

Summer 2014

# Structural Studies of Bile Salt Aggregation by Nuclear Magnetic Resonance Spectroscopy and Mass Spectrometry

Nicholas Doyle  
njd007@bucknell.edu

Follow this and additional works at: [https://digitalcommons.bucknell.edu/masters\\_theses](https://digitalcommons.bucknell.edu/masters_theses)



Part of the [Analytical Chemistry Commons](#)

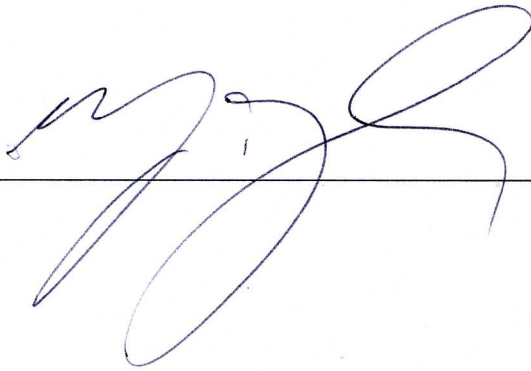
---

## Recommended Citation

Doyle, Nicholas, "Structural Studies of Bile Salt Aggregation by Nuclear Magnetic Resonance Spectroscopy and Mass Spectrometry" (2014). *Master's Theses*. 197.  
[https://digitalcommons.bucknell.edu/masters\\_theses/197](https://digitalcommons.bucknell.edu/masters_theses/197)

This Masters Thesis is brought to you for free and open access by the Student Theses at Bucknell Digital Commons. It has been accepted for inclusion in Master's Theses by an authorized administrator of Bucknell Digital Commons. For more information, please contact [dcadmin@bucknell.edu](mailto:dcadmin@bucknell.edu).

I, Nicholas J. Doyle, do grant permission for my thesis to be copied.



---

8/7/14



STRUCTURAL STUDIES OF BILE SALT AGGREGATION BY NUCLEAR  
MAGNETIC RESONANCE SPECTROSCOPY AND MASS SPECTROMETRY

by

Nicholas J. Doyle

A Thesis

Presented to the Faculty of  
Bucknell University  
In Partial Fulfillment of the Requirements for the Degree of  
Master of Science in Chemistry

Approved:



Timothy G. Strein  
Thesis Advisor  
Chair, Department of Chemistry



David Rovnyak  
Thesis Advisor

7/31/14

Date

## ACKNOWLEDGMENTS

As I look back at my time at Bucknell, I realize and am appreciative of how much I have grown here, as a person. When I first arrived in Lewisburg, I had just graduated from Geneseo, with only average grades, and had little idea of what I really wanted to do for a living. All I knew for certain was that I was decent at chemistry; I did not have any experience doing research or performing chemistry outside of class-mandated labs. The seminars, speakers, and greater exposure to conferences and higher academia provided to me at Bucknell, however, allowed me to pinpoint my professional strengths and determine a career path that best utilizes those strengths. While I enter the next phase of my education – law school at American University to pursue a career in patent law – with great excitement, I know I would not have gotten to this point without the help of several people. First and foremost, Drs. Strein and Rovnyak have been incredible mentors and have been instrumental (Strein-style pun) in showing me the world of academics. I would also like to thank Drs. Swan and Tillman for serving on my committee. Finally, I would be remiss if I did not thank my fellow students, particularly Mike, Broc, Dan, Matt, Scott, Adam, Will, Claire, Maria, Shauna, and Strein/Rovnyak group members past and present. You guys have been a fun group of both scientists with great futures and close companions with whom I have shared (and forgotten) tons of memories.

**TABLE OF CONTENTS**

LIST OF FIGURES .....	vi
LIST OF TABLES .....	x
ABSTRACT.....	xii
1. Introduction.....	1
1.1 Bile Salts and Probe Molecules .....	2
1.1.1 Cholate and Its Derivatives .....	3
1.1.2 Models of Bile Salt Aggregation.....	5
1.1.3 Probe Molecules .....	7
1.2 Nuclear Magnetic Resonance Spectroscopy .....	8
1.2.1 NMR History.....	8
1.2.2 NMR Theory.....	11
1.2.3 Structural Elucidation from NMR Spectra.....	17
1.2.4 Heteronuclear Single Quantum Coherence Spectroscopy...	20
1.2.5 Critical Micelle Concentration Determination .....	23
1.2.6 Bile Salts and NMR.....	26
1.3 Mass Spectrometry .....	28
1.3.1 MS History.....	28
1.3.2 MS Theory.....	29
1.3.3 The Mass Spectrometer.....	32
1.3.3.1 Electrospray Ionization .....	33

1.3.3.2 Orbitrap Mass Analysis and Detection .....	35
1.3.4 Bile Salts and MS.....	37
2. Experimental.....	39
2.1 Reagents.....	39
2.2 Instrumentation .....	39
2.2.1 MS Parameters .....	40
2.3 Standard Solutions for NMR .....	40
2.4 Standard Solutions for MS .....	41
3. Results and Discussion .....	42
3.1 Critical Micelle Concentration Determination Using Nuclear Magnetic Resonance Spectroscopy .....	42
3.1.1 The Phase-Transition Model.....	44
3.1.2 Principle Component Analysis for CMC Determination Using NMR Data.....	53
3.2 Micellar Structural Elucidation by Heteronuclear Single Quantum Coherence Spectroscopy.....	57
3.2.1 The Absolute Method for Considering Shifts in HSQC Data.....	63
3.2.2 The Conserved Method for Structural Elucidation from HSQC Data.....	72

3.3 Aggregation Number Determination of the Cholate Micelle System as Determined by Mass Spectrometry .....	81
4. Conclusion .....	94
References .....	95



## LIST OF FIGURES

Figure 1. Structures of Bile Salts .....	4
Figure 2. Small's Model .....	6
Figure 3. Kawamura's Model .....	6
Figure 4. Giglio's Model .....	6
Figure 5. The Structures of S- and R-BNDHP .....	7
Figure 6. The Precession of a Nuclear Magnetic Moment About an External Magnetic Field .....	12
Figure 7. Energy Level Diagram of a Nucleus with $m_s = \frac{1}{2}$ .....	13
Figure 8. Vector Diagram of an NMR Experiment .....	15
Figure 9. FID Converted to a Frequency-Dependent Spectrum by FT .....	16
Figure 10. Electrons Shielding a Nucleus from an External Magnetic Field .....	18
Figure 11. Ring Current .....	19
Figure 12. An Example HSQC Spectrum.....	21
Figure 13. An Example Mass Spectrum .....	32
Figure 14. A Schematic of an Electrospray Ionization Apparatus in Negative Ion Mode.....	34
Figure 15. A Schematic of an Orbitrap Mass Analyzer.....	36
Figure 16. A Stack Plot of BNDHP Proton NMR Spectra with Varying Cholate Concentration .....	43
Figure 17. Phase-Transition Modeling of BNDHP H3.....	46

Figure 18. Phase-Transition Modeling of BNDHP H4.....	47
Figure 19. Phase-Transition Modeling of BNDHP H5.....	48
Figure 20. Phase-Transition Modeling of BNDHP H6.....	49
Figure 21. Phase-Transition Modeling of BNDHP H7.....	50
Figure 22. Phase-Transition Modeling of BNDHP H8.....	51
Figure 23. Score Plot of Matrix in Table 3 .....	55
Figure 24. Structure of Cholate with Numbered Carbons.....	58
Figure 25. Overlay Plot of Several HSQC Spectra of Varying Concentrations of Cholate with S-BNDHP .....	59
Figure 26. Overlay Plot of Several HSQC Spectra of Varying Concentration of Cholate with R-BNDHP.....	60
Figure 27. Overlay Plot of Several HSQC Spectra of Varying Concentration of Cholate without Probe.....	61
Figure 28. Example of how the Absolute Method Measures Perturbation.....	64
Figure 29. Example of how the Absolute Method Measures Perturbation.....	65
Figure 30. Bar Graph Showing the Chemical Shift Perturbation of Cholate Carbons with R-BNDHP using the Absolute Method.....	66
Figure 31. Bar Graph Showing the Chemical Shift Perturbation of Cholate Carbons with S-BNDHP using the Absolute Method .....	67
Figure 32. Aggregation Interactions of Cholate with R-BNDHP Mapped onto the Structure of Cholate .....	68

Figure 33. Aggregation Interactions of Cholate with S-BNDHP Mapped onto the Structure of Cholate .....	68
Figure 34. Comparing Cholate Chemical Shift Perturbation Data from R- and S-BNDHP .....	70
Figure 35. Structure Showing Which Carbon-Proton Pairs Experience Stronger Perturbation as a Result of Aggregation with R- or S-BNDHP .....	71
Figure 36. Bar Graph Showing Conserved Data During Preliminary Aggregation .....	74
Figure 37. Bar Graph Showing Conserved Data During Primary Aggregation ...	75
Figure 38. Bar Graph Showing Conserved Data from 20 to 30 mM Cholate.....	76
Figure 39. Bar Graph Showing Conserved Data from 30 to 80 mM Cholate.....	77
Figure 40. Bar Graph Showing the Conserved Data Throughout the Aggregation Process.....	78
Figure 41. Full Mass Spectrum Collected from a 70 mM Sample of Sodium Cholate .....	83
Figure 42. Blown Up Area of Mass Spectrum: $m/z = 611$ .....	84
Figure 43. Blown Up Area of Mass Spectrum: $m/z = 815$ and $837$ .....	85
Figure 44. Blown Up Area of Mass Spectrum: $m/z = 1267$ .....	86
Figure 45. Blown Up Area of Mass Spectrum: $m/z = 1698$ .....	87
Figure 46. Blown Up Area of Mass Spectrum: $m/z = 2128$ .....	88
Figure 47. Blown Up Area of Mass Spectrum: $m/z = 2343$ .....	89

Figure 48. Blown Up Area of Mass Spectrum:  $m/z = 2558$ .....90

**LIST OF TABLES**

Table 1. Literature Proposed CMC Values for Cholate.....	25
Table 2. A Selection of Isotopes and Their Natural Abundances .....	31
Table 3. CMC of Cholate as Determined by Phase-Transition Modeling .....	52
Table 4. Matrix upon which PCA was Performed Treating the Chemical Shifts as Variables.....	54
Table 5. Cholate Aggregates Observed by Mass Spectrometry.....	91

## Abstract

Bile salts are biomolecules that are produced in the liver and are responsible for a range of functions in the process of digestion, primarily the emulsification of dietary fat and fat-soluble vitamins. Despite their importance in biological chemistry, the structure and dynamics of bile salt aggregation are not well understood. The efforts described herein attempt to enhance the understanding of cholate aggregation numbers (AN), critical micelle concentration (CMC), micellar structure(s), and interactions with a binaphthyl probe molecule. Cholate is the most common bile salt in mammals and is, therefore, a decent model for describing bile salt aggregation. CMC determination is achieved by observing the  $^1\text{H}$  NMR chemical shift perturbation of 1,1'-binaphthyl-2,2'-diyl hydrogen phosphate (R,S-BNDHP), a probe molecule for bile salt aggregation, when exposed to increased concentrations of sodium cholate. Using NMR and a phase-transition model to determine CMCs for pH 12.0 sodium cholate results in the observation of three unique CMC values at 6.1, 11.0, and  $\sim 25$  mM. Using  $^1\text{H}$ - $^{13}\text{C}$  heteronuclear single quantum coherence (HSQC) spectroscopy, a two-dimensional NMR experiment, it appears that anti-parallel cholate dimers are not strictly collinear, but rather a skew exists between the two-cholate monomers. The existence of a skew is surprising as it would be incongruent with a well-known model of bile salt aggregation proposed by Donald Small proposed in 1968. HSQC also showed evidence that R- and S-BNDHP attack different edges

of a cholate aggregate, possibly explaining the chiral selectivity exhibited by sodium cholate aggregates in earlier micellar electrokinetic chromatography experiments and confirming previous two-dimensional nuclear Overhauser effect (NOE) NMR data. HSQC data also suggest evidence for the interactions responsible for the aggregation of predicted aggregates by Small's model. High-resolution negative ion electrospray ionization mass spectrometry (ESI-MS) data suggest that cholate is capable of forming several aggregates of sufficient stability for mass analysis, the most massive of which is an aggregate with an aggregation number of 18. With these data it is clear that this system has several complexities that affect aggregation that may not be accounted for in previous bile salt aggregation models.

## 1. Introduction

Bile salts are biological detergents that play several important roles in the digestive systems of mammals. Bile salts are synthesized from cholesterol and are facial amphiphiles capable of forming complex micellar aggregates. Bile salts can also differentially bind chiral enantiomers of some pharmaceutically relevant molecules, making them analytically useful.<sup>1, 2</sup> Despite the biological and analytical importance of bile salts, the structure and dynamics of their aggregation is not well understood.

The goal of this work is to gain a greater understanding of bile salt aggregation, particularly in regard to the size, shape, and structure of the bile salt micelle, using nuclear magnetic resonance spectroscopy (NMR) and mass spectrometry (MS). One-dimensional (1D) proton (<sup>1</sup>H) NMR is a proven spectroscopic technique for determining molecular structure in small molecules by probing the chemical environment of individual protons within the molecule.<sup>3-7</sup> Using a probe molecule that is known to bind to bile salt micelles, aggregation and guest-host complexation can be studied.<sup>7-12</sup> Two-dimensional (2D) NMR can also be used to gain information on the guest-host complex and the shape of the micelle.<sup>3</sup> In particular, heteronuclear single quantum coherence spectroscopy (HSQC) is a two-dimensional NMR experiment that yields signals for a bonded carbon-proton pair.



Mass spectrometry (MS) is a well-characterized and highly predictable method of qualitative analysis, particularly for identifying biomolecules.<sup>13-16</sup> MS allows the determination of the mass and isotopic profile of molecules in a given sample. With these two pieces of information, it is possible to find the number of bile salt monomer units that compose a micelle in a particular solution, which is said to be the micelle aggregation number (AN). Therefore, modern MS has the resolution necessary to identify aggregates unambiguously.

### **1.1 Bile Salts and Probe Molecules**

Bile salts are naturally-occurring biomolecules that aid in the digestion of dietary fats and the uptake of fat-soluble species, such as vitamins A, D, E, and K in mammals.<sup>17-19</sup> Bile salts are produced via cholesterol 7  $\alpha$ -hydroxylase in the liver from cholesterol and are stored in the gallbladder. When food is digested, bile is released into the duodenum — the tissue that connects the stomach and small intestine — where it neutralizes remaining stomach acid and emulsifies fats. Bile salt micelles form in such a way that lets pancreatic lipase digest triglycerides allowing fats to be absorbed through the small intestine. Fat emulsification prevents lipids from aggregating and forming larger fat droplets, which would prevent fat absorption into the small intestine. While bile salts are a critical part of mammalian biology, questions still exist regarding the structure of

bile salt micelles, as well as the mechanism of micelle formation and aggregation in aqueous solutions.

### 1.1.1 Cholate and Its Derivatives

Bile is composed of several types of bile salts, approximately 80% of which are cholate and conjugates of cholate. Cholate (Fig. 1A) is composed of three six-membered rings, one five-membered ring, two methyl groups at carbons 18 and 19, as well as three hydroxyl groups. Conjugated forms of cholate also have a side chain that extends from the five-membered ring. Cholate typically forms a sodium salt under deprotonating conditions, but can form salts of calcium and potassium as well. The structures of cholate, chenodeoxycholate, deoxycholate, lithocholate, and taurodeoxycholate can be seen in Figure 1. Unlike traditional surfactants such as sodium dodecyl sulfate (SDS) that have hydrophilic head groups and hydrophobic tails, bile salts are facial amphiphiles, having a planar structure with faces of opposing polarity; the methyl groups are on the hydrophobic, slightly convex face and the hydroxyl groups are on the hydrophilic, concave face. In aqueous solvents, cholate monomers are thought to aggregate about the hydrophobic face, leaving the hydrophilic face exposed to solvent. As a result, bile salt aggregation is unique among surfactants, and a model that would characterize the aggregation of a traditional surfactant will not suffice for bile salt aggregates.

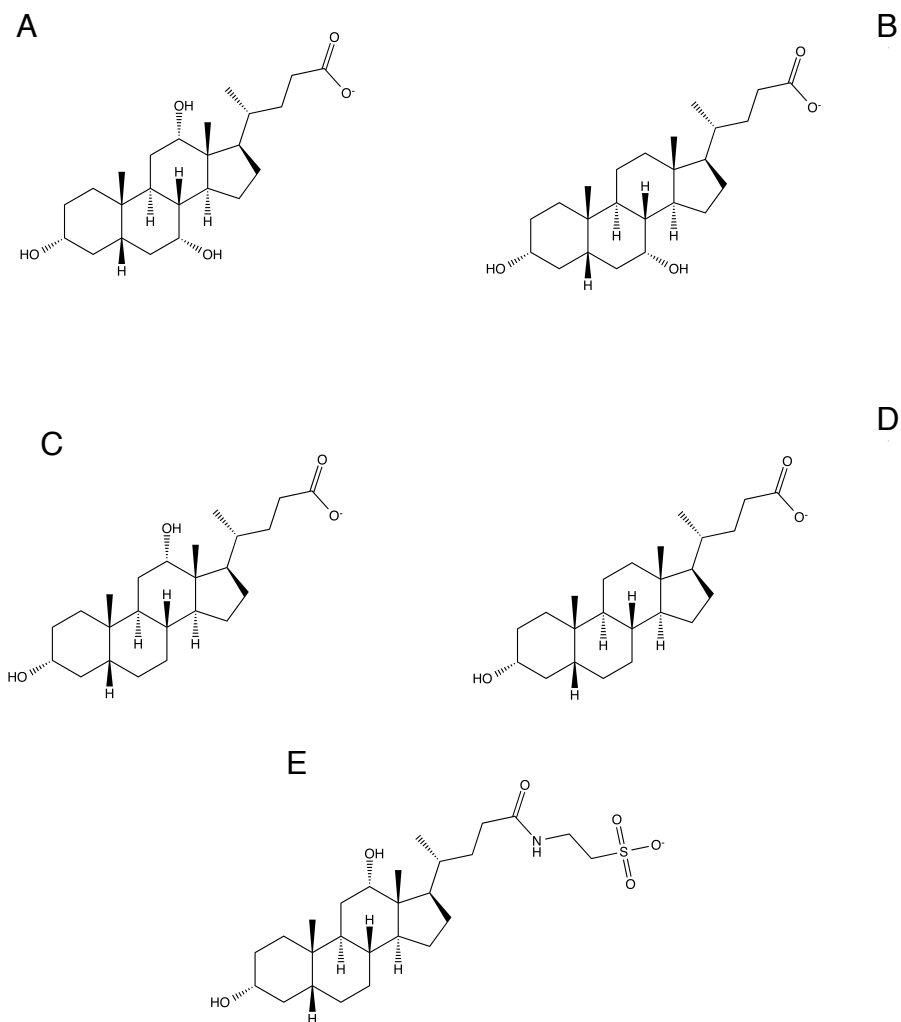
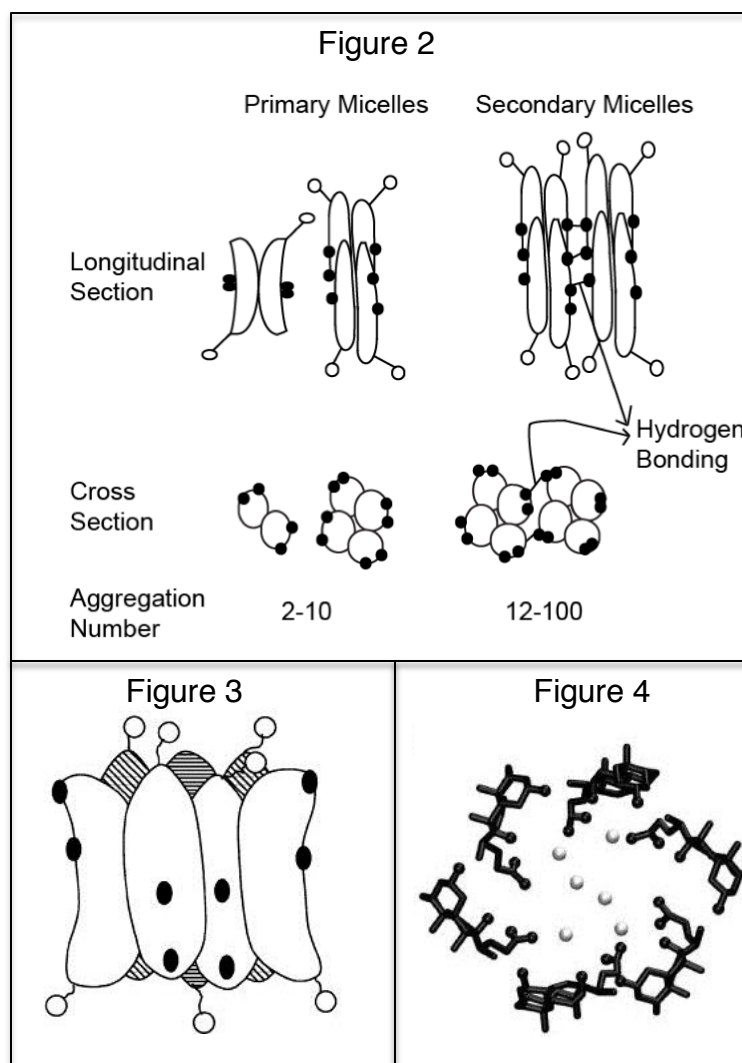


**Figure 1.** Structures of a selection of bile salts:

*A* Cholate, *B* Chenodeoxycholate, *C* Deoxycholate, *D* Lithocholate,  
*E* Taurodeoxycholate.

### 1.1.2 Models of Bile Salt Aggregation

Since the 1960s, bile salt micellar structure has been the subject of much debate, with three unique models having been proposed in the literature. In 1968, Donald Small proposed a model for bile salt aggregation, with a primary micelle consisting of two to ten bile salt monomers, and a secondary micelle comprised of two or more primary micelles (Figure 2).<sup>20</sup> The primary micelle forms through hydrophobic interactions, leaving the hydroxyl groups on the hydrophilic face exposed and able to form hydrogen bonds with water. Small's secondary micelle forms through hydrogen bonding of the hydroxyl groups on adjacent primary micelles. In 1989, Kawamura et al. proposed a monolayer disk-shaped micelle as a result of their spin-label studies (Figure 3).<sup>21</sup> Kawamura's model has a strong resemblance to Small's model, however instead of distinct secondary micelles, each additional bile salt monomer unit stacks together along one axis, forming a disk shape. Another published model, proposed by Giglio et al., predicts a helical structure with counter ions and water on the axis of the helix surrounded by bile salt monomers based on their x-ray spectroscopy studies (Figure 4).<sup>22</sup> No clear consensus of the true structure of aqueous bile salt micelles has emerged.



**Figures 2-4.** *Figure 2:* Small's Model suggesting a unique primary and secondary micellar structure.<sup>20</sup> (Artwork reproduced from Ouimet.<sup>23</sup>) *Figure 3:* Kawamura's model suggesting that additional bile salt monomers stack together, forming a disk-like shape.<sup>21</sup> *Figure 4:* Giglio's model depicting helical shaped micelles with water and counter ions arranged along the axis of the helix.<sup>22</sup> Artwork in figures 3 and 4 was reproduced, with permission, from Warren.<sup>24</sup>

### 1.1.3 Probe Molecules

The 1,1'-binaphthyl compounds used herein are model substrates for chiral recognition.<sup>1, 25</sup> In particular, 1,1'-binaphthyl-2,2'-diyl hydrogen phosphate (BNDHP) is used in these experiments (Figure 5). Instead of having one or several chiral centers, BNDHP has a chiral axis caused by restricted bond rotation about the 1,1' bond, making R- and S-BNDHP atropisomers.

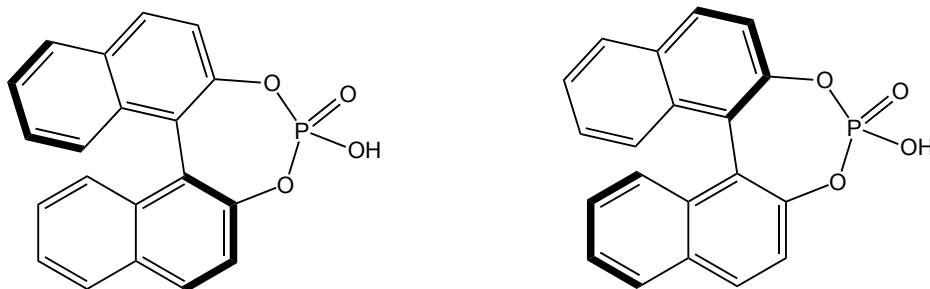


**Figure 5.** The structures of S-BNDHP (left) and R-BNDHP (right).

Due to its aromaticity, BNDHP is a convenient probe for NMR studies of bile salt aggregation, as bile salts are composed almost entirely of aliphatic carbons; therefore the signals from BNDHP protons and bile salt protons do not overlap. Previous work by Hebling et al.<sup>1</sup> and Eckenroad et al.<sup>12</sup> has shown the use of BNDHP in NMR studies of bile salts to be an effective way to determine the critical micelle concentration (CMC) of bile salt surfactant systems, which is the lowest concentration that aggregation can occur, as well as a method to infer the

structure of the bile salt aggregates. Evidence of the onset of cholate aggregation is when the chemical shifts of the BNDHP protons become perturbed.

## **1.2 Nuclear Magnetic Resonance Spectroscopy**

One powerful technique for structure elucidation is nuclear magnetic resonance spectroscopy (NMR). NMR provides information on local chemical environments that is not accessible with other methods,<sup>26, 27</sup> making it an oft-utilized technique by biochemists wishing to explore the structure of and interactions between biomolecules.<sup>11, 28-37</sup> Performing NMR on the protons and carbons of bile salts and their probe molecules can yield unique information about the structure of the bile salt aggregates and the mechanism by which they interact with a targeted molecule.

### **1.2.1 NMR History**

NMR is a technique that probes the chemical environments of spin-active nuclei. Though not all elemental isotopes are spin-active, it is estimated that about 80% of known elements possess at least one spin-active isotope.<sup>37</sup> A spin-active nucleus has an odd number of protons or an odd mass number and in the presence of an external magnetic field, the nucleus takes on a nuclear magnetic moment, a concept first proposed by Pauli in 1924 to explain hyperfine structure observed in atomic spectral lines.<sup>38</sup> The idea that a nucleus had a magnetic

moment was a surprising proposition in 1924, as it was a naturally occurring anomaly that was unaccounted for by classical mechanics. Later in the 1920s, Stern and Gerlach performed experiments with an inhomogeneous magnetic field that provided evidence for the quantization of two unique spin states for an electron.<sup>39-41</sup> The discovery by Stern and Gerlach of electron magnetic moments, coupled with Pauli's findings, gave rise to a focus on the investigation of nuclear magnetic moments in the 1930s. The final theoretical experiment before the practicality of NMR could be realized came in 1937, when Lazarev and Shubnikov published evidence of an equilibrium existing between nuclear spin states, giving credence to the theory of nuclear paramagnetism, or that a nucleus has a static magnetic moment.<sup>42</sup> By 1939, the first demonstration of nuclear magnetic resonance was carried out when Rabi et al. passed a beam of hydrogen molecules through a magnetic field induced by an electromagnet.<sup>43</sup> The frequency of the electromagnet was varied until the magnetism caused a deflection of the beam of hydrogen. It was not until 1945, however, that NMR as it is known today was developed. The final important development was undertaken by two groups working independently to make the spectroscopy of bulk samples possible; Purcell, Torrey, and Pound at Harvard started the field of solid-state NMR with their work on paraffin,<sup>44</sup> and Bloch, Hansen, and Packard at Stanford started the field of aqueous NMR with their work.<sup>45</sup> For developing the ability for NMR to be performed on bulk samples, furthering the burgeoning field



of NMR, Purcell and Bloch were awarded the Nobel Prize in physics, jointly, in 1952. Since the first NMR spectrometer, there have been hardware and software advances alike to bring NMR to the level that is currently enjoyed today; such advancements include the development of the superconducting magnet, to more efficiently create a magnetic field of high homogeneity.<sup>46</sup> It could be argued, however, that no single advancement has more shaped modern NMR than the development of pulsed Fourier transform (FT). FT is a technique that makes possible the simultaneous analysis of all frequencies. FT-NMR was first applied by Ernst in 1966 and led to the shortening of experiment times and improved signal-to-noise, allowing spectrometers to perform a greater variety of experiments than previously possible, a feat which won him the 1991 Nobel Prize.<sup>47</sup> In fact, the discovery and application of nuclear magnetism and its resonance have, thus far, earned five separate Nobel Prizes. Though most primitive NMR exploited the plentiful amount of spin-active protons available in a majority of samples, modern NMR can probe other biologically relevant nuclei such as  $^{13}\text{C}$ ,  $^{17}\text{O}$ ,  $^{19}\text{F}$ , and  $^{31}\text{P}$ .

### 1.2.2 NMR Theory

Nuclear magnetic resonance is a spectroscopic technique that exploits discrete differences in energy between nuclear spin or quantum states. In the case of NMR, there must exist a difference between the populations of nuclei in a magnetically polarized state and populations of nuclei in an unpolarized, or ground, state. Spin-active nuclei are polarized when they are placed in an external magnetic field. Nuclear polarization during the presence of the external magnetic field is dependent upon the quantized spin angular momentum ( $s$ ) of the spin-active nuclei. The number of protons and neutrons in the nucleus determines the existence of spin angular momentum; an even mass number yields a spin of zero, however odd mass numbers will yield quantifiable spins. For example,  $^{12}\text{C}$  has a spin of zero, while  $^{13}\text{C}$  has a spin of  $1/2$ . The spin states ( $m_s$ ) for  $^{13}\text{C}$  can, therefore, either be  $1/2$  or  $-1/2$ , where  $m_s = -1/2$  is the excited spin state. The nuclear spin angular momentum is critical in that it is necessary for the determination of a nuclear magnetic moment ( $\mu$ , N m/T). The magnetic moment a nucleus will have is determined by

$$\mu = \gamma s = \frac{\gamma m_s h}{2\pi}, \quad (1)$$

where  $\gamma$  is the magnetogyric ratio of the studied nucleus ( $\text{rad sec}^{-1} \text{ T}^{-1}$ ),  $s$  is the quantized spin angular momentum (J s),  $m_s$  is a spin state of the nucleus, and  $h$  is Planck's constant,  $6.626 \times 10^{-34} \text{ m}^2 \text{ kg/s}$ .<sup>36</sup> When a static magnetic field,  $B_0$ , is applied to a spin-active nucleus, the nuclear magnetic moment,  $\mu$ , of that nucleus

will undergo Larmor precession about the axis of  $B_0$  with a frequency called the Larmor frequency ( $\nu_0$ , rad/s or  $\omega_0$ , Hz), as seen in Figure 6.

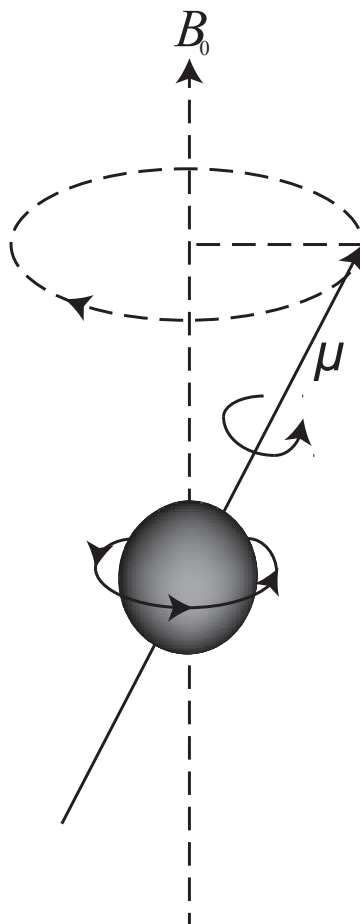


**Figure 6.** A nuclear magnetic moment caused to precess about an external magnetic field, reproduced from Ouimet.<sup>23</sup>

The Larmor frequency is meaningful, as it gives the energy difference between the ground state and the excited state and is given by

$$\omega_0 = \gamma B_0 = \frac{\Delta E}{\frac{h}{2\pi}}, \quad (2)$$

$$\nu_0 = \frac{\omega_0}{2\pi} = \frac{\Delta E}{h} = \frac{\gamma B_0}{2\pi}, \quad (3)$$

$$\Delta E = \gamma B_0 \left( \frac{h}{2\pi} \right), \quad (4)$$

where  $\omega_0$  is the Larmor frequency in Hz,  $\gamma$  is the magnetogyric ratio of the observed nucleus,  $B_0$  is the strength of the applied magnetic field (T),  $\Delta E$  is an energy difference (J),  $h$  is Planck's constant, and  $\nu_0$  is the Larmor frequency in rad/s. From equations 2-4, it can be seen that the energy difference between the excited and ground states ( $\Delta E$ ) increases linearly with the strength of the static magnetic field.<sup>37, 48</sup> This energy difference is equivalent to the amount of energy required to cause the magnetic moment of spin-active nuclei to flip from being parallel to the static magnetic field, a favorable position, to antiparallel to the field, which is energetically unfavorable, as seen in Figure 7.

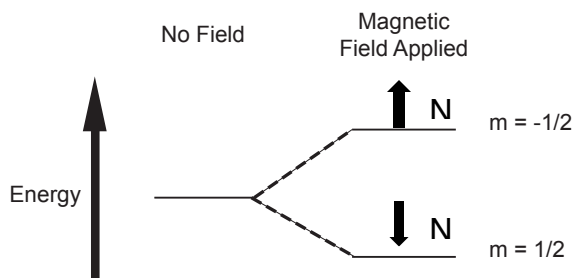


**Figure 7.** Energy level diagram of a nucleus with  $m_s = \frac{1}{2}$

The distribution of nuclei between these two states is described by the Boltzmann distribution, which relates the ratio of the population of nuclei in the excited state ( $P_{ex, m=-1/2}$ ) to the population of nuclei in the ground state ( $P_{gr, m=1/2}$ ) to the energy difference of the two states ( $\Delta E$ , J), temperature ( $T$ , K), and the Boltzmann constant ( $k_B$ ,  $1.381 \times 10^{-23} \text{ JK}^{-1}$ ) such that

$$\frac{P_{ex, m=-1/2}}{P_{gr, m=1/2}} = e^{(-\Delta E/k_B)}. \quad (5)$$

Since, as equation 4 shows, the magnitude of  $\Delta E$  is dependent on the strength of the magnetic field, applying the Boltzmann distribution yields that increasing the strength of the magnetic field increases the population difference and enhances signal-to-noise.<sup>48</sup>

A classical treatment of a sample of spinning nuclei leads to the concept of bulk magnetization. While individual nuclei can orient their magnetic moments in random directions in the absence of a static magnetic field, when a magnetic field is applied, the magnetic moments are weakly polarized along  $B_0$ . The bulk magnetization,  $M$ , is a vector that has the magnitude and direction equivalent to the sum of the individual magnetic moments, which precess about the applied magnetic field  $B_0$ . When an electromagnetically induced pulse is applied ( $B_1$ ), the bulk magnetization is rotated into the plane of the pulse, at which point the nuclei are said to be excited, and, after the pulse, precess at their characteristic Larmor frequency relaxing back to the pre-pulse equilibrium position in time ( $T_2$ ). This process is illustrated in Figure 8 that shows an external magnetic field ( $B_0$ ) with

which individual nuclear magnetic moments are aligning, forming the bulk magnetization vector ( $M$ ). Once a pulse is applied ( $B_1$ ),  $M$  is pushed into the same plane. After the pulse,  $M$  precesses about  $B_0$  back to the relaxed, equilibrium position.

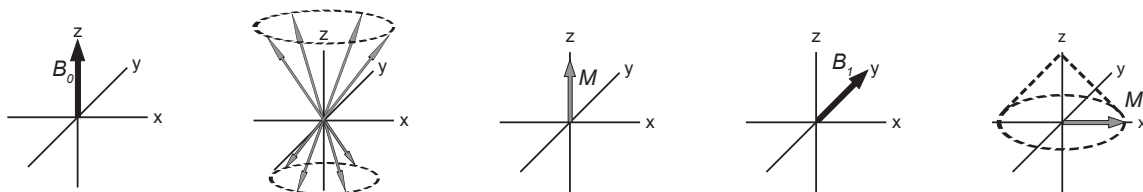


**Figure 8.** Vector diagram depicting a magnetic pulses affect on bulk magnetization.

If there is a suitably tuned receiver coil in the transverse plane, a current will be induced in the coil as  $M$  precesses. If, however, a pulse causes the bulk magnetization to have a direction that is perpendicular to the coil, no current will be induced. The time length of the pulse controls the degree of rotation of the bulk magnetization. Between pulses, it is necessary to allow the bulk magnetization to relax back to equilibrium population, and realign with  $B_0$ . It is from a single  $B_1$  pulse that a free induction decay (FID) is recorded with respect to time, where the maximum and minimum signal are recorded when the bulk magnetization are directed with the coil, zero signal is seen when  $M$  is

perpendicular to the coil, and an oscillating signal magnitude is observed between. If the FID is subject to a Fourier transform, to convert the signal from the time domain to the frequency domain, the familiar looking NMR spectrum appears. An FID and its resulting frequency-dependent spectrum can be seen in Figure 9. Because frequency units, Hz, are field dependent, standards such as tetramethylsilane (TMS) are used to ensure uniformity from spectrometer to spectrometer. The location of a signal relative to the location of the standard peak is referred to as a peak's chemical shift. Chemical shifts ( $\delta$ ) are strictly unitless, but are expressed as part per million (ppm) by

$$\delta = \frac{\nu_i - \nu_{ref}}{\nu_0} \cdot 10^6, \quad (6)$$

where  $\nu_i$  is the resonant frequency of the nucleus (Hz),  $\nu_{ref}$  is the frequency of the reference (Hz), and  $\nu_0$  is the operation frequency of the spectrometer (Hz), which is nuclei and magnet strength specific. The proton operating frequency on a 14.1 T magnet, for example, is 600 MHz based on the resonance of TMS.

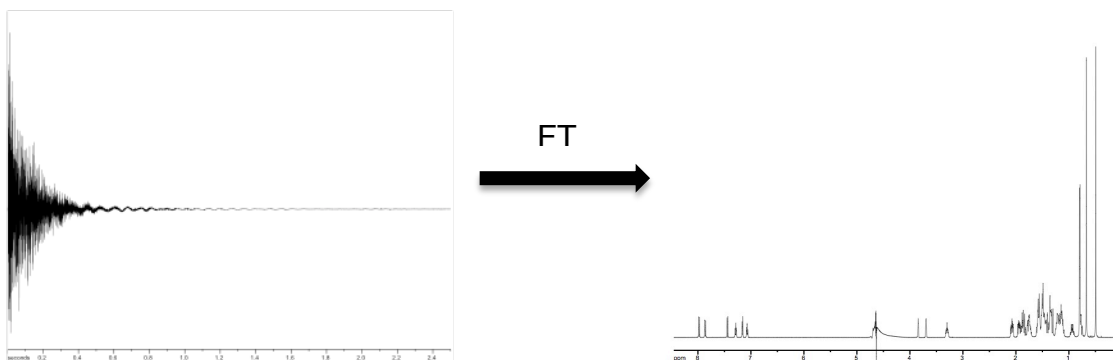


**Figure 9.** An FID is converted into a frequency domain spectrum by FT.

### 1.2.3 Structural Elucidation from NMR Spectra

As NMR is a probative technique for local chemical environment, both structural and environmental information can be gained with NMR. The information manifests itself as spectral data: certain chemical environments cause signals to appear at predictable frequencies. These predictable shifts are caused by the presence of electrons, called electronic shielding, that exert a small local magnetic field ( $B_{loc}$ ) that opposes the applied static magnetic field,  $B_0$ , an effect that is illustrated in Figure 10. The opposing local magnetic field, which is a physically necessary phenomenon that ensures that electromagnets abide by Newton's third law – which states that for every action there is an equal and opposing reaction – and the conservation of energy, is known as Lenz's Law. For example, a proton on a primary alkyl group will experience shielding and will have a resonance that is only minimally perturbed. On the other side of the spectrum, the acidic proton of a carboxylic acid will resonate at a higher frequency due to the deshielded environment caused by the electron withdrawing nature of the carbonyl and alcohol oxygen.



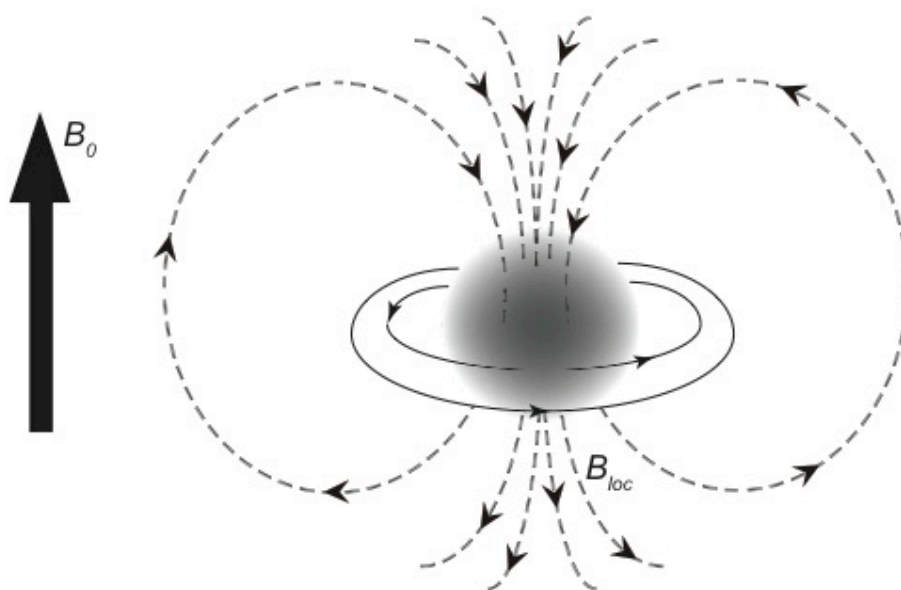


**Figure 10.** Opposing local magnetic field experienced by a nucleus as a result of circulating electrons, reproduced from Ouimet.<sup>23</sup>

Due to  $\pi$ -bonding structures, aromatic protons resonate at higher frequencies. In an effect that follows Lenz's law, ring current occurs when the plane of an aromatic ring system is held perpendicular to a magnetic field. Because these electrons are part of a delocalized  $\pi$ -system, the atoms of an aromatic molecule are more susceptible to develop induced currents in the molecular framework than localized electrons in a  $\sigma$ -system. The delocalized electrons cause the ring system to experience a magnetic field,  $B_{loc}$ , that slightly opposes  $B_0$ . The further from the ring system, though, the more  $B_{loc}$  gets forced back into alignment with  $B_0$ . By a carbon-proton bond length away from the ring system,  $B_{loc}$  has totally

reoriented with  $B_0$ . The magnetization experienced by the proton,  $B_H$ , is, therefore, a sum of  $B_0$  and  $B_{loc}$ . Ring current results in aromatic protons appearing in a narrow location on NMR spectra (7-9 ppm), making aromatic molecules valuable analytes for NMR experimentation.

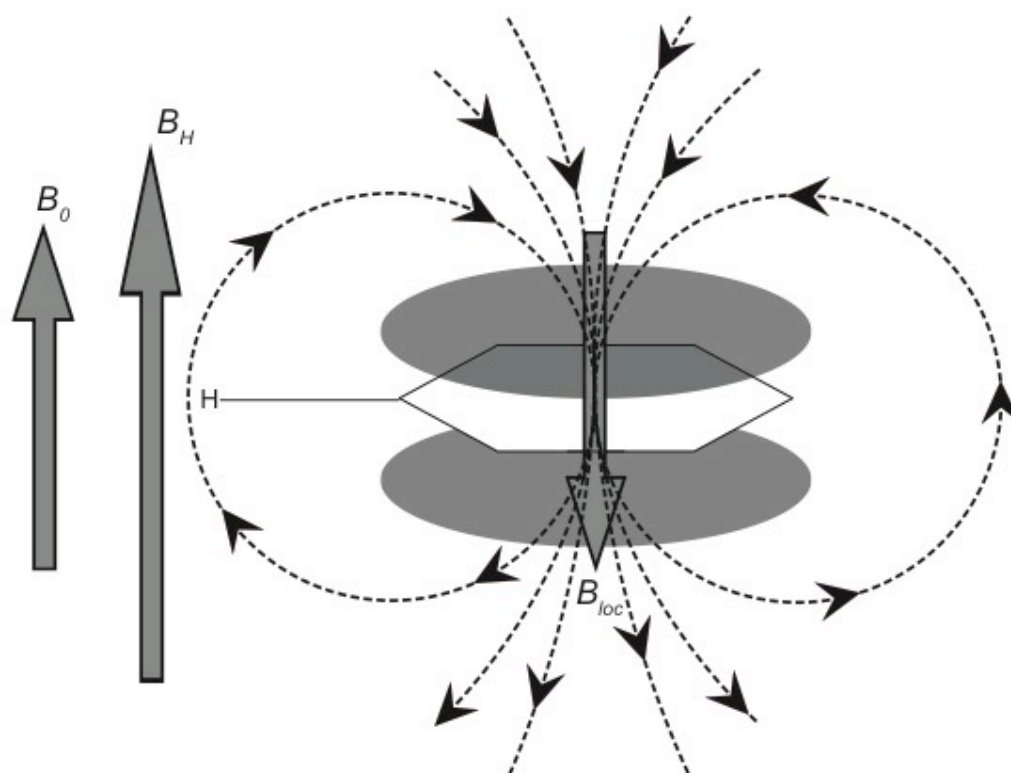


**Figure 11.** Increased magnetism experienced by an aromatic hydrogen as a result of ring current.

Two final pieces of 1D NMR spectral data from which structural information can be inferred involve the intensity, or height, of the peaks and the splitting, or number of peaks per signal. Peak splitting is determined by J-coupling, which is an electron-mediated coupling between two nuclei that are close in the bonded network of a molecule. In proton NMR, each signal has intensity that is proportional to the concentration of the proton (or set of equivalent protons) that gave rise to that signal. The signal is also split into a number of peaks, referred to as a multiplet, equivalent to  $n+1$ , where  $n$  is the number of magnetically equivalent hydrogens on neighboring carbons. The intensity of each peak corresponds to Pascal's triangle such that, for example, a triplet will split into peaks with intensities of 1:2:1. From typical 1D and 2D NMR, the connectivity of all atoms in a molecule can often be solved.

#### **1.2.4 Heteronuclear Single Quantum Coherence Spectroscopy**

Heteronuclear Single Quantum Coherence Spectroscopy (HSQC) is a two-dimensional NMR technique, meaning that two axes in the spectrum contain complementary chemical shift information. The HSQC reports the chemical environment of a bonded atomic pair, such as  $^1\text{H}$ - $^{13}\text{C}$  as utilized herein. The pulse sequence can be manipulated, however, so that other pairs, such as  $^1\text{H}$ - $^{15}\text{N}$ , can be probed by HSQC. The sensitivity to  $^1\text{H}$ - $^{13}\text{C}$  pairs manifests as a signal appearing only where there is a peak on the  $^{13}\text{C}$  spectrum, the "y-axis" or

indirect dimension of the HSQC spectrum, and a corresponding peak on the proton spectrum (“x-axis”) that is bonded to that carbon. As shown in Figure 12, a “dot” on the spectrum shows both the proton chemical shift (“x-axis”) and the carbon chemical shift (“y-axis”) of the carbon to which the proton is bonded.

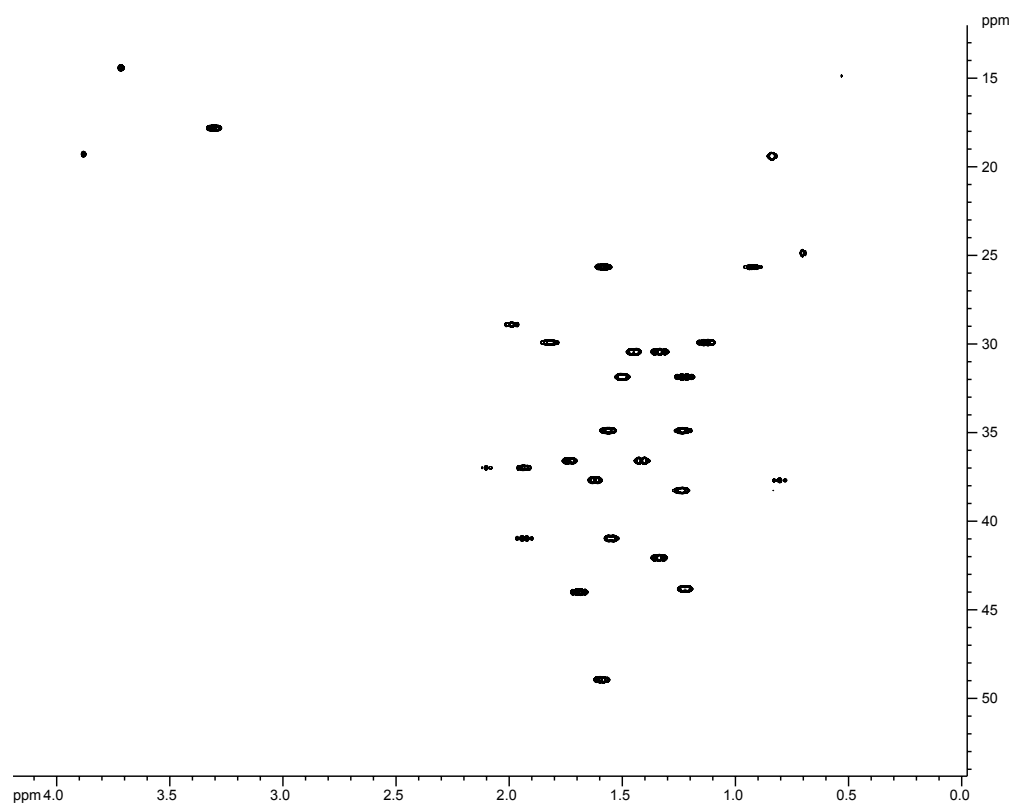


**Figure 12.** An HSQC spectrum of 80 mM sodium cholate at pH 12 with a 10% v/v D<sub>2</sub>O lock.

Bodenhausen and Ruben reported the first HSQC experiment in 1980, using an experiment that described a method to enhance the signal of less sensitive nuclei using a “double transfer of polarization.”<sup>49</sup> While the HSQC was initially performed with a  $^1\text{H}$ - $^{15}\text{N}$  pair, similar results were later recorded for a  $^1\text{H}$ - $^{13}\text{C}$  pair.<sup>50</sup> The key to HSQC experiments, the aforementioned transfer of polarization, is a phenomenon called insensitive nuclei enhanced by polarization transfer, or INEPT, and was first reported by Morris and Freeman in 1979.<sup>51</sup> A working way to think about an INEPT step is to consider that the proton has a larger Boltzmann population difference than that of carbon-13. The energy from this difference is transferred, via J-coupling, from the proton to the heteroatom it is bonded to, exciting the heteroatom’s nuclear spin. The moniker of double INEPT is earned when the energy of excitation is transferred back to the original proton, whose magnetic moment now has a precession that accounts for both the proton and carbon chemical environments; the proton is considered “labeled” by the Larmor frequency of its attached carbon. Because the proton relaxes more quickly than the carbon, each experiment can be repeated on the timescale of the proton relaxation, which is generally much shorter than the  $^{13}\text{C}$  relaxation time.

HSQC experiments do, however, take 6-18 hours longer to complete on a 14.1 T magnet than the typical 1D proton NMR experiments. Due to these time constraints, it is necessary to limit the number of samples analyzed.

### 1.2.5 Critical Micelle Concentration Determination

The critical micelle concentration (CMC) is an important description of surfactant chemical systems and describes the lowest concentration at which aggregation will occur. The CMC is influenced by thermodynamic as well as electrostatic and other attractive forces. A surfactant system can have several CMCs that describe sequential aggregation steps (monomer to dimer to tetramer, etc.).

NMR is a powerful tool for CMC determination, as it provides information on intermolecular interactions with atomic resolution. In studies of surfactant systems, a probe molecule that is known to form guest-host complexes with the surfactant can be used to determine the surfactant's CMC because any perturbation of chemical shift serves as evidence of both complexation and the onset of a CMC.<sup>4, 7, 31</sup> To mathematically model the chemical shift perturbations seen in <sup>1</sup>H NMR, a phase-transition model can be employed. The model treats the observed chemical shift ( $\delta_{obs}$ ) as a weighted average of the free ( $\delta_{free}$ ) and bound ( $\delta_{bound}$ ) chemical shifts such that

$$\delta_{obs} = f_{free} \delta_{free} + f_{bound} \delta_{bound} , \quad (7)$$

where  $f_{free}$  is the fraction of probe that is free in solution and  $f_{bound}$  is the fraction of probe that is bound in solution.<sup>52</sup> Since, experimentally, it is often difficult to determine what fraction of the probe is bound or not, another way to express equation 7, which incorporates the CMC of the system, is

$$\delta_{obs} = \frac{CMC}{[CA]_{total}} (\delta_{free} - \delta_{bound}) + \delta_{bound} , \quad (8)$$

where  $[CA]_{total}$  is the total concentration of the bile salt. Equation 8 is what is ultimately used to model data to determine the CMC. Equation 8 is obtained from equation 7 by the assumption that the CMC is equivalent to the concentration of free monomer. If untrue, this assumption could add bias and inaccuracy to the resulting CMC.

Another method that may have the potential to rigorously determine the CMC is principal component analysis (PCA). PCA is a treatment of data that employs matrix math to cluster variables based on how the variables cause variance in the data set in relation to the variance caused by other variables. Ultimately, the goal is to reduce many correlated variables to a much smaller number of uncorrelated variables, termed principal components. It is not immediately obvious, however, what the meaning of a principal component is, as a principal component is often several variables or physical phenomena experienced by the system under investigation. The definition of a principle component is not explicit, but rather guided by the user's understanding of the data set. PCA could, theoretically, yield more accurate CMC determinations than the phase-transition model because, while the phase-transition model attempts to fit physical observations to a model bound by ideal parameters and possibly biased by assumption, PCA is not model-dependent and can be sensitive to correlations between anything that may

cause variance in the data. Therefore, determinations made based on PCA avoid the possible pitfalls of bias introduced by expectation in a model.

Table 1 shows a list of previously reported CMC values for the bile salt sodium cholate found in literature.

**Table 1 Literature Proposed CMC Values for Cholate**

Method	Conditions	CMC (mM)
Electron Spin Resonance	pH 7.8, 30°C, borate, stearic acid, and methyl ester nitroxide <sup>53</sup>	5, 8
Potentiometry	25°C <sup>54</sup>	11
Dye Titration	25°C, pH 10.0, 0.15 M NaCl <sup>55</sup>	2.3
Fluorescence Probe	pH 8.0-8.4 <sup>36</sup>	13.5
	1,6-diphenylhexatriene probe <sup>56</sup>	16
Surface Tension	25°C, pH 8 <sup>57</sup>	13
Capillary Electrophoresis	20 mM sodium phosphate buffer pH 7 <sup>58</sup>	12.8
	25°C, pH 8.5, in Sudan III <sup>59</sup>	9
NMR	pH 8-8.4 <sup>26</sup>	16
	pH 12, 2.5 mM BNDHP probe, sodium cholate x-hydrate <sup>1</sup>	7±1, 14±1
Solubilization Assay	30°C, pH 7.8 (borate), assay with cholesterol <sup>60</sup>	19
Theoretical Model <sup>61</sup>		27.4
Calorimetry	30°C, pH 7.9 (K <sub>3</sub> PO <sub>4</sub> ) <sup>26</sup>	18.4



As made clear in table 1, the CMC of cholate can be affected by several factors such as the method used to probe the aggregation, the pH and ionic strength of the solvent, and the concentration of any probe used.

### 1.2.6 Bile Salts and NMR

NMR has been considered a useful tool for the study of guest-host interactions, such as the interactions between bile salts and probe molecules.<sup>1,7,26,62-64</sup> Systems of glycine- and taurine-conjugated bile salts have been studied using several different probes by rotating frame nuclear Overhauser effect spectroscopy (ROESY), a 2D-NMR technique that can give the user an idea of atoms or parts of a molecule that are near each other through space.<sup>62-64</sup> Because ROESY measures proton-proton “through-space” connectivity, as opposed to “through-bond”, ROESY can provide insight on noncovalent interactions, such as the interactions a surfactant would experience during guest-host docking. Using  $\beta$ -cyclodextrin, Schönbeck et al. and Holm et al. found that the side chain, or tail, of the bile salts, as well as the five-membered ring of the bile salts have strong interactions with protons on  $\beta$ -cyclodextrin.<sup>62, 63</sup> The results of the ROESY experiment led Schönbeck and Holm to conclude that bile salts attack molecules in a tail-first manner, allowing the tail to wrap around the molecule. Dominguez et al. also found that bile salts attacked pig and horse colipase in the same tail first manner inferred by Schönbeck and Holm.<sup>64</sup>

Another area of interest is the origin of bile salt chiral recognition. Hebling et al. found that bile salts could resolve racemic mixtures of binaphthyl-based compounds with chiral specificity.<sup>1</sup> While the chiral recognition of bile salts was observed by micellar electrokinetic chromatography (MEKC),<sup>1</sup> 1D <sup>1</sup>H NMR also show that proton signals of one atropisomer of BNHDP are more perturbed by increased bile salt concentration than proton signals of the other atropisomer of BNDHP. The increased perturbations of S-BNDHP over R-BNDHP suggest that bile salts S-BNDHP more strongly than R-BNDHP. Evidence for the origin of the chiral selectivity of deoxycholate was found after nuclear Overhauser effect spectroscopy (NOESY) NMR studies by Eckenroad showed that S-BNDHP and R-BNDHP attacked different edges of the cholate micelle.<sup>12</sup> Despite the findings from the aforementioned NMR experiments of bile salts, a consensus regarding the structural model of bile salts and the origin of chiral selectivity by bile salts remains to be found.

### 1.3 Mass Spectrometry

Mass spectrometry (MS) is used to obtain the mass and isotopic profile of analyte ions or fragments. The ability for MS to distinguish between components of a sample by mass makes it an attractive tool to analyze bile salt micelle solutions, as well as perhaps gain a greater thermodynamic understanding of how bile salt micelles are formed.

#### 1.3.1 MS History

Mass spectrometry is a powerful technique for determining the masses of molecules or fragments of molecules and the isotopic profiles of the atoms that make up those molecules. The development of MS began in 1898 when Wien demonstrated that streams of positively charged particles could be bent by a strong magnetic field suggesting that the particles were different masses.<sup>65</sup> In 1913, Thomson published data showing that, using a similar technique, the resolution of  $^{20}\text{Ne}$  from  $^{22}\text{Ne}$  was possible.<sup>66</sup> Thomson accomplished this by flowing atomic neon through a permeated cathode to ionize the gas. The gas was exposed to a strong magnetic field, which caused the streams of neon isotopes to bend at differing degrees. A piece of photographic paper was then exposed to the stream, which showed that the stream of neon had a much wider band than usual, leading Thomson to believe that there were multiple isotopes of neon.<sup>66</sup> In 1919, Francis Aston, Thomson's student, improved the experiment by developing

the first modern mass spectrometer, the magnetic sector.<sup>67</sup> Aston used this instrument to discover 212 of the 281 naturally occurring isotopes, an achievement that was recognized with his receiving of the 1922 Nobel Prize for chemistry.

### 1.3.2 MS Theory

While the principles that govern mass spectrometry have remained, improvements have been made in an attempt to optimize a spectrometer's resolving power. The resolving power is a measure of how well a spectrometer separates two peaks of similar mass. This is an important parameter as the ability to distinguish peaks is required for acquiring the full isotopic profile, needed to identify the analyte. The resolving power is defined as

$$\text{Resolving power} = \frac{m}{\Delta m}, \quad (9)$$

where  $m$  is the smaller value of  $m/z$  and  $\Delta m$  is the difference in  $m/z$  between two peaks. While the mass spectrometers of old had resolving powers that were as low as 130, today's spectrometers are capable of resolving powers approaching or even surpassing  $1 \times 10^6$ .

Mass spectrometry can be performed on both bulk samples and samples purified by chromatography. The chromatographic step, if there is one, is typically performed with gas chromatography (GC), however high-performance liquid chromatography (HPLC) and capillary electrophoresis (CE) have also been

interfaced with MS.<sup>68</sup> Chromatography can be beneficial in that separating solutions into its components can produce a cleaner mass spectrum.

To perform MS, a sample must first be volatilized and ionized. Analytes are required to be gas phase ions because MS is performed under a vacuum and uses electric potentials and/or magnetic fields to move ions through the instrument. Once the sample is isolated, vaporized, ionized, and accelerated into the mass spectrometer, it encounters the mass analyzer. The mass analyzer has been the most improved aspect of the mass spectrometer since its inception, having progressed from the magnetic sector of the early 1900s to analyzers that have resolving power that is thousands of times more powerful today. Mass analyzers relate ion motion to their mass-to-charge ratio; the magnetic sector, for example, analyzes masses by exploiting a relationship between the mass-to-charge ratio and adjustable magnetic field strength. Typically, mass analyzers relate an ion's momentum or velocity to their mass-to-charge ratio. Because of this, high-resolution mass analyzers have the ability to detect the mass of analyte ions to within a few ppm of the exact, monoisotopic mass of ions, accounting even for different isotopes of atoms in the ion. The intensity of any peak that is a result of an isotope should be proportional to that isotope's natural abundance, meaning the most abundant isotopes will be the largest contributor to the total mass of the ion. A selection of isotopic natural abundances of some common elements is shown in Table 2. After the ion is analyzed, it is then detected; a

mass spectrometer detector is typically an electron multiplier, which amplifies the current produced when the ion hits a charged surface. Detectors can also be used in concert with the mass analyzers to produce a time-dependent spectrum, much like that of an NMR. The signal from the mass analyzer is related to the intensity of the signal produced by the molecule at the detector by a transducer, yielding a spectrum with intensity (or relative intensity to the “base peak,” the largest peak) along the y-axis and the mass-to-charge ratio along the x-axis, as seen in Figure 13.

**Table 2 Selection of Isotopes and Their Natural Abundances**

Element	Mass Number	Mass (Da)	Abundance (%)
H	1	1.007825	99.988
	2	2.01410	0.012
C	12	12. (exact)	98.93
	13	13.00335	1.07
O	16	15.99491	99.757
	17	16.99913	0.205
	18	17.99916	0.038

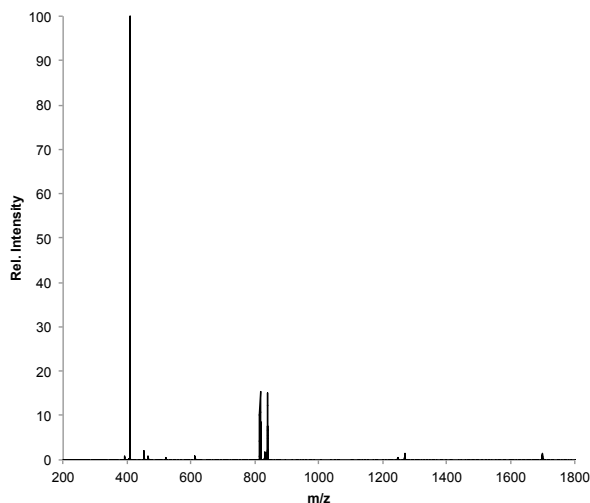


**Figure 13.** A mass spectrum of 70 mM sodium cholate collected by ESI-MS with orbitrap mass analyzer.

### 1.3.3 The Mass Spectrometer

The mass spectrometer has three main modules – ionization, mass analysis, and ion detection. Some mass analyzers can do both analysis and detection of the ion. Different kinds of samples require different methods of ionization depending upon the medium the sample is in. For an aqueous solution composed of ionic salts, electrospray ionization (ESI) is used as a soft ionization source, producing minimal or no fragmentation. The orbitrap mass analyzer and detector is used in the experiments herein, as it provides a high level of resolving power and mass accuracy.

### *1.3.3.1 Electrospray Ionization*

Electrospray ionization (ESI) has become a popular tool for the structural analysis of biological molecules, such as proteins.<sup>13-16</sup> ESI is capable of ionizing microliter volumes at femtomole quantities of analytes that were classically difficult to ionize.<sup>69</sup> ESI was invented by Fenn in the late 1980s and released for commercial use in 1996 after years of improvement, a feat that he was awarded the Nobel Prize for in 2002. Fenn's idea was based off of work by Dole et al. a decade earlier when Dole's group produced a fine spray of charged particles by spraying a dilute aqueous solution via a small tube through a strong electric field.<sup>70, 71</sup> It was Dole's contention that solvent evaporation from the droplets of analyte-containing aqueous solution would eventually cause the charged droplet to reach a critical point at which the surface-charge density would surpass the Rayleigh limit of the droplet. The droplet would then burst apart as Coulombic repulsion overcomes surface tension, causing an explosion that forms several smaller charged droplets (Figure 14). The cycle of charge overcoming surface tension and the resultant Coulombic explosions would continue until the droplet contained only one charged analyte. As evaporation of the droplet reaches a terminal stage, the charge is deposited on the analyte, which is then accelerated through a potential field, into the mass analyzer.<sup>72</sup> Due to the manner in which charge/s is/are deposited, the analyte ion can take on multiple charge states,



giving any mass spectrometer equipped with ESI a much broader mass range, as a mass spectrometer detects the mass-to-charge ratio of an analyte.

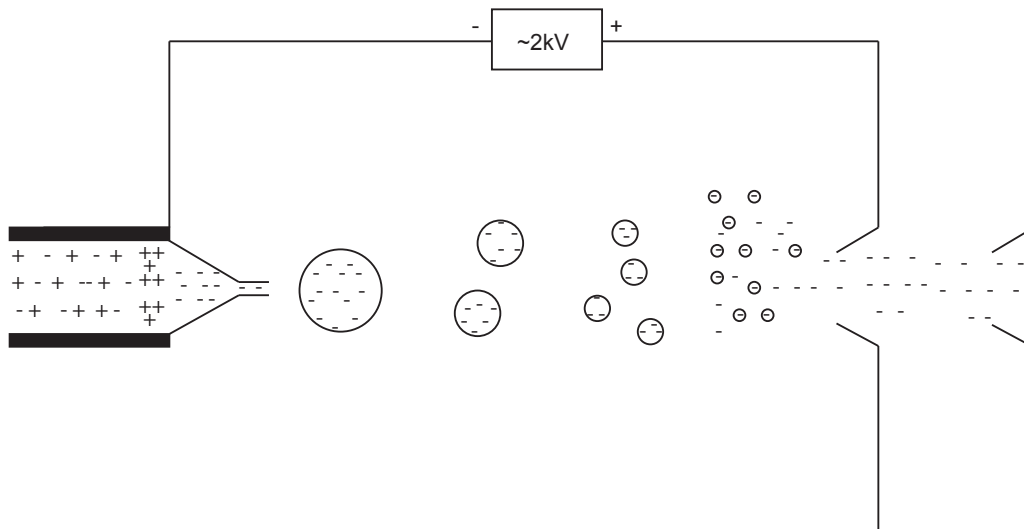


**Figure 14.** Schematic of electro spray ionization in negative ion mode. Ions are being accelerated through charged orifices into the MS.

While the desired ions of analyte are formed, counter charges must also exist to conserve charge. The counter charges are not allowed into the mass spectrometer by properly biased potential differences along the spray capillary, which attracts the counter ions. The desired analyte in solution is allowed into the tip of the spray capillary and is sprayed into an inert gas that aids the evaporation of the solvent. To further aid evaporation, the capillary can also be heated or sprayed into a partial vacuum. Following ionization, the analyte ions are

accelerated through an appropriately biased potential field and into the entrance orifice of the MS, as seen in Figure 14.

### *1.3.3.2 Orbitrap Mass Analysis and Detection*

Due to exceptionally high resolving power and mass accuracy, orbitrap mass analyzers are a popular choice in current applications that require high mass accuracy and/or the analysis of relatively large molecules. Examples of recent uses of orbitrap-based MS include proteomic studies as well as metabolomic, environmental, and food safety studies.<sup>73-75</sup> The orbitrap's power and accuracy stem from the harmonic motion of ions exposed to the electric environment in the mass analyzer. Ions from the ion source are first trapped by a radio frequency field, allowing analytes to be introduced into the mass analyzer in discrete quanta. Upon injection into the orbitrap mass analyzer, ions are initially propelled tangential to the inner, spindle-like electrode, causing them to rotate about the electrode with elliptical trajectories. The geometry of the cavity and an offset injection trajectory result in the "left to right" oscillation of the orbiting ions. The oscillatory movement of the ions is detected by two metal pieces, which produce an image current (Figure 15).

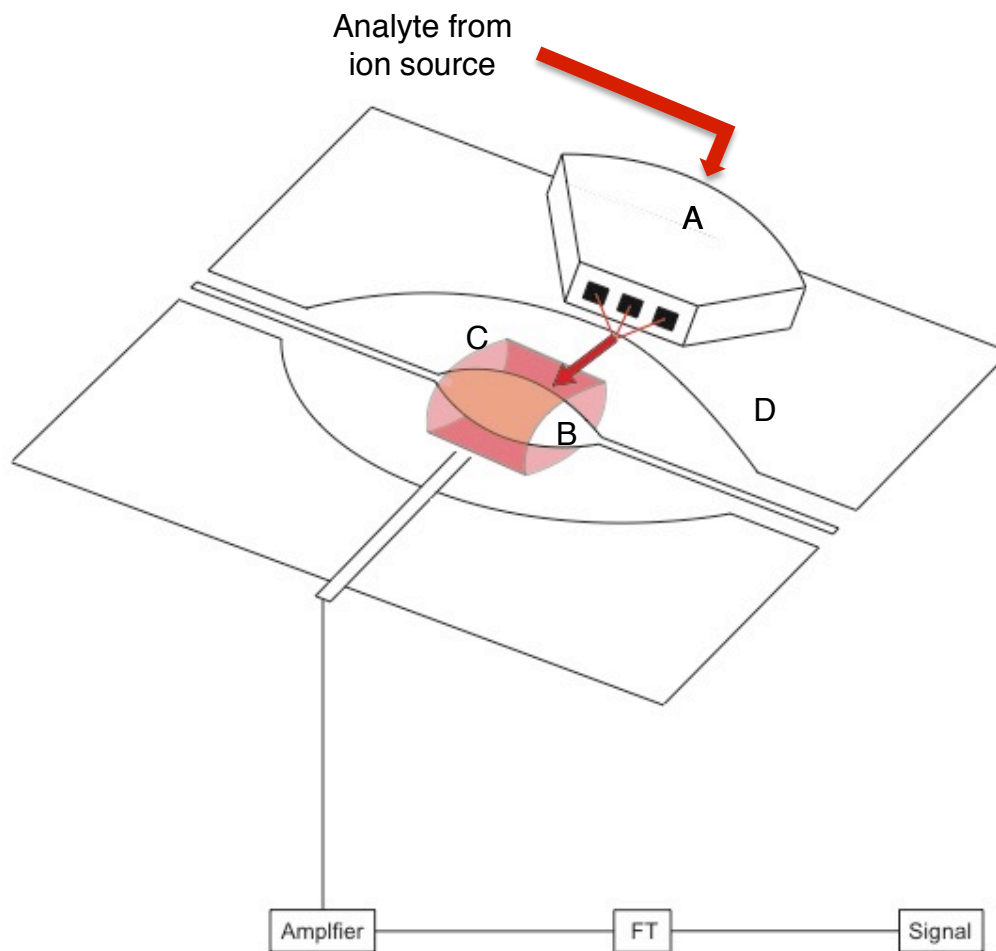


**Figure 15.** A diagram of an orbitrap mass analyzer with ion trajectory in red. *A* Ion trap. *B* Inner, spindle-like electrode. *C* Possible ion trajectories while orbiting the inner electrode. These pathways are elliptical orbits that oscillate from one end of the spindle to the other. *D* Outer electrode.

Due to the barrel like shape of the outer electrode (Figure 15, D) and the spindle-like shape of the inner electrode (Figure 15, B), the electric field in the analyzer has a quadro-logarithmic potential distribution. The non-uniform potential field causes ions to oscillate from one side of the spindle to the other (“left to right” along the axis of the spindle), passing the detector as the ion rotates around the spindle in an elliptical trajectory. The oscillatory motion is harmonic, dependent on only mass-to-charge, and easily characterized. The axial frequency ( $\omega_z$ , rad/sec) of a harmonic oscillator can be described, equation 10, as

$$\omega_z = \sqrt{k/(m/z)}, \quad (10)$$

where  $k$  is the spring constant, which is unique to each orbitrap, and  $m/z$  is the mass-to-charge ratio.<sup>76</sup> In order to utilize the relationship shown in equation 10, the image current, which is in the time-domain, must be converted into the frequency-domain by Fourier transform. Once a Fourier transform is performed, angular frequency of an ion is determined.

#### 1.3.4 Bile Salts and MS

Bile salt aggregation has yet to be thoroughly investigated by MS. In 2000, Rodriguez and Yost performed ESI-MS with an ion trapping mass analyzer on solutions of sodium cholate, sodium taurocholate, and sodium taurodeoxycholate in positive ion mode. Each bile salt solution was comprised of between 0.1 and 13 mM bile salt, with 10 mM ammonium acetate, 10 mM sodium or potassium

acetate, and adjusted to pH 7 with solutions of ammonium hydroxide, sodium hydroxide, potassium hydroxide, or acetic acid. With these solutions, Rodriguez and Yost were able to detect a range of aggregates with a maximum aggregation number of 17 for cholate, 20 for taurocholate, and 29 for taurodeoxycholate. Rodriguez and Yost also found that, while cholate aggregates only could take on two positive charges, taurocholate and taurodeoxycholate aggregates could take on three and four positive charges per micelle, respectively.<sup>14</sup>

In 2005, Nohara, Kajiura, and Takeda performed ESI-MS on 15-40 mM sodium cholate aqueous solutions with varying amounts of ethanol. The Nohara group found that aggregation numbers ranged from 2 to 9 without ethanol, and the average aggregation number decreased linearly with increasing ethanol content.<sup>16</sup>

In the work herein, using the phase-transition model and PCA on proton NMR data will show cholate CMC determination. The CMCs derived from these methods will guide the selection of samples on which to perform HSQC. Due to the care taken in the selection of these samples, structural information regarding different bile salt aggregation steps can be inferred. In addition, high-resolution orbitrap-based electrospray ionization will be used to investigate the aggregation number of cholate aggregates.

## 2. Experimental

### 2.1 Reagents

Cholic acid ( $\geq 98\%$  purity) and R,S-1,1'-binaphthyl-2,2'-diyl hydrogen phosphate (97% purity) were obtained from Sigma-Aldrich Chemical Company (St. Louis, MO, USA). Sodium hydroxide was obtained from Fisher Scientific (Fairfield, NJ, USA). Deuterium oxide (99% D) was obtained from Cambridge Isotope Laboratories, Inc. (Andover, MA, USA). All chemicals were used without further purification. Sodium cholate x-hydrate is not used, as the level of hydration is not known. Because the level of hydration is not known, an exact molar mass of sodium cholate x-hydrate is now known with any certainty.

### 2.2 Instrumentation

All NMR spectra were collected at Bucknell University with a Varian Direct Drive 600 MHz spectrometer (Palo Alto, CA, USA) equipped with a 5 mm Varian HCN triple resonance probe with WATERGATE suppression of water signals using VnmrJ version 3.2 software from Varian. NMR spectral analysis and manipulation was performed using iNMR (nucleomatica, <http://www.inmr.net>). Mass spectra were acquired on a Thermo Scientific Exactiv mass spectrometer with electrospray ionization (Waltham, MA, USA) using Thermo Exactiv Tune and Thermo Xcalibur 2.1 software.

### *2.2.1 MS Parameters*

Parameters for the mass spectrometry performed herein are as follows: HCD (fragmentation) gas off; mass range of 200-3000 m/z; negative ion mode; sheath gas of 14; spray voltage was 2.5 kV; the capillary temperature was 275°C; the capillary voltage was -75 V; the tube lens voltage was -145 V; the skimmer voltage was -22 V; the inlet heater was set to off; the sweep gas was varied between 1 and 8, with the goal of keeping the total ion count below  $1 \times 10^9$ ; the flow rate was 30  $\mu\text{L}/\text{min}$  and the composition of the mobile phase was 90% 18M $\Omega$ ·cm water and 10% methanol.

### **2.3 Standard Solutions for NMR**

Stock solutions of 200.0 mM sodium cholate were prepared by dissolving approximately 20.427 g (5.000 mmol) of cholic acid in one equivalent (5.000 mmol) of sodium hydroxide and  $\sim 175$  mL of 18M $\Omega$ ·cm in a 250 mL volumetric flask water with sonication, heat, and stirring. The solution was allowed to return to room temperature and the magnetic stirring bar was removed prior to the final dilution in the volumetric flask. Such a procedure yields a solution of sodium cholate with a pH of approximately 7.25. Stock solutions of 6.25 mM BNDHP were also prepared as needed by dissolving 0.544 g (1.560 mmol) of either S- or R-BNDHP in one equivalent (1.560 mmol) of sodium hydroxide and  $\sim 175$  mL of 18M $\Omega$ ·cm water with sonication, heat, and stirring. The solution was allowed to

return to room temperature, and the stir bar was removed prior to the final dilution. Such preparation of BNDHP yields a solution with a pH of around 3. Cholates/BNDHP mixtures, herein referred to as “samples,” were made by adding an aliquot of the 200 mM sodium cholate solution with a volume equal to that needed to yield a final solution with a concentration of cholate between 1 and 80 mM in 25.00 mL (62.5  $\mu$ L to 5 mL). A 10.00 mL aliquot of 6.250 mM BNDHP solution was then added to the aliquot of sodium cholate, giving every sample a BNDHP concentration of 2.500 mM. Then, 2.500 mL of deuterium oxide was added to give each sample deuterium composition of 10%. Aqueous samples need to be composed of at least 10% deuterium in order to establish an acceptable lock. Finally, the pH of the samples were adjusted to pH = 12.0 in the 25 mL volumetric flasks, using sodium hydroxide (2M, 0.1M, and/or 0.01M) and 18M $\Omega$ ·cm water. The samples were mixed by shaking upon addition of water or sodium hydroxide prior to their pH being retested.

#### **2.4 Standard Solution for MS**

A stock solution of 100.0 mM sodium cholate was prepared by dissolving 4.085 g (10.00 mmol) of cholic acid in one equivalent (10.00 mmol) of sodium hydroxide and ~60 mL of 18M $\Omega$ ·cm water in a 100 mL volumetric flask. The stock was then diluted using 18M $\Omega$ ·cm water to make 25 mL solutions with concentrations of 1, 3, 5, 7, 9, 11, 13, 15, 20, 30, 40, 70, 80, and 100 mM sodium cholate.



### 3. Results and Discussion

#### 3.1 Critical Micelle Concentration Using Nuclear Magnetic Resonance Spectroscopy

One-dimensional (1D) proton ( $^1\text{H}$ ) nuclear magnetic resonance spectroscopy (NMR) can be used to determine the CMC for systems of cholate aggregates.<sup>1</sup> When aggregation of cholate occurs, two or more cholate monomers will bind to one another changing the chemical environments of the protons of cholate. The perturbation of chemical environments will be detected on the NMR spectra, as the signals of the affected cholate protons will move based on the type of environments the protons encounter. However, several of the cholate aliphatic protons have very similar chemical shifts, giving the cholate NMR spectrum ambiguity, making it difficult to assign each signal to a particular proton. With the use of a probe molecule, such as 1,1'-binaphthyl-2,2'-diyl hydrogen phosphate (BNDHP) (Figure 16, inset) a CMC for the cholate micelle system can be determined based on the chemical shift perturbations of BNDHP. BNDHP is known to be attracted to the binding pocket of formed cholate micelles and makes a convenient probe molecule for NMR analysis of cholate micelles because the chemical shifts of BNDHP protons is in a region that does not overlap with chemical shifts of cholate protons. If the NMR spectra of BNDHP in increasing concentrations of cholate are vertically stacked in order of increasing

cholate concentration, the onset of BNDHP chemical shift perturbation – the CMC of the cholate micelle system – is determinable by inspection (Figure 16).

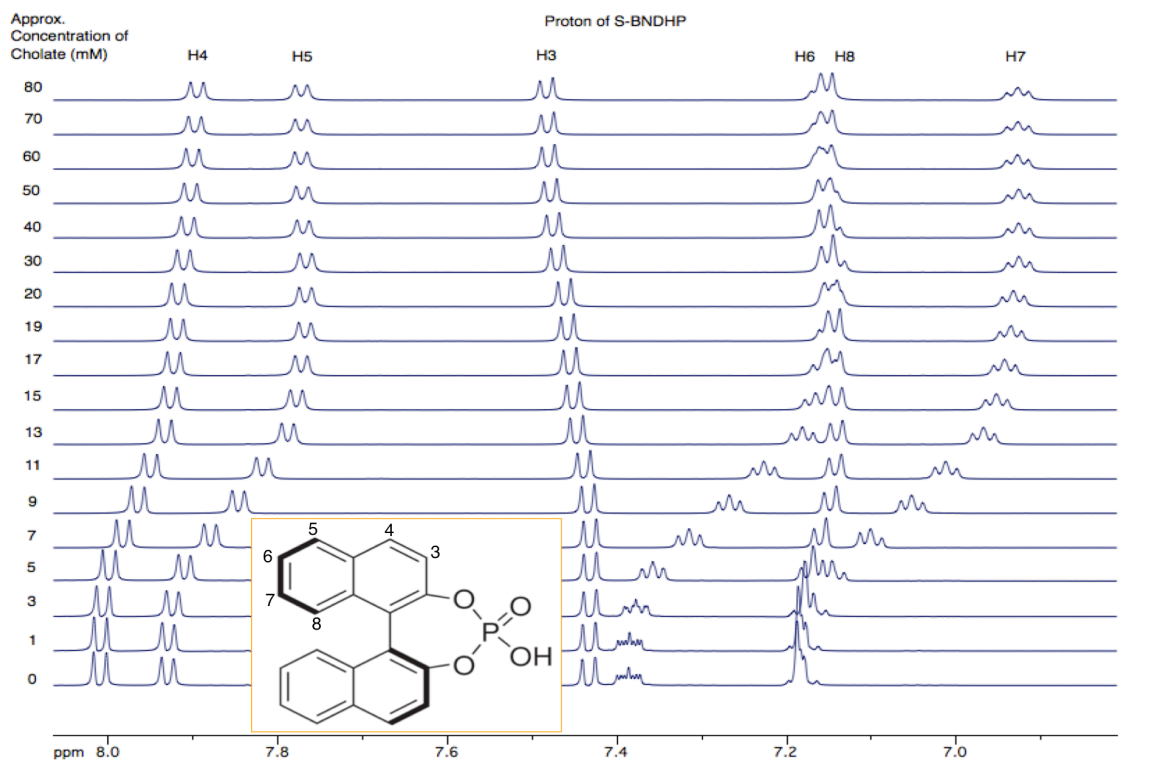


**Figure 16.** NMR spectra of 2.5 mM S-BNDHP in varying concentrations of sodium cholate at pH 12. Spectra were recorded at different concentrations of sodium cholate, ranging from 0-80 mM at pH = 12, and vertically stacked in consecutive concentrations. *Inset* The structure of S-BNDHP with positions numbered for convenience.

Several CMCs can be interpreted from Figure 16. BNDHP H4-H8 detects the preliminary CMC, or formation of a dimer; the chemical shifts of these protons change between 5 and 7 mM cholate. BNDHP H3 detects the primary CMC, or formation of an aggregate thought to have an AN between 2 and 10, when the proton's chemical shift is perturbed between 11 and 13 mM cholate. Finally, a secondary CMC, for an aggregate consisting of greater than ten monomer units, is detected by H4, whose chemical shift is perturbed between 20 and 40 mM cholate.

### 3.1.1 The Phase-Transition Model

Mathematic modeling was used to analyze 1D  $^1\text{H}$  NMR data, using a phase-transition model (equation 8, page 26). The chemical shift of each BNDHP proton was recorded for each concentration of sodium cholate and plotted logarithmically against the logarithm of the concentration of sodium cholate. The log-log style of plotting was utilized to prevent the model from being disproportionately biased by data collected at high sodium cholate concentrations. For signals split into an even-numbered multiplicity, the average of the chemical shifts was taken to be the chemical shift of that proton; for signals split into an odd-numbered multiplicity, the chemical shift of the central signal was taken to be the chemical shift of the proton. The phase-transition model, which treats a solution as a weighted average of free and bound monomer, is

manipulated by two parameters, the chemical shift of bound monomer and the CMC of the system. When the phase-transition model was plotted so that the model fit as many as the physical observations as possible, the CMC of cholate as experienced by every proton of BNDHP was determined, accounting for chemical environment differences experienced throughout the probe molecule. Figures 17 through 22 show the log-log plots of both the observed chemical shift data from 1D proton NMR on protons from 2.5 mM S-BNDHP and a model of expected chemical shifts for selected values of CMC,  $\delta_{\text{bound}}$ , and  $\delta_{\text{free}}$ . The CMC is the point of the initial deviation from linearity. The CMC differs from figure to figure as different protons of BNDHP may sample different local environments in the various aggregation stages of cholate. For example, while H5 of BNDHP may be in the middle of the cholate dimer binding pocket, a very hydrophobic environment, H3 of BNDHP may be more solvent-exposed, a more hydrophilic environment than the binding pocket. Because H3 of BNDHP is more solvent-exposed, that proton may be sensitive to a different aggregation step than the protons in the binding pocket. The data shown in Figure 16 and Figures 17-22 agree in that H3 of BNDHP indeed samples a different aggregation stage of cholate than the other protons of BNDHP. While most protons of BNDHP experience a cholate CMC of around 6.5 mM, H3 samples a cholate aggregate that has a CMC of 11 mM (Figures 17-22). The idea that H3 is in a more solvent-exposed position is also supported by the direction that the chemical shifts are

perturbed. Shifts to higher frequencies on a 1D  $^1\text{H}$  NMR are said to be hydrophilic shifts, meaning that the proton is coming into a more hydrophilic environment. Perturbations that cause the chemical shifts to appear in a lower frequency are said to be hydrophobic shifts. As seen in Figure 16, most of the protons of BNDHP experience hydrophobic perturbations. H3 is the only proton that experiences a hydrophilic perturbation.

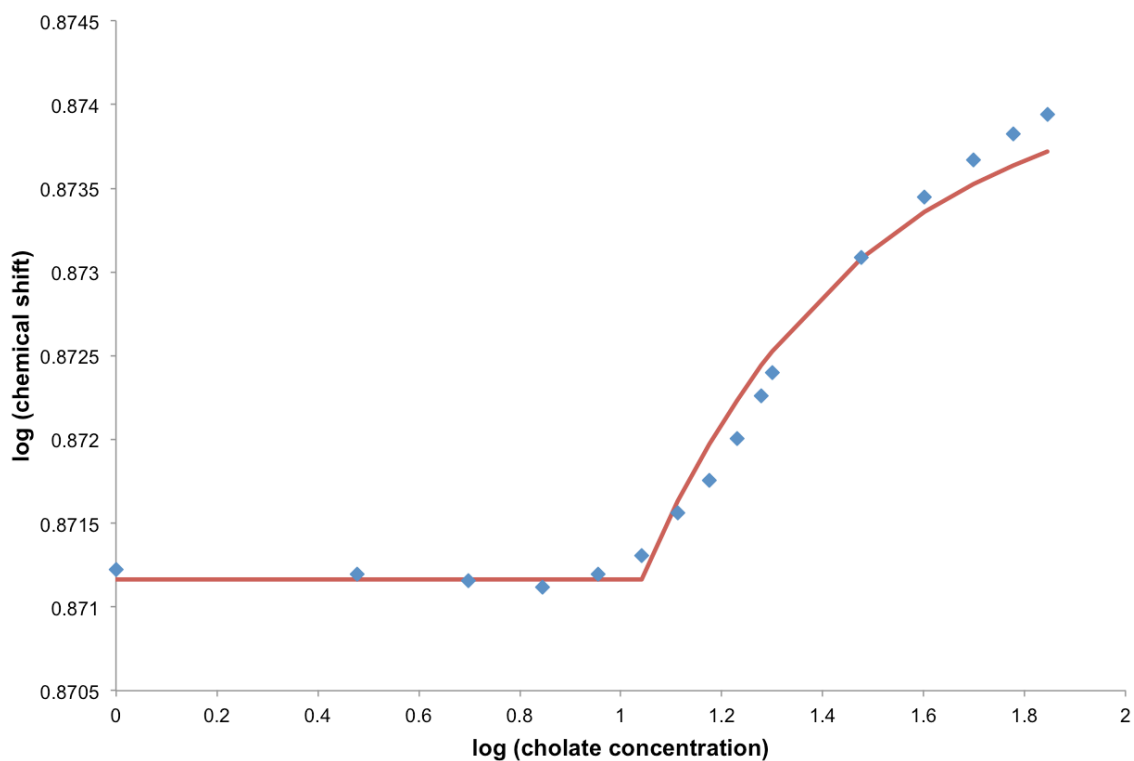


**Figure 17.** Modeling of S-BNDHP H3 chemical shift data. The diamonds are the experimental data. The line shows predicted chemical shifts based on the phase-transition model, which yielded a cholate CMC of 11 mM.

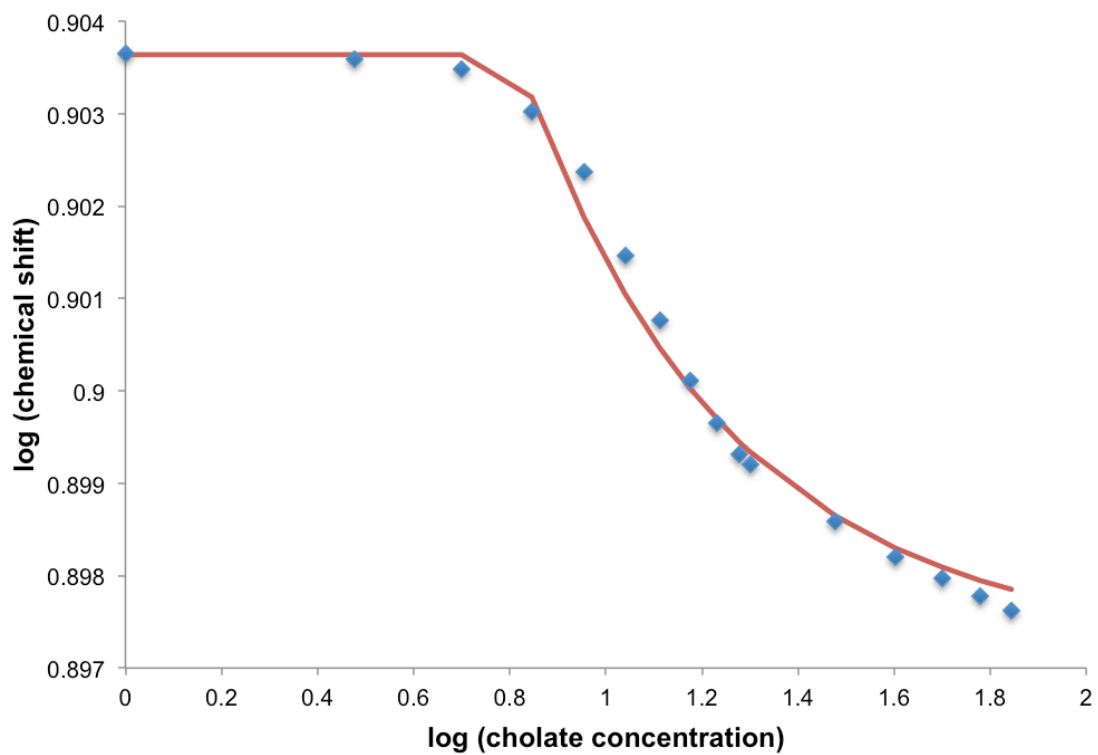


**Figure 18.** Modeling of S-BNDHP H4 chemical shift data. The diamonds are the experimental data. The line shows predicted chemical shifts based on the phase-transition model, which yielded a cholate CMC of 6.5 mM.

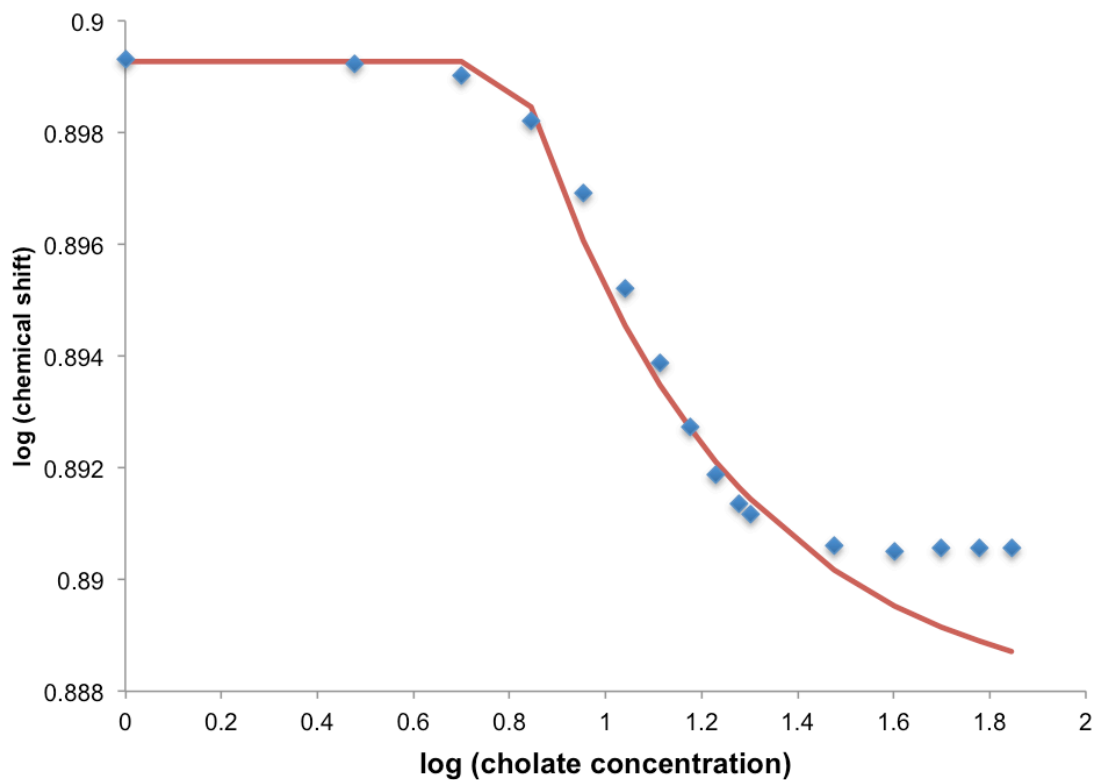


**Figure 19.** Modeling of S-BNDHP H5 chemical shift data. The diamonds are the experimental data. The line shows predicted chemical shifts based on the phase-transition model, which yielded a cholate CMC of 6.5 mM.

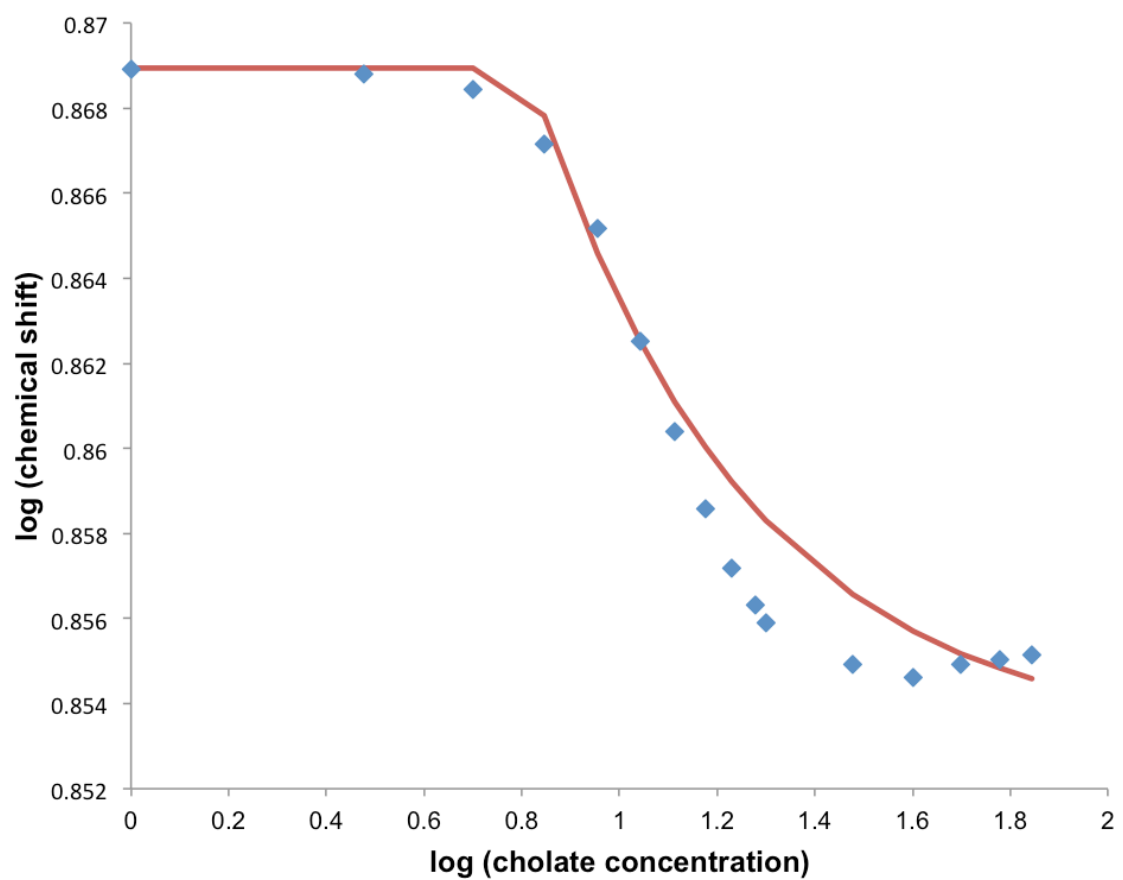


**Figure 20.** Modeling of S-BNDHP H6 chemical shift data. The diamonds are the experimental data. The line shows predicted chemical shifts based on the phase-transition model, which yielded a cholate CMC of 6.5 mM.



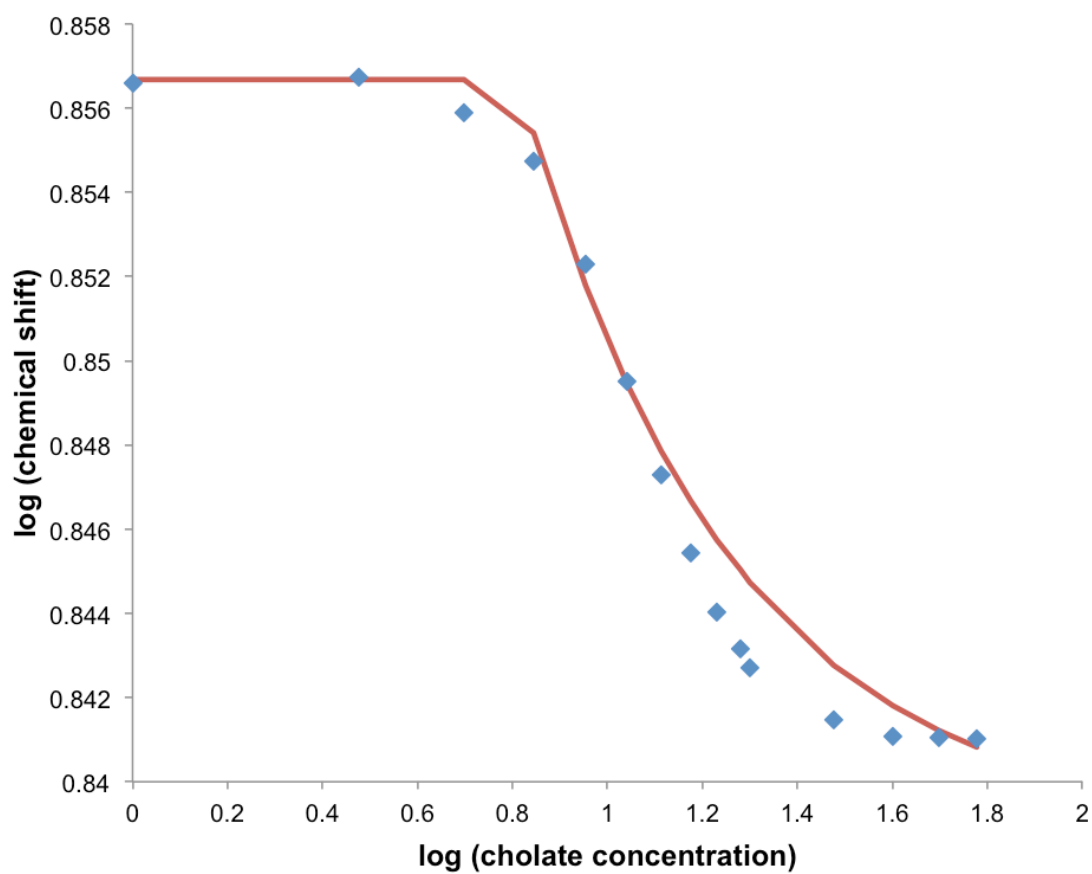


**Figure 21.** Modeling of S-BNDHP H7 chemical shift data. The diamonds are the experimental data. The line shows predicted chemical shifts based on the phase-transition model, which yielded a cholate CMC of 6.5 mM.

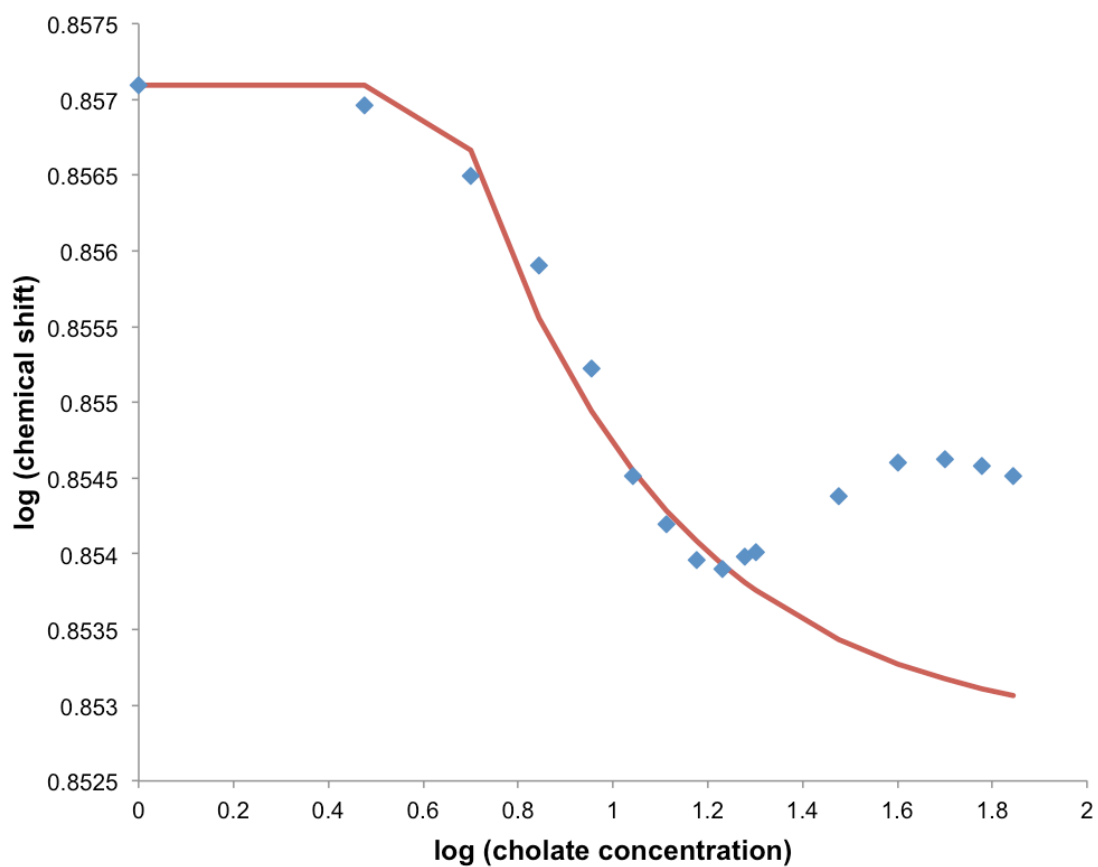


**Figure 22.** Modeling of S-BNDHP H8 chemical shift data. The diamonds are the experimental data. The line shows predicted chemical shifts based on the phase-transition model, which yielded a cholate CMC of 4.5 mM.

The CMCs experienced by different protons of S-BNDHP based on phase-transition modeling can be seen in Table 3. Using the phase-transition model, there was evidence for at least two aggregation states for sodium cholate at pH 12 and 25°C with an S-BNDHP probe. The CMCs of the cholate micelle system for two of the states were found to be approximately 6.1 and 11.0 mM. The existence of these two aggregation states is supported by Small's model where at lower concentrations a preliminary aggregate that is consistent with a dimer, will form and at moderate concentrations an aggregate will form with an aggregation number between 2 and 10, referred to as the primary aggregate.<sup>20</sup>

**Table 3. CMC of Cholate as Determined by Phase-Transition Modeling**

BNDHP Proton	CMC (mM)
H3	11.0
H4	6.5
H5	6.5
H6	6.5
H7	6.5
H8	4.5

### 3.1.2 Principal Component Analysis for CMC Determination Using

#### NMR Data

Given the phase-transition model's pitfalls of potential bias, from the mathematic assumptions made in deriving the model, and imprecision, from the human guidance required in using the model, as discussed in the introduction, another method may give a more accurate CMC determination. Principal component analysis (PCA) is a method of data treatment that can make subtle variances and trends in data more accessible. In this work, PCA was performed using MATLAB software by making a matrix out of the proton-labeled chemical shift and concentration data. Entering the chemical shift and concentration data into MATLAB can be accomplished by entering the BNDHP proton chemical shift data as the variables in the x-axis of the matrix at varying cholate concentrations along the y-axis (Table 4). When PCA is performed, the loading of every variable in each principal component is determined the data set. Variables are data that vary based on the observables in a data set, chemical shift in this experiment. The loading is a number that describes how affected a variable is by a principal component. Ideally, several variables will have similar variances in a data set and will cluster together when plotted, which is evidence that the variables may be related. When PCA was performed on the data set from Table 4, a bi-plot

combining a score plot and a loadings plot, shown in Figure 23, was created, which plots the loading from principal component 1 (PC1) along the x-axis and the loading from principal component 2 (PC2) along the y-axis.

**Table 4. Matrix upon which PCA was Performed Treating the Chemical**

**Shifts as Variables**

Concentrations of Cholate (mM)	Protons of BNDHP					
	H3	H4	H5	H6	H7	H8
1	7.44375	8.0125	7.93375	7.33875	7.18375	7.19625
3	7.43374	8.01125	7.93125	7.38625	7.17875	7.19375
5	7.43375	8.00875	7.92625	7.38125	7.17125	7.1875
7	7.43375	8.00125	7.91375	7.36375	7.15125	7.18
9	7.43375	7.98375	7.88125	7.31625	7.10125	7.16375
11	7.43625	7.97375	7.8625	7.28875	7.07375	7.1575
13	7.44	7.9625	7.84125	7.25625	7.04125	7.1525
15	7.44625	7.94625	7.8125	7.21375	6.99875	7.1475
17	7.44875	7.93875	7.80124	7.19875	6.98375	7.14624
19	7.45125	7.93375	7.79125	7.18125	6.96625	7.14625
20	7.45375	7.92875	7.78625	7.17375	6.95875	7.1475
30	7.46625	7.91625	7.7725	7.16125	6.93375	7.14375
40	7.47375	7.91125	7.77375	7.15125	6.93125	7.145
50	7.47875	7.90625	7.77375	7.15125	6.93125	7.14625
60	7.47875	7.90375	7.77375	7.15625	6.93125	7.1525
70	7.48125	7.90875	7.775	7.16125	6.93125	7.14875
80	7.48375	7.89625	7.775	7.16125	6.93125	7.155

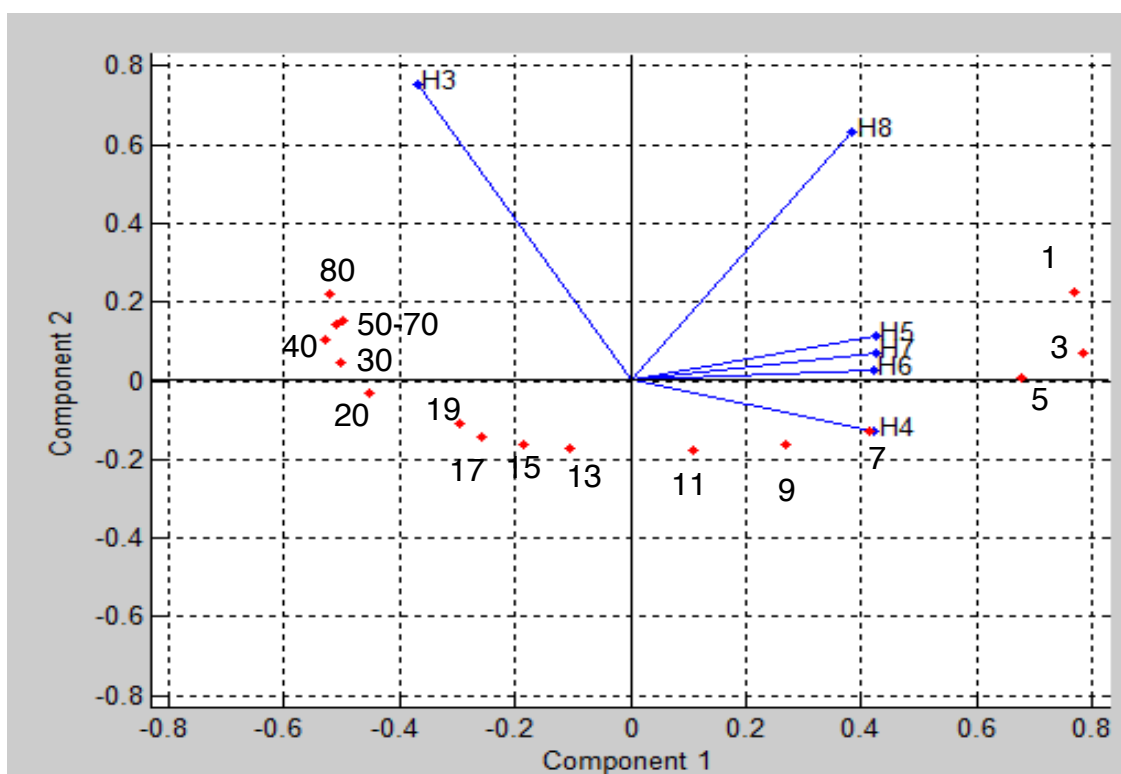


**Figure 23.** Score plot of matrix in Table 4, lines indicate BNDHP protons, dots indicate cholate concentrations, shown, in mM. The axes show how the data represented by lines and dots are affected by principal component 1 and principal component 2.

By looking at where the dots and lines lie on the plot and using prior knowledge about the system, a good first approximation of the identities of the principal components is that component 1 has to do with stage of the aggregation and component 2 has to do with the type of interactions occurring at that proton or concentration. The exact identities or variables that comprise each component

is not explicitly known, however based on what prior experiments have shown about the system in regards to the CMCs and the kind of interactions that occur at different aggregation steps, the stated identities of the principal components are plausible. Several interesting pieces of information can be inferred from Figure 23. The loadings for H4-H7 cluster, indicating that these protons have chemical shifts that were perturbed at nearly the same concentration of cholate. The loading of H3 is in an entirely different quadrant, which suggests that the chemical shift of proton H3 was perturbed in a totally opposite manner. The changing chemical environment experienced by the protons of BNDHP shown by PCA can be seen in NMR as a hydrophilic shift for H3 and a hydrophobic shift for H4-8. While the behavior of the protons of BNDHP shown by PCA was not previously unknown, the behavior did give credence to the method's ability to highlight what was physically happening in solution. The scores of the concentrations, however, appeared to be much more interesting. The dots on the score plot represent different concentration of cholate. When the principal component scores of the different cholate concentrations are plotted, their representative dots form an arc passing through all four quadrants (Figure 23). Interestingly, each time the arc crosses an axis, the cholate concentrations near the axis crossings are very similar to critical micelle concentrations of cholate. The axis crossings occurred at approximately 5 mM, a concentration thought to be where a dimer would first form, around 12 mM, a concentration that primary

aggregation has been seen, and around 25 mM, a concentration that is theorized to be where secondary aggregation may occur. The concentrations seen at the axis crossings are conspicuously close to the CMC values found using the phase-transition model, therefore it is reasonable to assume that PCA may have the potential to determine CMC values for the cholate aggregate system.

Another interesting observation was that concentrations after the secondary micelle CMC had scores that were in the same quadrant as the loading of H3. H3 was differentiated from the other protons of BNDHP due to its hydrophilic chemical shift perturbation. According to Small's model, the secondary micelle is formed by hydrophilic interactions, which might be verified by PCA. PCA for CMC determination remains a novel and under-investigated method for accurate CMC determination in the cholate micelle systems. From PCA data, a more accurate CMC may be found.

### **3.2 Micellar Structural Elucidation by Heteronuclear Single Quantum**

#### **Coherence Spectroscopy**

The structure of the cholate micelle system has been the subject of much debate since Small's model was published in 1968.<sup>20-22</sup> Heteronuclear single quantum coherence spectroscopy (HSQC) is a two-dimensional (2D) NMR technique that pairs the signal of a proton with, in this case, the  $^{13}\text{C}$  that the proton is bonded to. HSQC, therefore, allows for the probing of chemical



environments of bonded  $^1\text{H}$ - $^{13}\text{C}$  pairs with atomic resolution and may allow for the mapping of these chemical environments onto a molecule. The mapping of chemical shift perturbations as seen by HSQC for cholate was made possible by Ijare who identified the  $^1\text{H}$ - $^{13}\text{C}$  pair that gave rise to each signal on an HSQC spectrum.<sup>3</sup> The structure of cholate with labeled carbon is reproduced in Figure 24, for convenience.

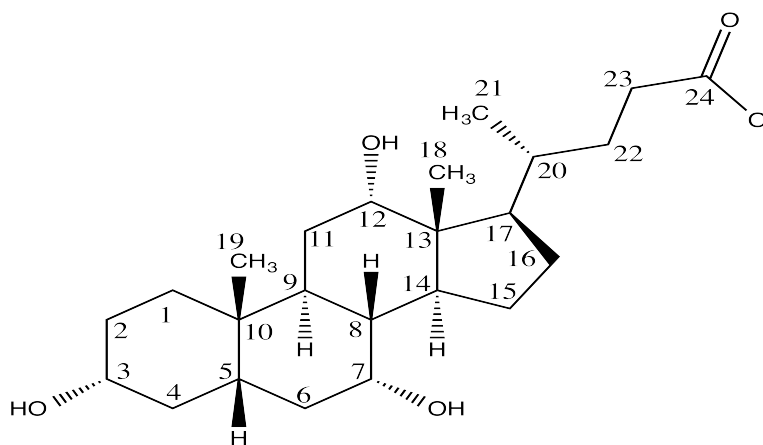


**Figure 24.** Structure of cholate with numbered carbons.

Because HSQC can take up to 18 hours on a 600 MHz instrument, it was decided that HSQC would be performed on only five representative samples of cholate at different aggregation stages. To sample each suspected aggregation stage of the cholate micelle, the concentrations of cholate that spectra were recorded for in each of the following experiments was 3, 11, 20, 30, and 80 mM at pH 12. Plots were constructed, overlaying the HSQC spectra from the five

concentrations to visualize trends. Three plots were constructed; one where each sample contained 2.5 mM S-BNDHP (Figure 25), one where each sample contained 2.5 mM R-BNDHP (Figure 26), and one where no probe molecule was used (Figure 27).

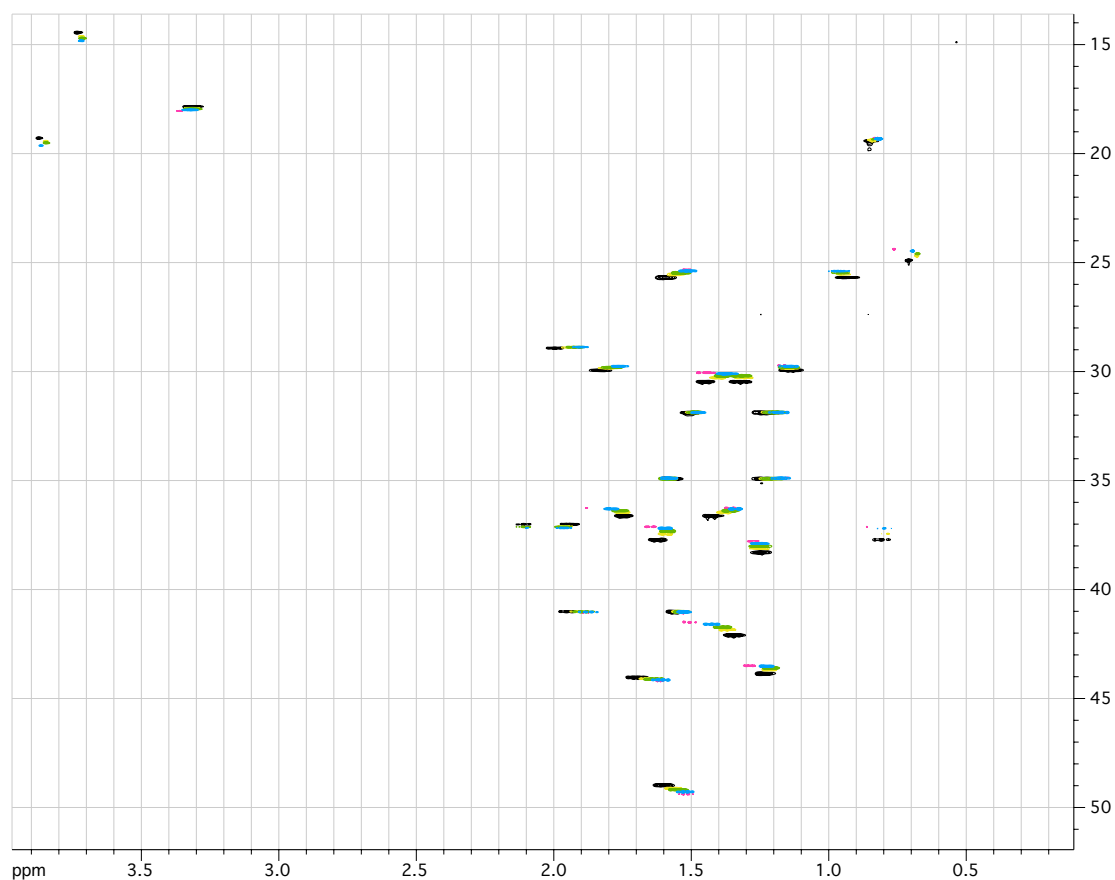


**Figure 25.** Plot of an overlay of several  $^1\text{H}$ - $^{13}\text{C}$  HSQC spectra from samples at pH 12 containing 2.5 mM S-BNDHP and the following concentrations of sodium cholate: 3 (red), 11 (blue), 20 (green), 30 (yellow), and 80 (black) mM.

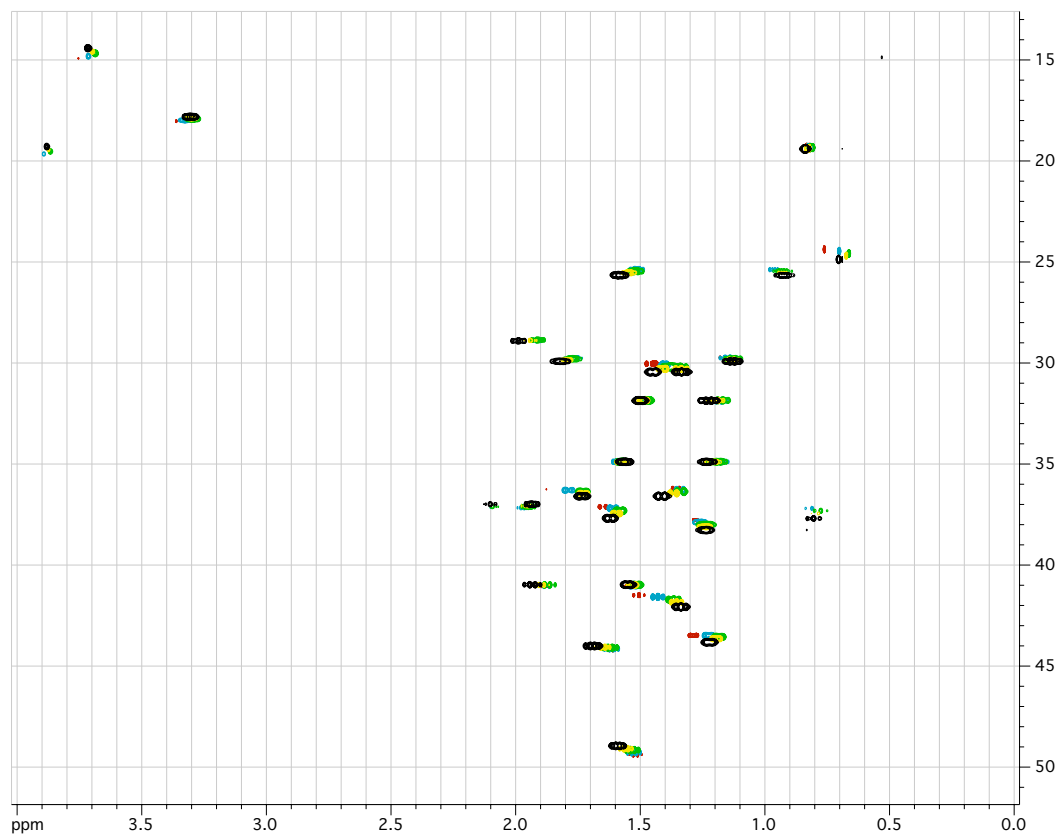


**Figure 26.** Plot of an overlay of several  $^1\text{H}$ - $^{13}\text{C}$  HSQC spectra from samples at pH 12 containing 2.5 mM R-BNDHP and the following concentrations of sodium cholate: 3 (red), 11 (blue), 20 (green), 30 (yellow), and 80 (black) mM.

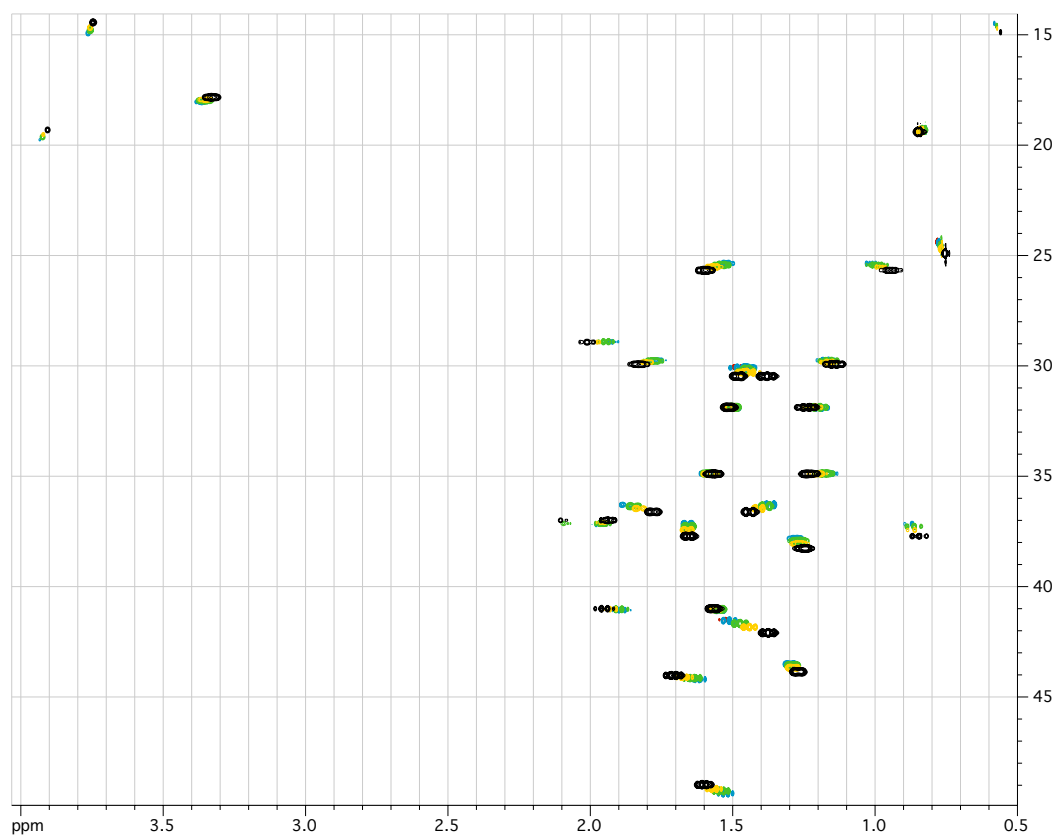


**Figure 27.** Plot of an overlay of several  $^1\text{H}$ - $^{13}\text{C}$  HSQC spectra from samples at pH 12 containing the following concentrations of sodium cholate: 3 (red), 11 (blue), 20 (green), 30 (yellow), and 80 (black) mM.

Changes in the observed chemical shift from concentration to concentration are an indication of aggregation. To map the magnitude and/or type of interaction highlighted by HSQC to a  $^1\text{H}$ - $^{13}\text{C}$  pair in a cholate molecule, the magnitude of each chemical shift perturbation must be calculated. There are two ways to determine the magnitude of chemical shift from the HSQC data; a method that conserves the directionality of the shift, herein referred to as the “conserved” method, and a method that does not conserve directionality and measures the overall magnitude of the chemical shift perturbation, herein referred to as the “absolute” method. The two methods each emphasize different characteristics of the cholate micelle system; the conserved method will show what type of interactions, either hydrophilic or hydrophobic, dominate at different parts of the micelle, while the absolute method will show which parts of the cholate molecule are the most involved in the formation of the cholate micelle. The methods show different information because the type of interaction a carbon-proton pair experiences can be determined by the direction that the chemical shifts are perturbed, which is reported by the sign of the difference in chemical shifts of two consecutive cholate concentrations. Conversely, by taking the absolute value of these differences the total chemical shift perturbation experienced by a carbon-proton pair can be determined, which is a good indication of the extent of aggregation at a particular location on each monomer. For both methods, only the proton chemical shift data are considered.

### 3.2.1 The “Total Walk” Method for Considering Shifts in HSQC Data

The “total walk” method for considering shifts in HSQC data involves determining the magnitude of the perturbation of the chemical shift of each  $^1\text{H}$ - $^{13}\text{C}$  pair as the concentration of cholate is increased from 3 mM to 11 mM to 20 mM to 30 mM to 80 mM. A way to conceptualize this is to think of the odometer of a car. The odometer keeps track of miles in a route-independent way, much like the way the math of the absolute method keeps track of the magnitude of the chemical shift perturbation by adding absolute values. The independence of route achieved by the absolute method is accomplished by finding the distance between two consecutive concentrations of cholate for the same signal arising from a  $^1\text{H}$ - $^{13}\text{C}$  pair, and then summing the distances over the concentration range considered. The absolute perturbation is determined by equation 11

$$\text{"Total Walk" Perturbation} = |X_1| + |X_2| + |X_3| + |X_4|, \quad (11)$$

where  $X_{1-4}$  is the absolute value of the change in proton chemical shift between two consecutive signals, as shown in Figures 28 and 29. The absolute perturbation was determined for each proton-carbon pair and plotted as a bar graph for cholate samples in solution with R- and S-BNDHP. The bar graphs were then grouped into carbon-proton pairs that exhibited strong, medium, and weak perturbations, which are denoted by lines in Figures 30 and 31. Bars representing carbon-proton pairs that extend above a line are considered to be perturbed similarly, shown by the shaded boxes. The lines were drawn in a

manner that would group several bars that seemed to plateau. The strength of these perturbations was then mapped onto the structure of cholate using the characterization of medium and strong perturbation experienced (Figure 29 and 30).

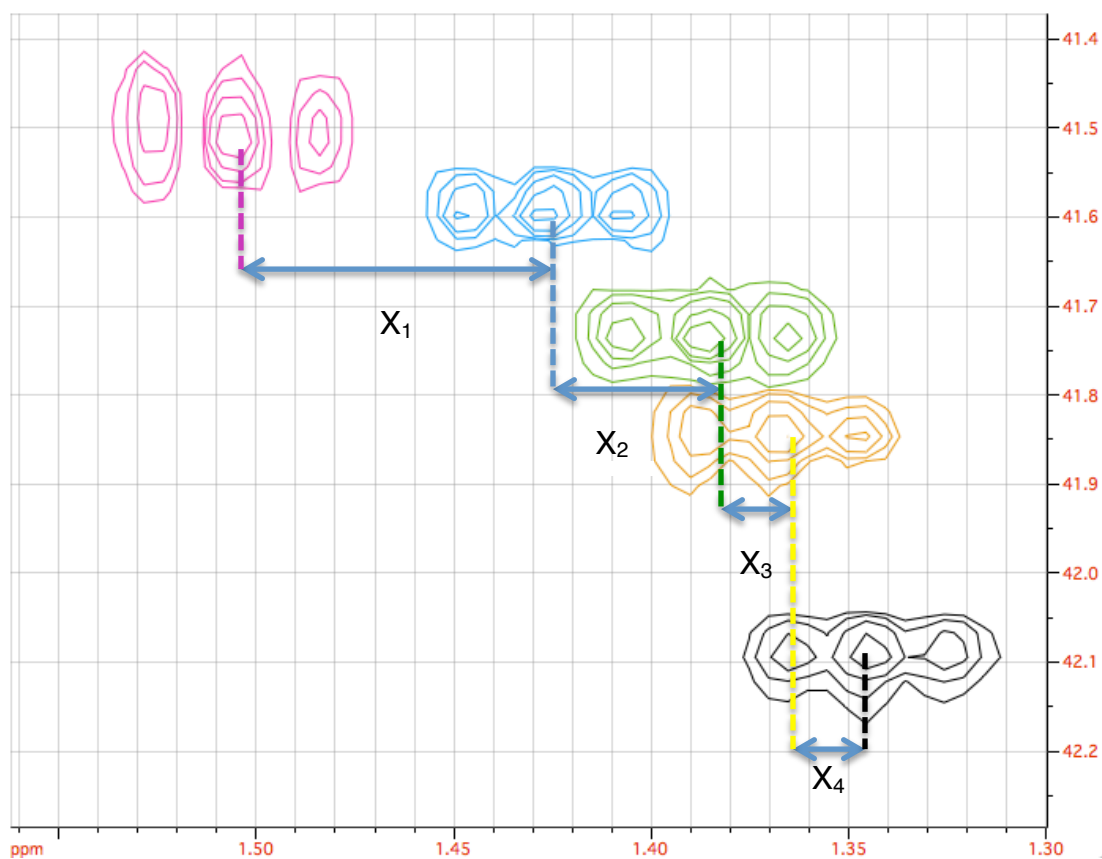


**Figure 28.** Plot of an overlay from HSQC signals for cholate C8 at five different concentrations (3, 11, 20, 30, 80 mM) with 2.5 mM S-BNDHP. The “total walk” magnitude of total chemical shift perturbation was calculated as the sum of the absolute value of  $X_1$ ,  $X_2$ ,  $X_3$ , and  $X_4$ .

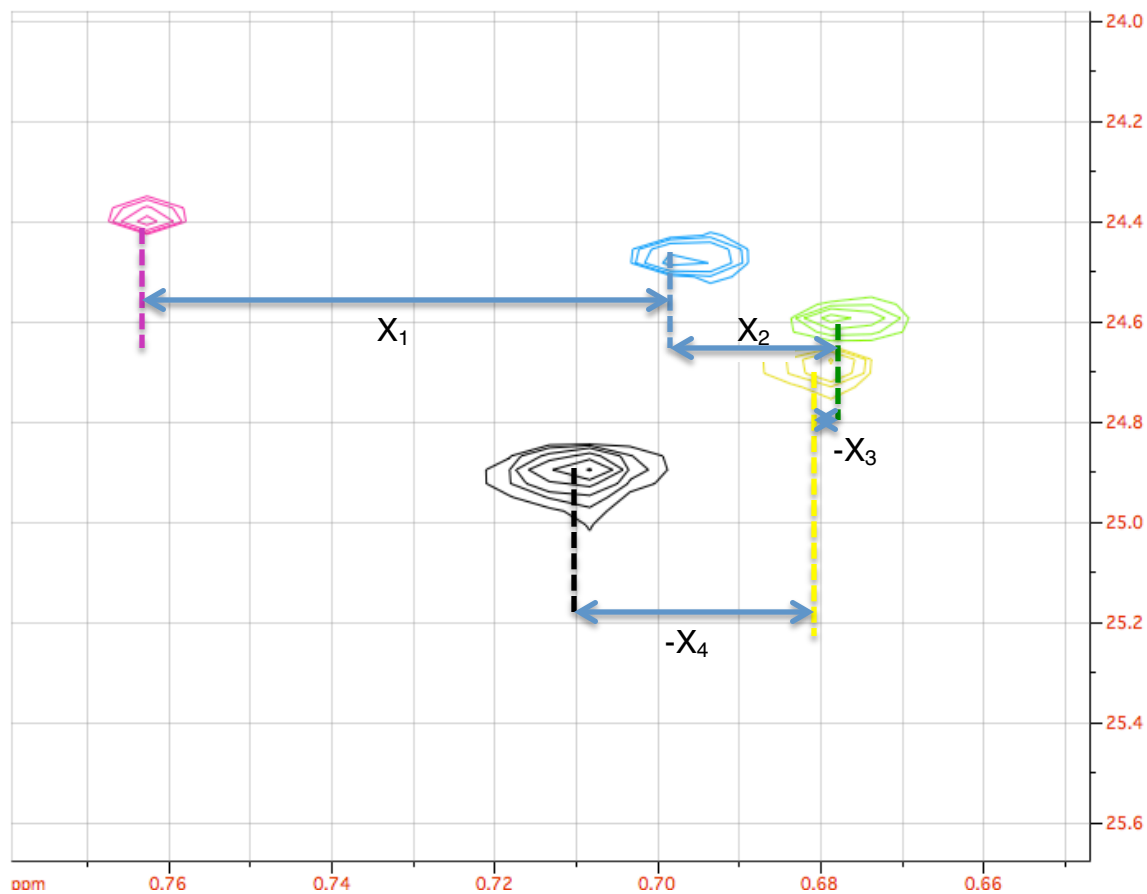


**Figure 29.** Plot of an overlay from HSQC signals for cholate C12 at five different concentrations (3, 11, 20, 30, 80 mM) with 2.5 mM S-BNDHP. The “total walk” magnitude of total chemical shift perturbation was calculated as the sum of the absolute value of  $X_1$ ,  $X_2$ ,  $X_3$ , and  $X_4$ .



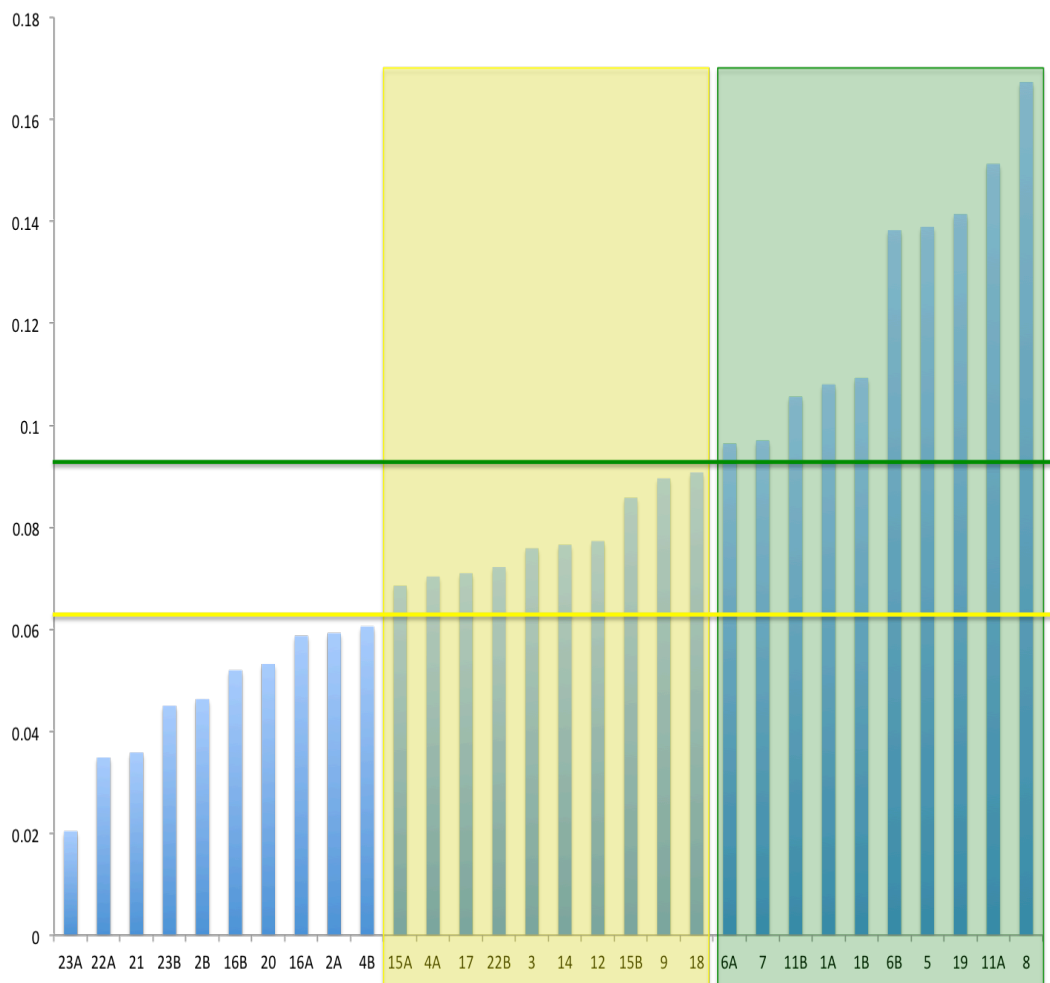


**Figure 30.** A bar graph constructed from the magnitude of “total walk” perturbation in proton chemical shift experienced by carbon-proton pairs of cholate (x-axis) from 3 to 80 mM with 2.5 mM R-BNDHP in solution from HSQC data. Bars above the line at  $\sim 0.06$ , but below the line at  $\sim 0.09$  (in the lightly shaded area) represent pairs with moderate chemical shift perturbation. Bars above the line at  $\sim 0.09$  (in the darker shaded area) represent pairs with a large chemical shift perturbation.

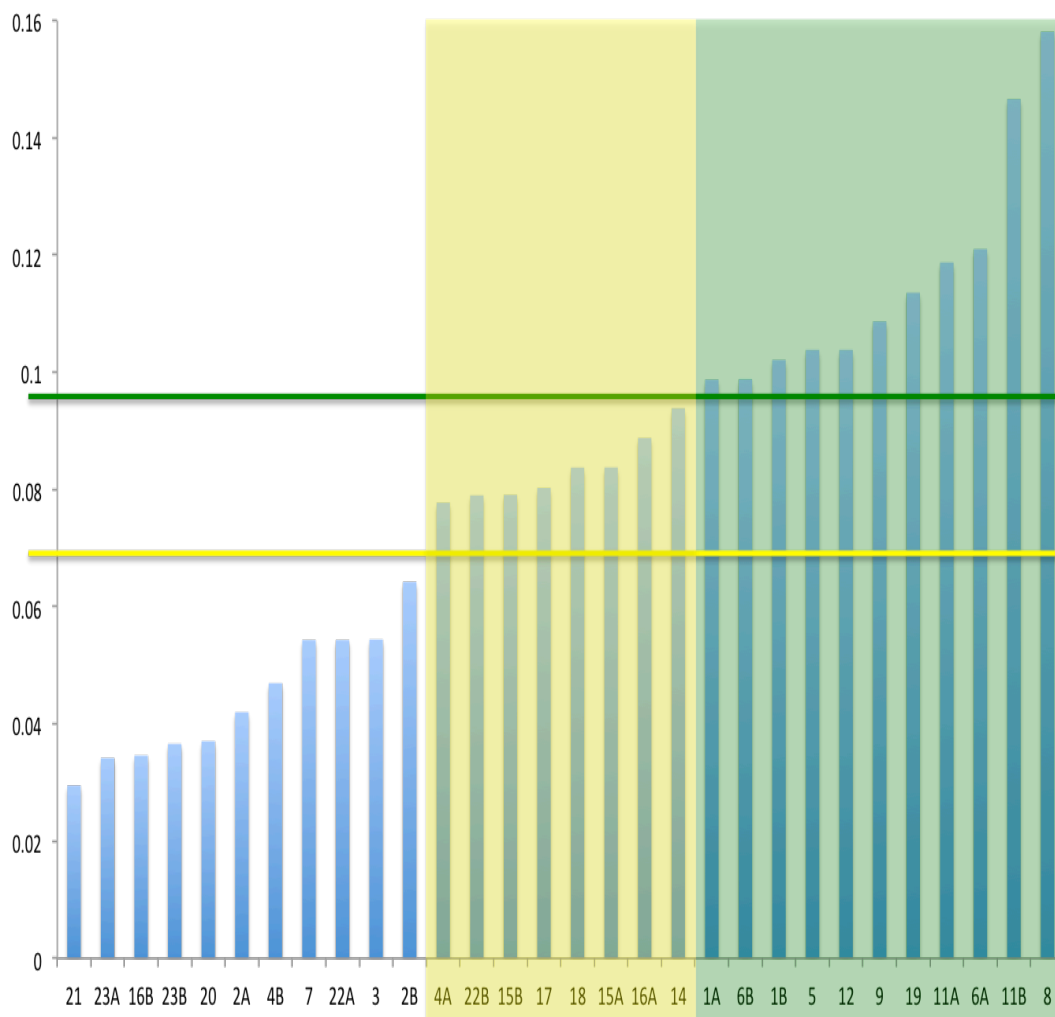


**Figure 31.** A bar graph constructed from the magnitude of “total walk” perturbation in proton chemical shift experienced by carbon-proton pairs of cholate (x-axis) from 30 to 80 mM with 2.5 mM S-BNDHP in solution from HSQC data. Bars above the line at  $\sim 0.07$ , but below the line at  $\sim 0.1$  (in the lightly shaded area) represent pairs with moderate chemical shift perturbation. Bars above the line at  $\sim 0.1$  (in the darker shaded area) represent pairs with a large chemical shift perturbation.

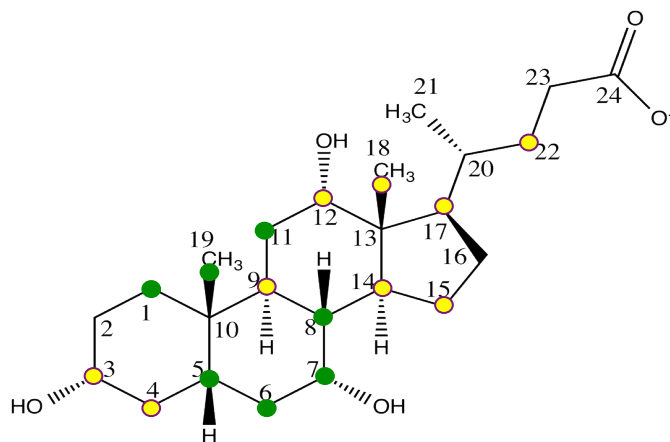


**Figure 32.** Magnitude of “total walk” chemical shift perturbation experienced by carbon-proton pairs, mapped onto the structure of cholate, throughout the process of

aggregation (3 to 80 mM) in the presence of 2.5 mM R-BNDHP. Dark circles represent pairs that experience strong perturbations, while light circles represent pairs that experience moderate perturbations. Remaining pairs experience little or no perturbation.

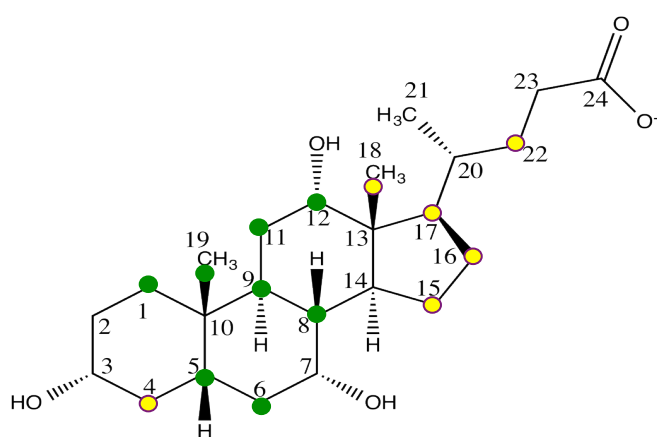


**Figure 33.** Magnitude of “total walk” chemical shift perturbation experienced by carbon-proton pairs, mapped onto the structure of cholate, throughout the process of aggregation (3 to 80

mM) in the presence of 2.5 mM S-BNDHP. Dark circles represent pairs that experience strong perturbations, while light circles represent pairs that experience moderate perturbations. Remaining pairs experience little or no perturbation.

The interaction mapping in Figures 32 and 33 show that the area of highest perturbation for cholate, regardless of which enantiomer of BNDHP is used, is the second six-membered ring containing C6-C10. Furthermore, the area of strong perturbation is nearly surrounded by carbon-proton pairs that experience moderate chemical shift perturbation. Therefore, the mapping of the chemical shift perturbations from HSQC spectra suggests that, instead of two collinear, anti-parallel cholate monomers making up a dimer, that an angle or skew may exist between the two-monomer units. No model of cholate aggregation, including Small's model, has mentioned the presence of this skew before.

Although both R- and S-BNDHP indicate the possible presence of a skew between the two monomers composing a dimer, when the bar graphs depicting proton chemical shift perturbation in the presence of R- and S-BNDHP data are overlaid, additional information can be extracted. Figure 34 depicts the differences in the total magnitude of absolute chemical shift perturbation between a series of five concentrations of cholate with 2.5 mM R-BNDHP compared to a series of five concentrations of cholate with 2.5 mM S-BNDHP. If the difference between the R- and S-BNDHP data sets was greater than 0.01, that carbon-proton pair was assigned a dot corresponding to whichever atropisomer of BNDHP caused the greatest perturbation.

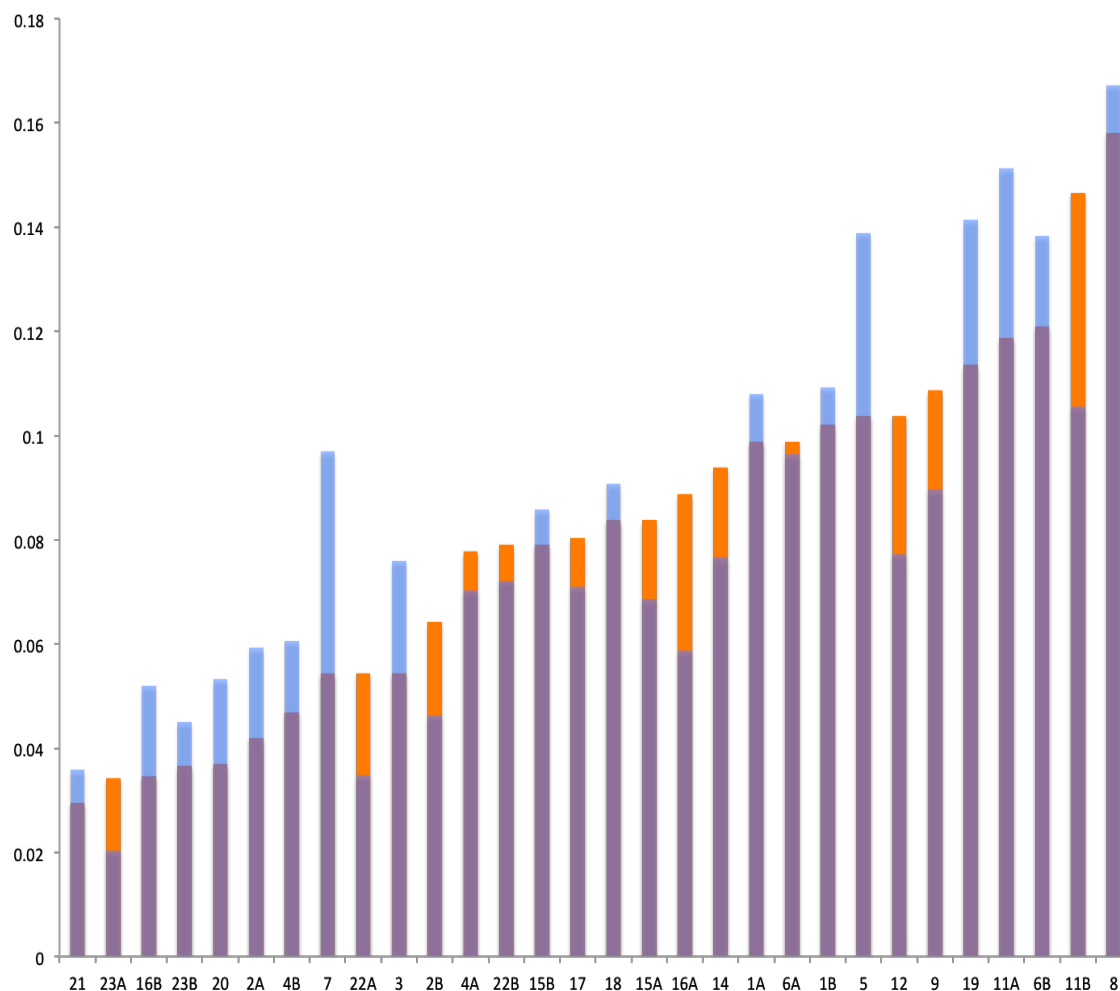


**Figure 34.** Overlay of bar graphs constructed from the magnitude of  $^1\text{H}$  chemical shift perturbation in HSQC data experienced by carbon-proton pairs of cholate (x-axis) as the concentration of cholate increased from 3 to 80 mM in the presence of 2.5 mM S-BNDHP (Orange) and R-BNDHP (Blue).

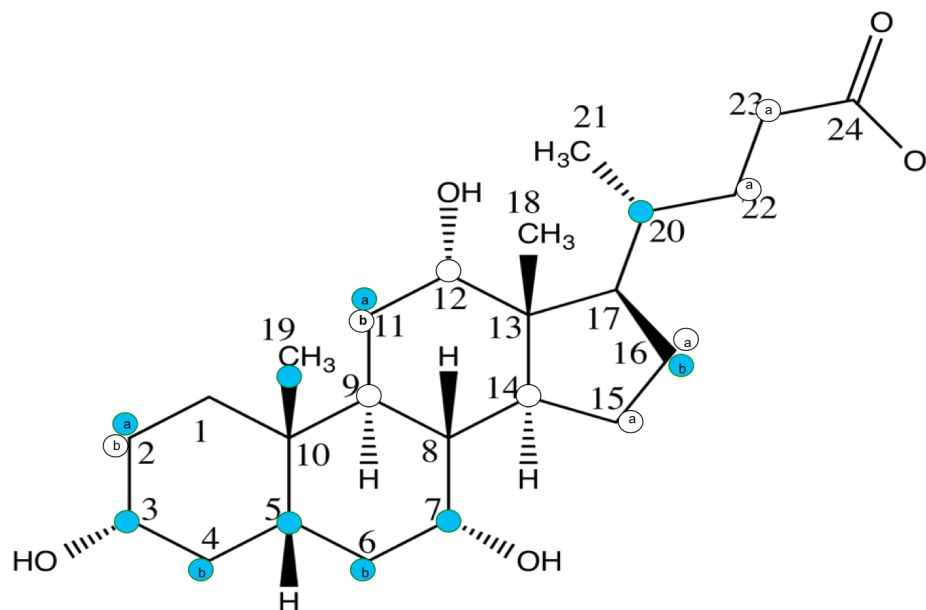


**Figure 35.** A molecule of cholate upon which circles have been placed on carbon-proton pairs that are either more strongly perturbed by R-BNDHP (filled circles) or more strongly perturbed by S-BNDHP (open circles). If no circle has been assigned, the difference between R- and S-BNDHP is negligible (less than 0.01).

The difference interaction mapping in Figure 35 shows that, generally, S-BNDHP more strongly perturbs the carbon-proton pairs on the C9-13 ring and on the C12 edge of cholate while R-BNDHP more strongly perturbs the carbon-proton pairs on the C1-5 and C6-10 rings and on the C7 edge of cholate. The strong perturbation of one side over the other for a particular atropisomer of

BNDHP suggests that S-BNDHP preferentially attacks the C12 edge of cholate, while R-BNDHP attacks the C7 edge, which is consistent with earlier NOE data.<sup>12</sup> The preferential attacking by different enantiomers of BNDHP could explain the chiral sensitivity observed in MEKC experiments performed previously in the lab.<sup>1</sup>

### 3.2.2 The “Net Change” Method for Analysis of HSQC Data

The “net change” method for the analysis of HSQC data determines the path-dependent magnitude of perturbation of a carbon-proton pair’s <sup>1</sup>H chemical shift during the process of bile salt aggregation. The “net change” method can be helpful in showing what kind of interactions are occurring at a specific carbon-proton pair between two different concentrations of cholate because the type of interaction will change the direction of the shift. The way the equations are set up, a hydrophobic interaction will cause a positive shift, while a hydrophilic interaction will cause a negative shift. The type of interaction can be determined by

$$X_1 = \delta_{3 \text{ mM}} - \delta_{11 \text{ mM}} , \quad (12)$$

$$X_2 = \delta_{11 \text{ mM}} - \delta_{20 \text{ mM}} , \quad (13)$$

$$X_3 = \delta_{20 \text{ mM}} - \delta_{30 \text{ mM}} , \quad (14)$$

$$X_4 = \delta_{30 \text{ mM}} - \delta_{80 \text{ mM}} , \quad (15)$$

where  $X_1$  is assumed to account for preliminary aggregation,  $X_2$  is considered to account for primary aggregation, and  $X_3$  and  $X_4$  are considered to account for secondary aggregation. The sum of  $X_{1-4}$  can also be used to determine the overall interaction for a particular carbon-proton pair. Figures 36-40 show the conserved  $^1\text{H}$  chemical shift for each carbon-proton pair of cholate with 2.5 mM R-BNDHP (gray), 2.5 mM S-BNDHP (black), and without a probe molecule (striped). Figure 36 shows the data from equation 12, Figure 37 shows the data from equation 13, Figure 38 shows the data from equation 14, Figure 39 shows the data from equation 15, and Figure 40 shows the sum of  $X_1$ ,  $X_2$ ,  $X_3$ , and  $X_4$ . Figures 36-40 are helpful for seeing which carbon-proton pairs are experiencing what kind of shifts over the course of aggregation and the dominant force for a given carbon-proton pair. The “total walk” method cannot do this because the math eliminates chemical shift perturbation directionality, which is necessary for determining the type of interaction.



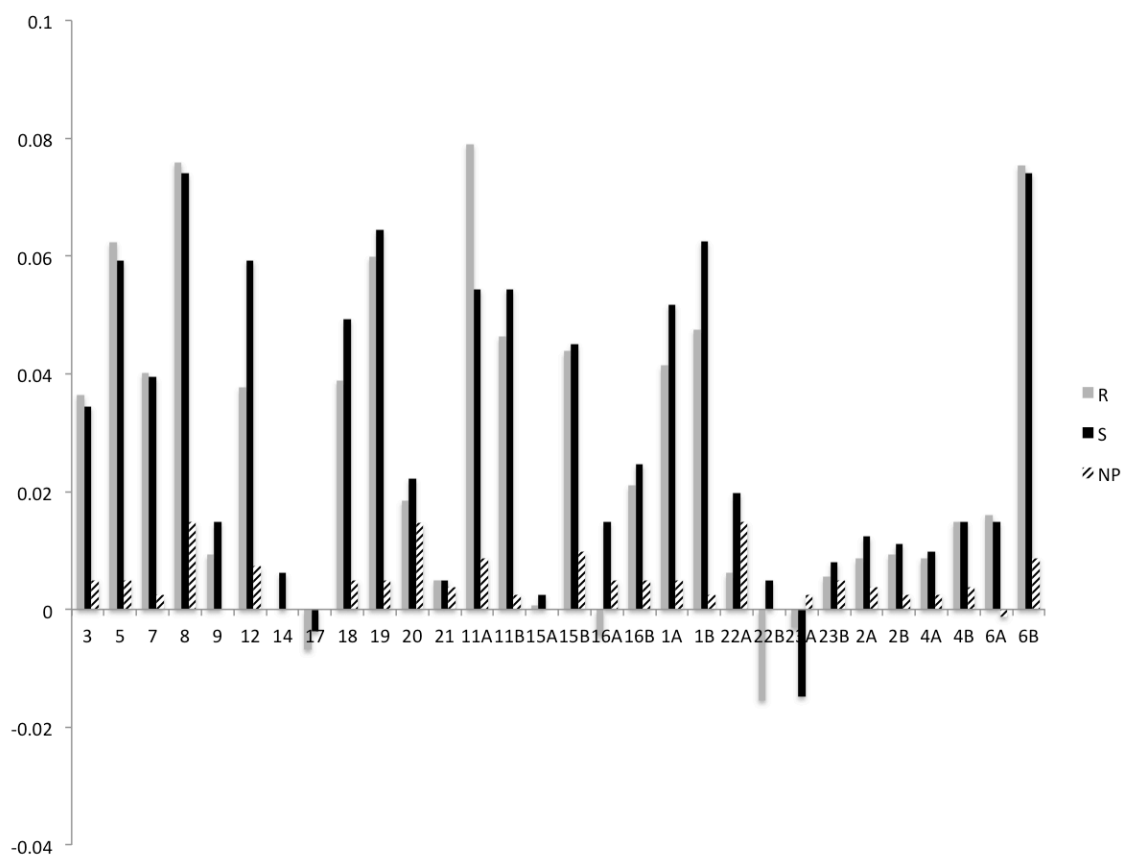


**Figure 36.** Bar graph illustrating magnitude and direction of <sup>1</sup>H chemical shift in HSQC data experienced by different carbon-proton pairs (x-axis) in the presence of 2.5 mM R-BNDHP (grey), 2.5 mM S-BNDHP (black), and without probe (striped) from 3 to 11 mM cholate. A positive bar signifies a hydrophobic shift. A negative bar signifies a hydrophilic shift.

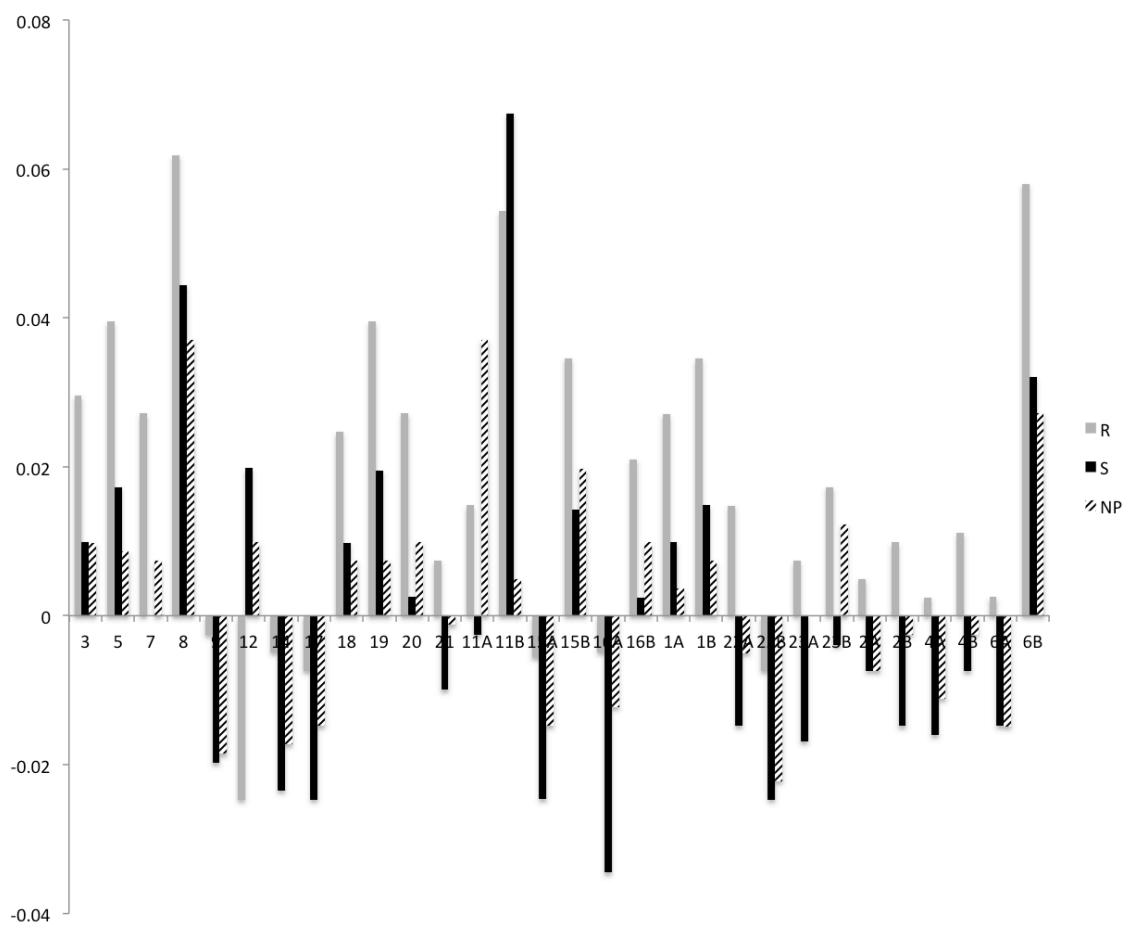


**Figure 37.** Bar graph illustrating magnitude and direction of <sup>1</sup>H chemical shift in HSQC data experienced by different carbon-proton pairs (x-axis) in the presence of 2.5 mM R-BNDHP (grey), 2.5 mM S-BNDHP (black), and without probe (striped) from 11 to 20 mM cholate. A positive bar signifies a hydrophobic shift. A negative bar signifies a hydrophilic shift.

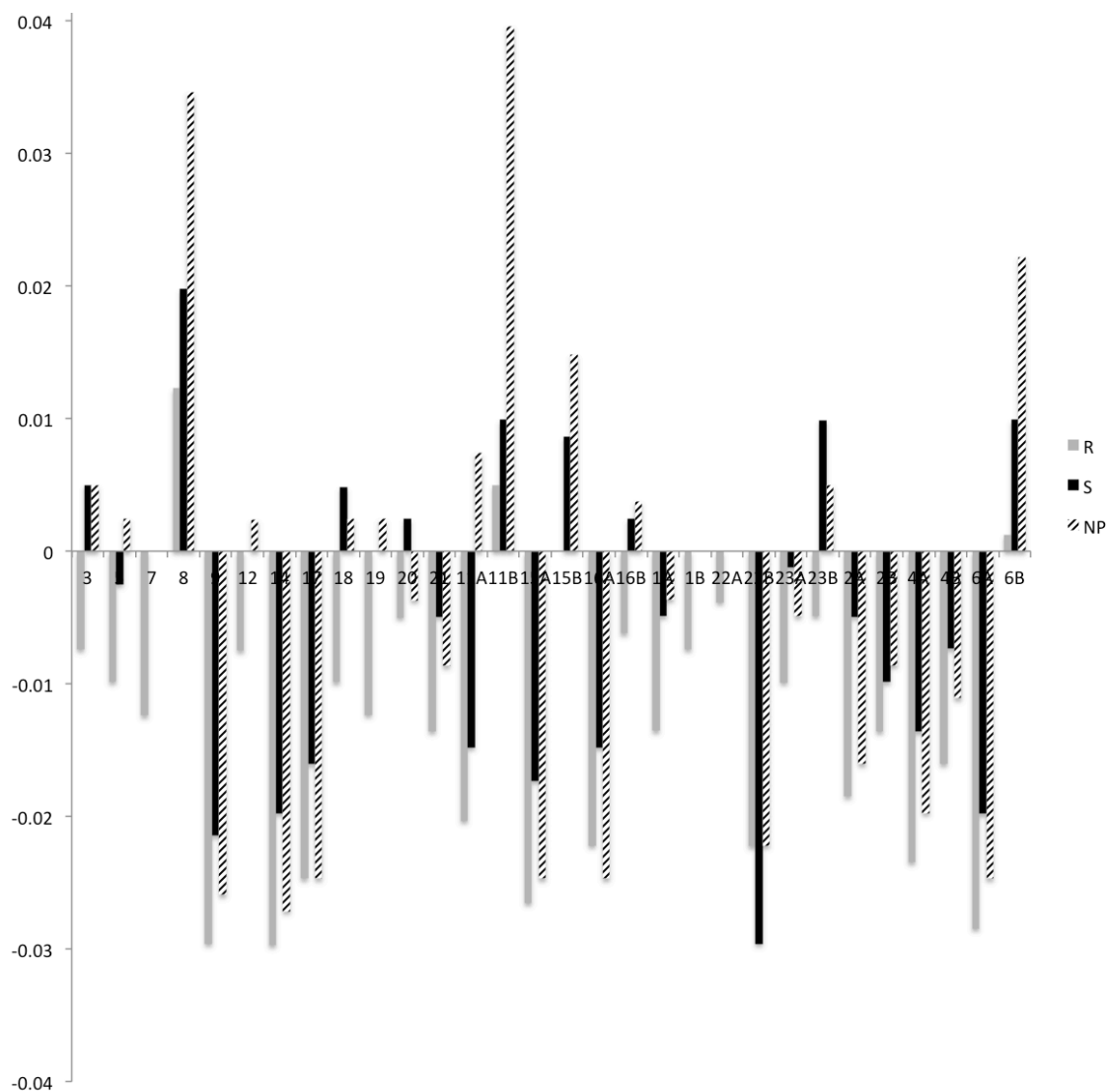


**Figure 38.** Bar graph illustrating magnitude and direction of <sup>1</sup>H chemical shift in HSQC data experienced by different carbon-proton pairs (x-axis) in the presence of 2.5 mM R-BNDHP (grey), 2.5 mM S-BNDHP (black), and without probe (striped) from 20 to 30 mM cholate. A positive bar signifies a hydrophobic shift. A negative bar signifies a hydrophilic shift.

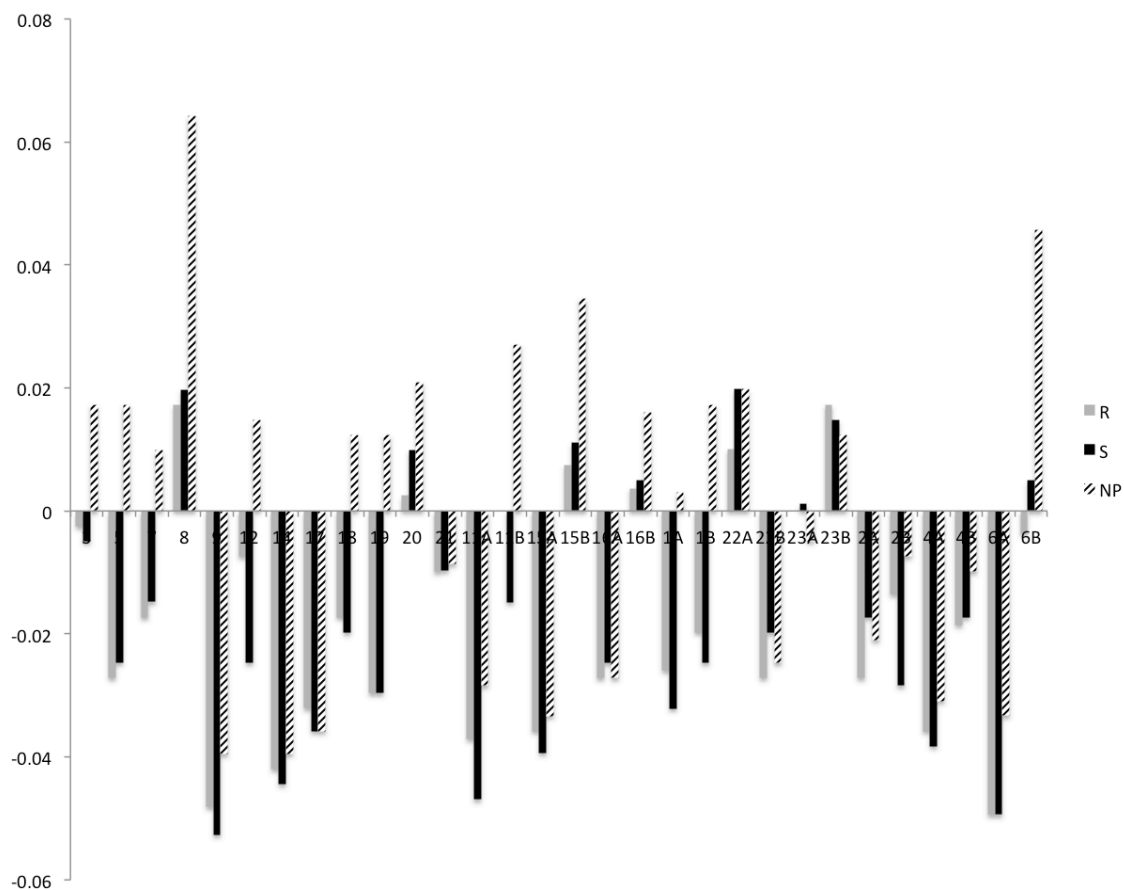


**Figure 39.** Bar graph illustrating magnitude and direction of <sup>1</sup>H chemical shift in HSQC data experienced by different carbon-proton pairs (x-axis) in the presence of 2.5 mM R-BNDHP (grey), 2.5 mM S-BNDHP (black), and without probe (striped) from 30 to 80 mM cholate. A positive bar signifies a hydrophobic shift. A negative bar signifies a hydrophilic shift.

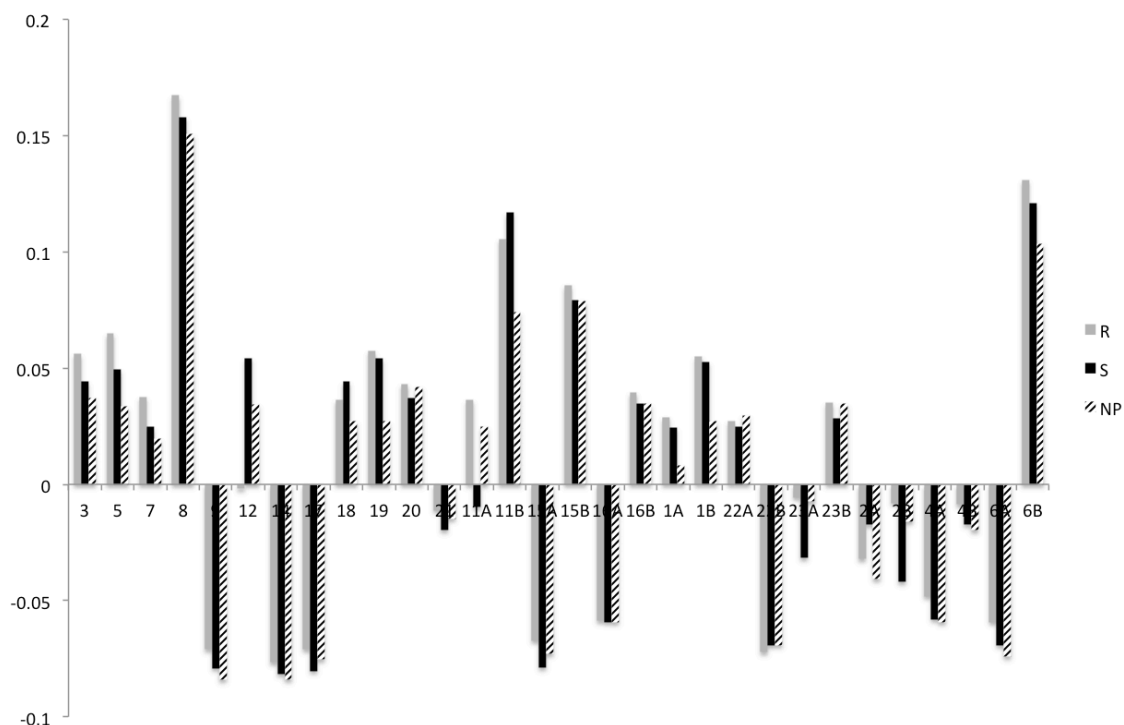


**Figure 40.** Bar graph illustrating magnitude and direction of  $^1\text{H}$  chemical shift in HSQC data experienced by different carbon-proton pairs (x-axis) in the presence of 2.5 mM R-BNDHP (grey), 2.5 mM S-BNDHP (black), and without probe (striped) from 3 to 80 mM cholate. A positive bar signifies a hydrophobic shift. A negative bar signifies a hydrophilic shift.

With the exception of C17 and C22B for R-BNDHP, and C23A for both R- and S-BNDHP, Figure 36 shows that every shift was a positive shift, or a hydrophobic shift. The hydrophobic shift is a result of dimer formation and probe binding. Figure 37 shows that many of the carbon-proton pairs on the solvent-exposed,

hydrophilic face are starting to show hydrophilic shifts. C9, C14, C17, and the “alpha” protons (pairs labeled C#A or #A) are located on the face that is exposed to the solvent, as opposed to the face in the binding pocket of a dimer. The hydrophilic shifts of the carbon-proton pairs on the hydrophilic face suggest that these pairs do not detect probe molecule binding past the dimer stage. Figure 37 also shows that C12 with R-BNDHP has a very negative chemical shift perturbation from 11 to 20 mM cholate, which would provide further evidence of the previously discussed edge attack. Evidence for secondary aggregation can be seen in Figure 38, which shows the system from 20 to 30 mM cholate. C8, C11B, and C6B exhibit very positive, hydrophobic shifts, providing further evidence of the skew. Because C8, C11B, and C6B are at the center of the skew, those carbon-proton pairs will remain in a very hydrophobic environment throughout aggregation. The majority of carbon-proton pairs have negligible shifts from 20 to 30 mM cholate, suggesting that much of cholate is neither perturbed by the probe molecule (which would result in hydrophobic shift), nor detecting the formation of a larger aggregate. C9, C14, C17, C15A, C16A, C2A, C4A, and C6A, making up most of the hydrophilic face of cholate, show a large hydrophilic shift from 20 to 30 mM cholate. The large hydrophilic shift could be an indication that these pairs are detecting the formation of a larger aggregate. According to Small’s model,<sup>20</sup> secondary aggregation will involve the formation of hydrogen bonds between alcohol groups on the hydrophilic faces of adjacent primary

micelles. Hydrogen bonding will create an increasingly hydrophilic environment compared to the hydrophobic environment created by the probe molecule. Figure 39 shows that the trends seen from 20 to 30 mM cholate continue from 30 to 80 mM, with the exception that more carbon-proton pairs are detecting the secondary aggregate, and have hydrophilic shifts as a result. Figure 40 shows that the hydrophobic and hydrophilic interactions as the concentration of cholate increases from 3 to 80 mM partly cancel each other out. Generally, carbon-proton pairs on the hydrophobic side of cholate experience a more hydrophobic environment, with C8, C11B, and C6B exhibiting the most hydrophobic environment. Conversely, the hydrophilic side of cholate, most notably C9, C14, and C17, experiences more hydrophilic environments. The evidence from the conserved method suggests that secondary aggregates do indeed form through the hydrogen bonding of hydrophilic faces on neighboring primary aggregates, an observation that supports Small's model and has not been previously supported by experimental data in literature.

### 3.3 Aggregation Number Determination of the Cholates Micelle System as Determined by Mass Spectrometry

The aggregation number (AN) of a micelle system describes the number of monomer units that comprise a micelle. According to Small's model,<sup>20</sup> the aggregation number of the bile salt micelle system varies; the primary aggregate has an AN = 2-10, while the secondary aggregate has an AN = 12-100. Mass spectrometry provides a useful tool in aggregation number determination, as both  $m/z$  and isotopic profile will change in predictable ways as the number of carbons being analyzed increases. The isotopic profile for the case of the cholates system is dominated by the natural abundance of  $^{13}\text{C}$ , which is 1.08%. While only the molecular ion peak will contain all  $^{12}\text{C}$  atoms, there could be several peaks of varying intensity with a number of  $^{13}\text{C}$  atoms dependent upon the number of carbons in the system. For example, in a molecule containing 100 carbon atoms the probability that the molecule will contain one  $^{13}\text{C}$  is 10.8% and two  $^{13}\text{C}$  is about 60%. Explicitly, the relative intensity ( $RI$ ) of a molecule containing  $J$   $^{13}\text{C}$  to the zero  $^{13}\text{C}$ -containing molecule is

$$RI = (0.0108)^J * \frac{n!}{J!(n-J)!}, \quad (16)$$

where  $n$  is the number of carbons in the molecule.

The isotopic ratio is not the only tool necessary to characterize every  $m/z$  signal on the mass spectrum. Because electrospray ionization (ESI) can deposit



several charges onto an analyte before mass analysis is performed, it is likely to observe in the mass spectrum a singly charged dimer, a doubly charged tetramer, and a triply charged hexamer that have the same  $m/z$ . Thankfully, there will be differences in the spacing of the isotope peaks; whereas the dimer will exhibit spacing between isotope peaks with  $m/z$  equal to one mass unit, the tetramer will have spacing of  $m/z$  equal to half a mass unit, and the hexamer will have spacing of  $m/z$  equal to a third of a mass unit. By knowing the isotopic profile of a given aggregate and the spacing between isotope peaks, full characterization of the mass spectrum is possible.

Mass spectra from approximately 5  $\mu\text{L}$  of 1, 3, 5, 7, 9, 11, 13, 15, 20, 30, 40, 70, 80, and 100 mM sodium cholate solutions at a pH of approximately 7.5 were collected. The complete mass spectrum of sodium cholate (Figure 41) and aggregates forming cholate micelles (Figures 42-48) were observed. Only the 70 mM sample's spectrum is presented in this thesis because the collected spectra from the other concentrations showed the presence of the same peaks with only a slight variance in the intensity of those peaks relative to the base cholate peak. While all identified aggregates appear in the spectrum of each concentration, the relative intensity of the largest peak of an aggregate compared to the intensity of the base peak for that concentration, typically, increases as concentration increases. The standard deviation of the average relative intensity of every concentration for each aggregate is small.

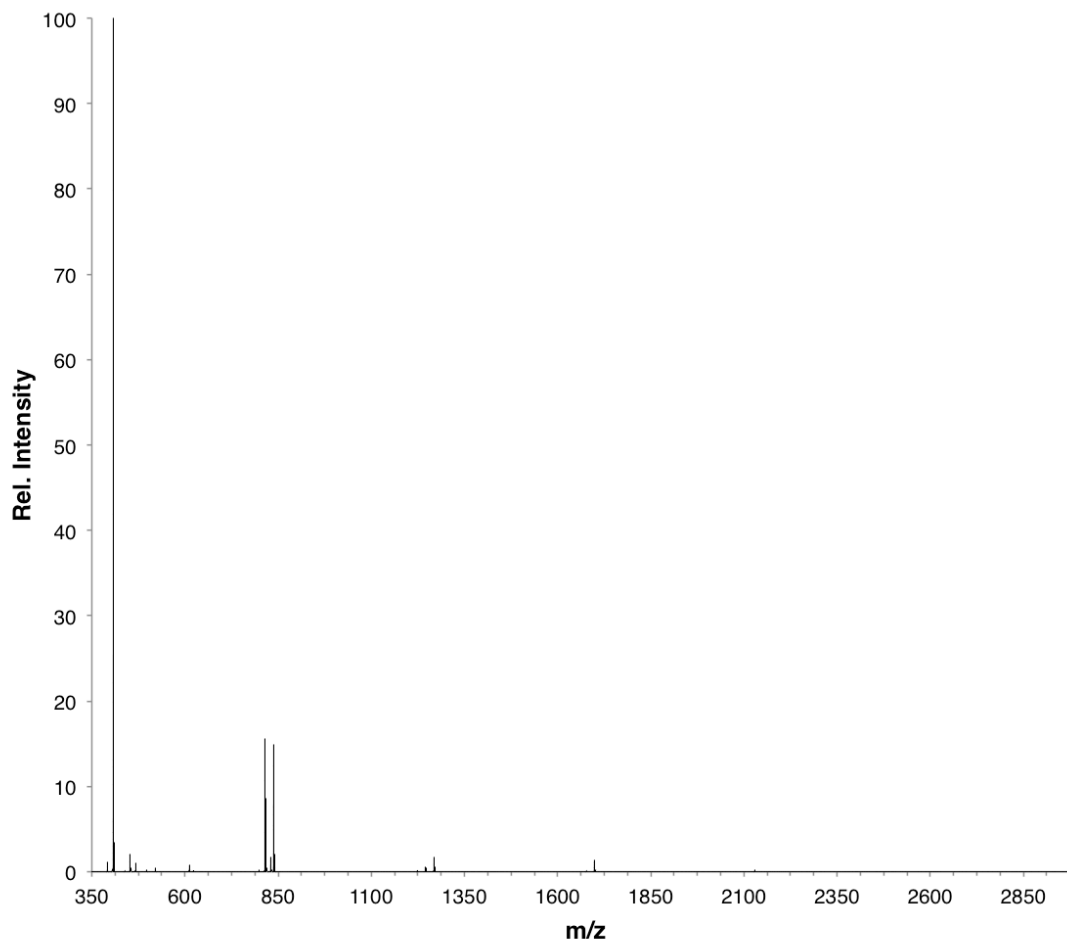


**Figure 41.** Negative ion mass spectrum collected from a 70 mM sodium cholate sample at pH = 7.5 using ESI and orbitrap by injecting sample into a stream of 90:10 water to methanol at a flow rate of 30  $\mu\text{L}/\text{min}$ . The relative intensity is set relative to the base peak at  $m/z = 407.2806$ , which has been identified as  $\text{C}_{24}\text{H}_{39}\text{O}_5^-$ , the molecular ion of deprotonated cholic acid. Higher mass-to-charge aggregates are also observed.

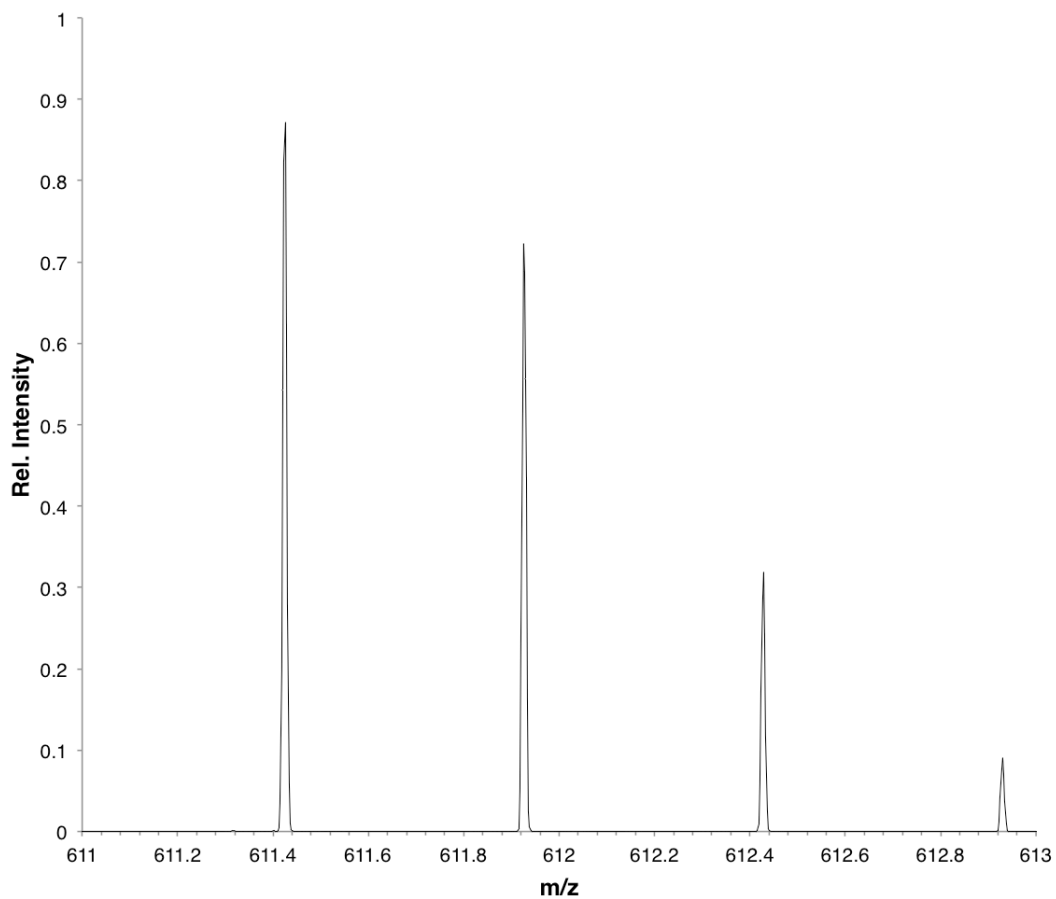


**Figure 42.** A portion of the negative ion mass spectrum collected from a 70 mM sodium cholate sample at pH = 7.5 using ESI and orbitrap by injecting sample into a stream of 90:10 water to methanol at a flow rate of 30  $\mu\text{L}/\text{min}$ . The relative intensity is set relative to the base peak at  $m/z = 407.2806$ , which has been identified as  $\text{C}_{24}\text{H}_{39}\text{O}_5^-$ , the molecular ion of deprotonated cholic acid. The signal from a doubly charged trimer can be seen here, beginning at  $m/z = 611.4248$ .

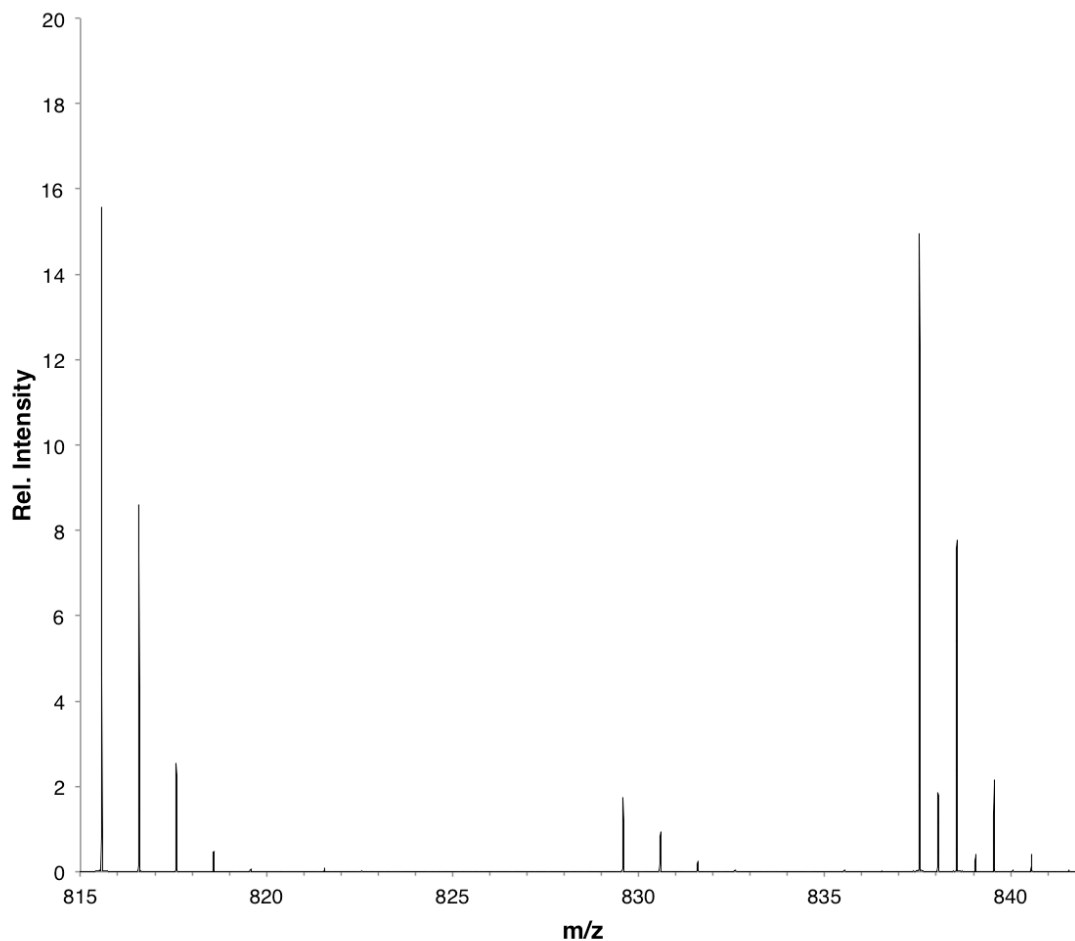


**Figure 43.** A portion of the negative ion mass spectrum collected from a 70 mM sodium cholate sample at pH = 7.5 using ESI and orbitrap by injecting sample into a stream of 90:10 water to methanol at a flow rate of 30  $\mu\text{L}/\text{min}$ . The relative intensity is set relative to the base peak at  $m/z = 407.2806$ , which has been identified as  $\text{C}_{24}\text{H}_{39}\text{O}_5^-$ , the molecular ion of deprotonated cholic acid. The signals at  $m/z = 815.5694$  and  $837.5508$  originate from dimers. Another signal at  $m/z = 837.5508$  is a doubly charged tetramer.

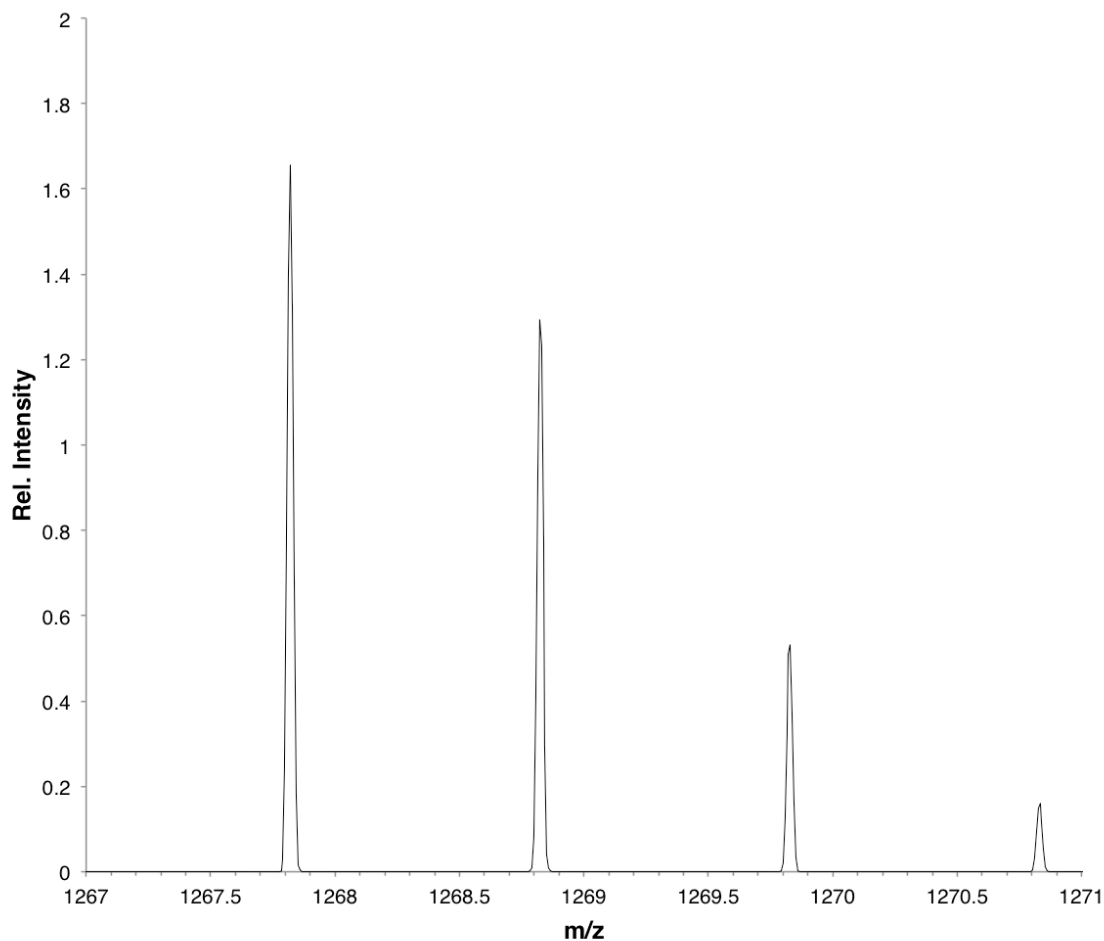


**Figure 44.** A portion of the negative ion mass spectrum collected from a 70 mM sodium cholate sample at pH = 7.5 using ESI and orbitrap by injecting sample into a stream of 90:10 water to methanol at a flow rate of 30  $\mu\text{L}/\text{min}$ . The relative intensity is set relative to the base peak at  $m/z = 407.2806$ , which has been identified as  $\text{C}_{24}\text{H}_{39}\text{O}_5^-$ , the molecular ion of deprotonated cholic acid. The signal from one unique aggregate, a trimer, can be seen here, beginning at  $m/z = 1267.8205$ .

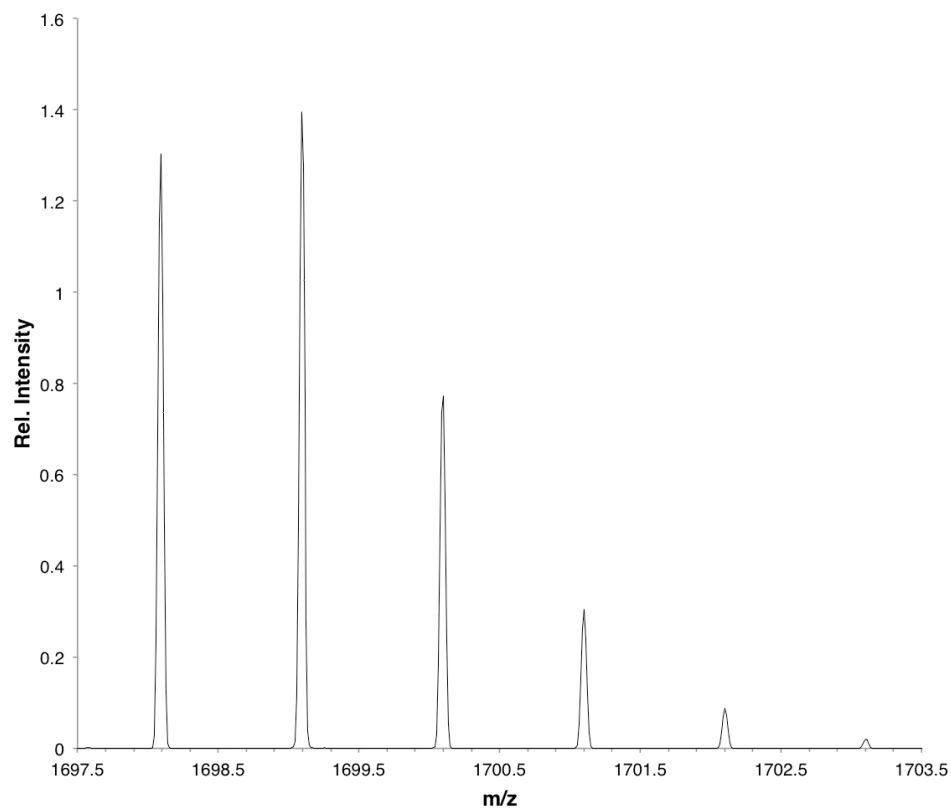


**Figure 45.** A portion of the negative ion mass spectrum collected from a 70 mM sodium cholate sample at pH = 7.5 using ESI and orbitrap by injecting sample into a stream of 90:10 water to methanol at a flow rate of 30  $\mu\text{L}/\text{min}$ . The relative intensity is set relative to the base peak at  $m/z = 407.2806$ , which has been identified as  $\text{C}_{24}\text{H}_{39}\text{O}_5^-$ , the molecular ion of deprotonated cholic acid. The signal from one unique aggregate, a tetramer, can be seen here, beginning at  $m/z = 1698.0910$ .

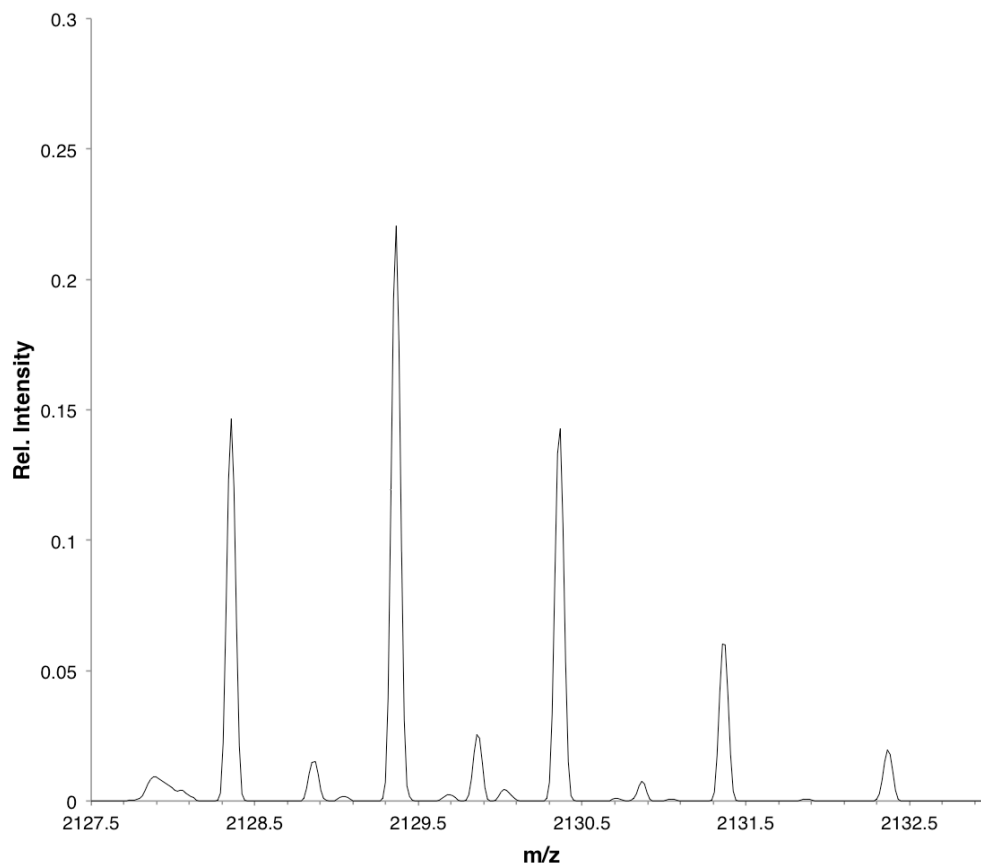


**Figure 46.** A portion of the negative ion mass spectrum collected from a 70 mM sodium cholate sample at pH = 7.5 using ESI and orbitrap by injecting sample into a stream of 90:10 water to methanol at a flow rate of 30  $\mu\text{L}/\text{min}$ . The relative intensity is set relative to the base peak at  $m/z = 407.2806$ , which has been identified as  $\text{C}_{24}\text{H}_{39}\text{O}_5^-$ , the molecular ion of deprotonated cholic acid. Signals from two unique aggregates, a 5- and 10-mer, can be seen, both beginning at  $m/z = 2128.3567$ .

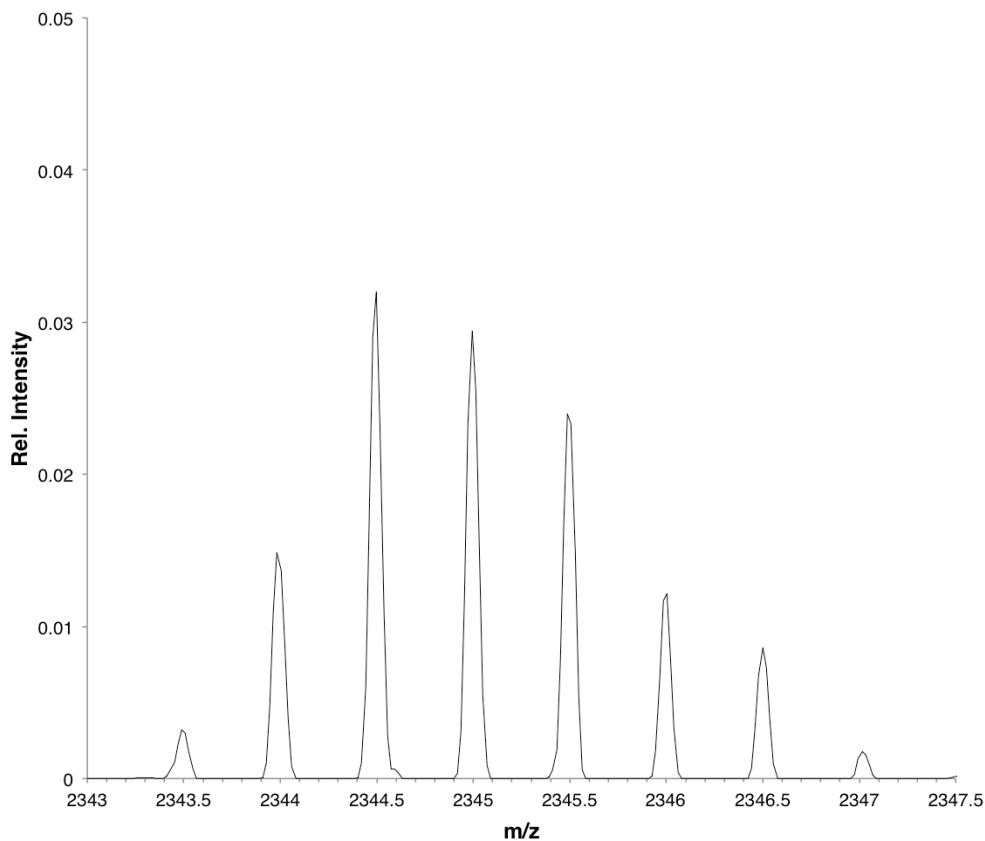


**Figure 47.** A portion of the negative ion mass spectrum collected from a 70 mM sodium cholate sample at pH = 7.5 using ESI and orbitrap by injecting sample into a stream of 90:10 water to methanol at a flow rate of 30  $\mu\text{L}/\text{min}$ . The relative intensity is set relative to the base peak at  $m/z = 407.2806$ , which has been identified as  $\text{C}_{24}\text{H}_{39}\text{O}_5^-$ , the molecular ion of deprotonated cholic acid. The signal from one unique aggregate, an 11-mer, can be seen here, beginning at  $m/z = 2343.4948$ .



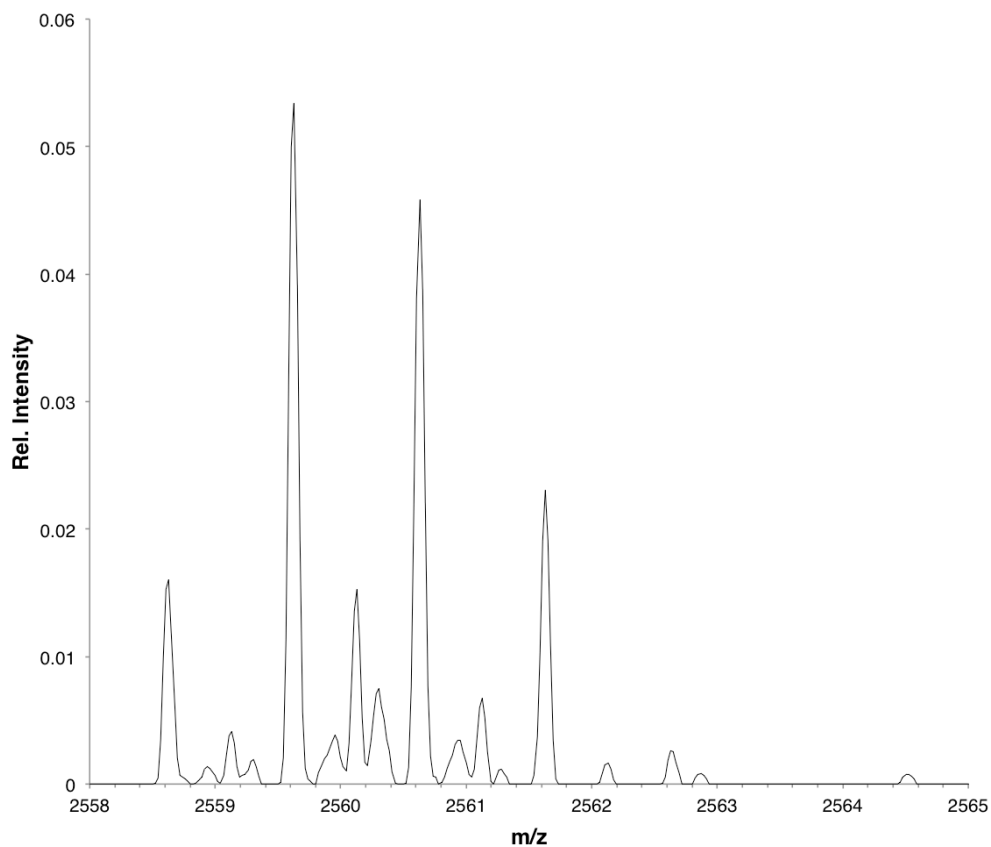


**Figure 48.** A portion of the negative ion mass spectrum collected from a 70 mM sodium cholate sample at pH = 7.5 using ESI and orbitrap by injecting sample into a stream of 90:10 water to methanol at a flow rate of 30  $\mu\text{L}/\text{min}$ . The relative intensity is set relative to the base peak at  $m/z = 407.2806$ , which has been identified as  $\text{C}_{24}\text{H}_{39}\text{O}_5^-$ , the molecular ion of deprotonated cholic acid. Signals from three unique aggregates, a hexa-, 12-, and 18-mer, can be seen, all beginning at  $m/z = 2558.6230$ .

As a result of the exceptional resolving power of the orbitrap mass analyzer, the isotopic profile of each aggregate matched its predicted profile. From the isotopic profiles and from the spacing of the isotope peaks it was determined that thirteen unique aggregates were observed (Table 5).

**Table 5. Cholates Aggregates Observed by Mass Spectrometry**

m/z	Formula	Aggregation Number	Charge	Exact Mass (amu)	Deviation (ppm)
407.2806	C <sub>24</sub> H <sub>39</sub> O <sub>5</sub>	1	-1	407.27975	2.0
611.4248	C <sub>72</sub> H <sub>118</sub> O <sub>15</sub>	3	-2	1222.84707	2.0
815.5694	C <sub>48</sub> H <sub>79</sub> O <sub>10</sub>	2	-1	815.56732	3.0
837.5508	C <sub>48</sub> H <sub>78</sub> O <sub>10</sub> Na	2	-1	837.54927	2.0
	C <sub>96</sub> H <sub>156</sub> O <sub>20</sub> Na <sub>2</sub>	4	-2	1675.09854	2.0
1267.8205	C <sub>72</sub> H <sub>117</sub> O <sub>15</sub> Na <sub>2</sub>	3	-1	1267.81879	1.0
1698.0910	C <sub>96</sub> H <sub>156</sub> O <sub>20</sub> Na <sub>3</sub>	4	-1	1698.08831	2.0
2128.3567	C <sub>120</sub> H <sub>195</sub> O <sub>25</sub> Na <sub>4</sub>	5	-1	2128.35782	1.0
	C <sub>240</sub> H <sub>390</sub> O <sub>50</sub> Na <sub>8</sub>	10	-2	4256.71564	1.0
2343.4948	C <sub>264</sub> H <sub>429</sub> O <sub>55</sub> Na <sub>9</sub>	11	-2	4686.98517	1.0
2558.6230	C <sub>144</sub> H <sub>234</sub> O <sub>30</sub> Na <sub>5</sub>	6	-1	2558.62734	2.0
	C <sub>288</sub> H <sub>468</sub> O <sub>60</sub> Na <sub>10</sub>	12	-2	5117.25468	2.0
	C <sub>432</sub> H <sub>702</sub> O <sub>90</sub> Na <sub>15</sub>	18	-3	7675.88202	2.0

The results from mass spectroscopy are noteworthy in that they differ from both published results of cholates mass spectrometry as well as Small's model for micelle aggregation.<sup>27</sup> While Rodriguez and Yost were only able to detect micelles with a maximum aggregation number of 17, an aggregate with an

aggregation number of 18 was seen here. A potential explanation for the expanded results could be a result of the resolving power of orbitrap. Rodriguez and Yost used an LCQ ion-trap mass analyzer, which may not have had the resolving power to be able to resolve the peaks of the AN = 6 aggregate from the AN = 18 aggregate. In ESI, because an analyte can assume many different charge states, it is important to have a mass analyzer with high resolving power. Another potential reason for the differences is that Rodriguez and Yost injected in positive ion mode using different ionic conditions. The ionic strength of the solution can alter the stability of the aggregates as well as the CMCs of the aggregates in solution.

The mass spectrometry results are also not fully supported by Small's model, which does not account for fragments with an odd aggregation number for the primary micelle. According to Small's model, primary aggregates are formed through hydrophobic attraction by the binding pocket comprised of one or more dimers. Therefore, an aggregate with an aggregation number of three does not fit Small's model, suggesting that a revised model may be needed to fully explain the complex bile salt micelle system.

One final observation that can be made from the MS data presented here is that the abundance of the large aggregates is largely unaffected by the concentration of the solution at injection. According to the CMCs and Small's model,<sup>27</sup> aggregates larger than an aggregation number of ten should not be

observed in a spectrum of a cholate solution less concentrated than 11 mM. The large aggregates, however, are observed at injected concentrations of sodium cholate as low as 1 mM, much less concentrated than even the CMC for the primary aggregate. A plausible reason for the apparent contradiction arises from the phenomena that make ESI possible. The observed large aggregates on the mass spectra of solutions of insufficient concentration to normally form these aggregates suggests that the cholate molecules can arrange themselves into micelles as evaporation occurs through the electrospray ionization process. Therefore, the effective concentration of the solution that actually gets analyzed in the mass spectrometer could be many times more concentrated than the initial solution.

#### 4. Conclusion

While bile salts play an important role in the digestive systems of mammals, the mechanism behind bile salt aggregation and the characteristics of bile salt aggregates remain sufficiently complex to elude full understanding. According to literature,<sup>1, 26, 53-60</sup> several variables, including pH of the solution and ionic strength, affect the critical micelle concentration of bile salt surfactant systems. While the critical micelle concentration of the bile salt surfactant system can be determined with proton NMR data by modeling the chemical shift perturbations of a probe molecule, PCA on this data shows promise of yielding more accurate, less biased CMCs. Heteronuclear single quantum coherence spectroscopy provides a technique to examine bile salt micellar structure, through probing the intra- and inter-micellar interactions. Through HSQC data, a skew between two monomers composing a dimer is evident. HSQC also provided potential insight into the chiral selectivity of certain bile salts, which was first noted in MEKC data, as well as insight into the hydrophilic interactions that occur during the formation of secondary micelles. Finally, orbitrap mass spectrometry of cholates solutions enabled the observation of larger aggregates than had previously been reported for cholates micelles. As none of the published models for bile salt aggregation support all of the evidence published here, the need for a new, more broadly encompassing model of bile salt aggregation is evident.

## References

1. Hebling, C. M.; Thompson, L. E.; Eckenroad, K. W.; Manley, G. A.; Fry, R. A.; Mueller, K. T.; Strein, T. G.; Rovnyak, D. *Langmuir* **2008**, 24, 13866-13874.
2. Hinze, W. L.; Williams, R. W., Jr.; Fu, Z.; Suzuki, Y.; Quina, F. H. *Colloids Surf.* **1990**, 48, 1-3, 79-94.
3. Ijare, O. B.; Somashekar, B. S.; Jadegoud, Y.; Nagana Gowda, G. A. *Lipids* **2005**, 40, 10, 1031-1040.
4. Wenzel, T. J.; Cameron, K. *Magn. Reson. Chem.* **1989**, 27, 8, 734-739.
5. Bernstein, H. J.; Pople, J. A.; Schneider, W. G. *Can. J. Chem.* **1957**, 35, 65-81.
6. Caldarelli, S.; Catalano, D.; Di Bari, L.; Pasquali, M.; Veracini, C. A.; Leoni, P. *Gazz. Chim. Ital.* **1990**, 120, 3, 211-213.
7. Cruz, J. R.; Becker, B. A.; Morris, K. F.; Larive, C. K. *Magn. Reson. Chem.* **2008**, 46, 838-845.
8. Friebolin, H. *Basic One- and Two-Dimensional NMR Spectroscopy*. Verlagsgesellschaft: Weinheim; **1993**.
9. Orfi, L.; Lin, M.; Larive, C. K. *Anal. Chem.* **1998**, 70, 1339-1345.
10. Söderman, O.; Stilbs, P.; Price, W. S. *Concepts in Magn. Reson. A* **2004**, 23A, 2, 121-135.

11. Morris, K. F.; Froberg, A. L.; Becker, B. A.; Almeida, V. K.; Tarus, J.; Larive, C. K. *Anal. Chem.* **2005**, 254-263.
12. Eckenroad, K. W.; Thompson, L. E.; Strein, T. G.; Rovnyak, D. *Magn. Reson. Chem.* **2007**, 45, 72-75.
13. Hu, Q.; Noll, R. J.; Li, H.; Makarov, A.; Hardman, M.; Cooks, R. G. *J. Mass Spectrom.* **2005**, 40, 430-443.
14. Rodriguez, M. A.; Yost, R. A. *Rapid Commun. Mass Spectrom.* **2000**, 14, 1398-1403.
15. Ikegawa, S.; Okuyama, H.; Oohashi, J.; Murao, N.; Goto, J. *Anal. Sci.* **1999**, 15, 625-631.
16. Nohara, D.; Kajiura, T.; Takeda, K. *J. Mass Spectrom.* **2005**, 40, 489-493.
17. Mukhopadhyay, S.; Maitra, U. *Curr. Sci.* **2004**, 87, 1666-1683.
18. Haslewood, G. A. D. *Bile Salts*; Methuen & Co Ltd: London, **1967**.
19. Danielsson, H.; Sjövall, J. *Sterols and Bile Acids*; Elsevier: Amsterdam, **1985**.
20. Small, D. M. *Adv. Chem. Ser.* **1968**, 31-52.
21. Kawamura, H.; Murata, Y.; Yamaguchi, T.; Igimi, H.; Tanaka, M.; Sugihara, G.; Kratochvil, J. P. *J. Phys. Chem.* **1989**, 93, 3321-3326.
22. Giglio, E.; Loreti, S.; Pavel, N. V. *J. Phys. Chem.* **1988**, 92, 2858-2862.

23. Ouimet, C. M. Honors' Thesis, *Understanding Bile Micelle Chiral Interactions*, Bucknell University, **2014**.
24. Warren, D. B.; Chalmers, D. K.; Hutchinson, K.; Dang, W.; Pouton, C. W. *Colloids Surf., A* **2006**, 280, 182-193.
25. Bielejewska, A.; Duszczyk, K.; Kwaterczak, A.; Sybilska, D. *J. Chromatogr., A* **2002**, 977, 2, 225-237.
26. Gouin, S.; Zhu, X. X. *Langmuir* **1998**, 4025-4029.
27. Paul, P. H.; Garguilo, M. G.; Rakestraw, D. J. *Anal. Chem.* **1998**, 70, 2459-2467.
28. Chankvetadze, B.; Endresz, G.; Schulte, G.; Bergenthal, D.; Blaschke, G. *J. Chromatogr., A* **1996**, 732, 143-150.
29. Rugutt, J. K.; Billiot, E.; Warner, I. M.; *Langmuir* **2000**, 16, 3022-3029.
30. Yarabe, H. H.; Rugutt, J. K.; McCarroll, M. E.; Warner, I. M.; *Electrophoresis* **2000**, 21, 2025-2032.
31. Valle, B. C.; Morris, K. F.; Fletcher, K. A.; Fernand, V.; Sword, D. M.; Eldridge, S.; Larive, C. K.; Warner, I. M. *Langmuir* **2007**, 23, 425-435.
32. Morris, K. F.; Becker, B. A.; Valle, B. C.; Warner, I. M.; Larive, C. K. *J. Phys. Chem. B* **2006**, 110, 17359-17369.
33. Yamamoto, C.; Yashima, E.; Okamoto, Y. *J. Am. Chem. Soc.* **2002**, 124, 12583-12589.



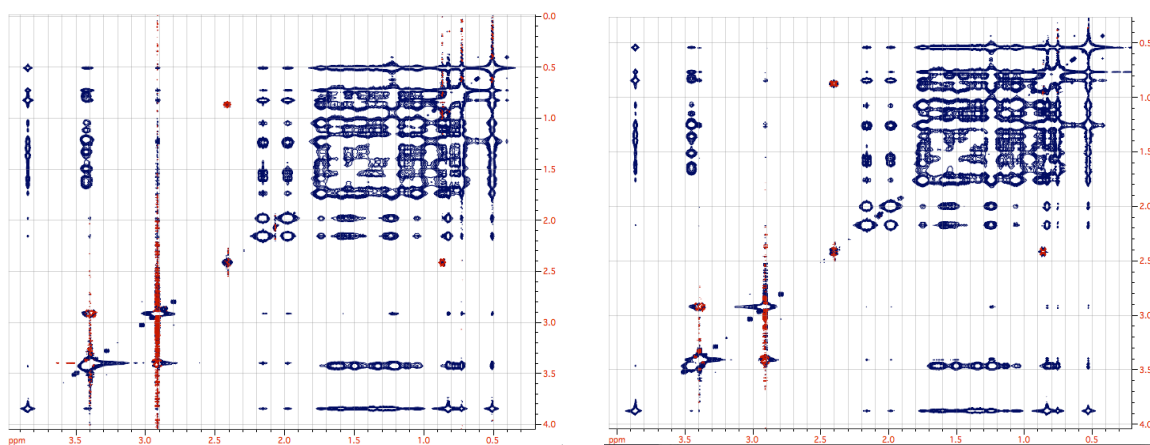
34. Cavanagh, J.; Fairbrother, W. J.; Palmer III, A. G.; Skelton, N. J.; Rance, M. *Protein NMR Spectroscopy Principles and Practice*; Academic Press: New York, 1996.
35. Kawamura, H.; Manabe, M.; Narikiyo, T.; Igimi, H.; Murata, Y.; Sugihara, G.; Tanaka, M. *J. Sol. Chem.* **1987**, 16, 433-441.
36. Leyden, D. E.; Cox, R. H. *Analytical Applications of NMR*; John Wiley & Sons: New York, 1977.
37. MacComber, R. S. *A Complete Introduction to Modern NMR Spectroscopy*; John Wiley & Sons: Toronto, 1998.
38. Pauli, W. *Naturwissenschaften* **1924**, 12, 741.
39. Gerlach, W.; Stern, O. *Z. Phys.* **1921**, 8, 110-111.
40. Stern, O. *Z. Phys.* **1921**, 7, 249.
41. Gerlach, W.; Stern, O. *Ann. Phys. Lpz.* **1924**, 74, 673.
42. Lazarev, B. G.; Shubnikov, L. W. *Phys. Z. Sowjet.* **1937**, 11, 445.
43. Rabi, I. I.; Millman, S.; Kusch, P.; Zacharias, J. R. *Phys. Rev.* **1939**, 55, 526-535.
44. Purcell, E. M.; Torrey, H. C.; Pound, R. V. *Phys. Rev.* **1946**, 69, 37-38.
45. Bloch, R.; Hansen, W. W.; Packard, M. E. *Phys. Rev.* **1946**, 69, 474-485.
46. Halliday, J. D.; Hill, H. D. W.; Richard, R. E. *J. Phys. E* **1969**, 2, 2, 29-32.
47. Ernst, R. R.; Anderson, W. A. *Rev. Sci. Instrum.* **1966**, 37, 93-102.

48. Sanders, J.; Hunter, B. K. *Modern NMR Spectroscopy: A Guide for Chemists*, 2nd ed.; Oxford University Press: Oxford, 1993.
49. Bodenhausen, G.; Ruben, D. J. *Chem. Phys. Lett.* **1980**, 69, 1, 185-189.
50. Bodenhausen, G.; Freeman, R. *J. Magn. Reson.* **1977**, 28, 3, 471-476.
51. Morris, G. A.; Freeman, R. *J. Am. Chem. Soc.* **1979**, 101, 3, 760-762.
52. Hilton, M.; Armstrong, D. W. *J. Liq. Chromatogr.* **1991**, 14, 1, 9-28.
53. Kratochvil, J. P.; Sugihara, G.; Misturu, T.; Igimi, H.; Yamaguchi, T.; Murata, Y.; Kawamura, H. *J. Phys. Chem.* **1989**, 93, 3321-3326.
54. Nakashima, T.; Anno, T.; Kanda, H.; Sato, Y.; Kuroi, H.; Fujji, S.; Nagadome, G.; Sigihara, G. *Colloids Surf.* **2002**, 24, 103-110.
55. Carey, M. C.; Montet, J.; Small, D. M. *Biochemistry* **1975**, 14, 22, 4896-4905.
56. Subuddhi, U.; Mishra, A. K. *Colloids Surf., B* **2007**, 57, 102-107.
57. Roda, A.; Hofmann, A. F.; Mysels, K. J. *J. Biol. Chem.* **1983**, 25, 6362-6370.
58. Nakamura, H.; Sano, A.; Marsuura, K.; *Anal. Sci.* **1998**, 14, 379-382.
59. Maeder, C.; Beaudoin, G. M. J., III; Hsu, E.; Escobar, V. A.; Chambers, S. M.; Kurtin, W. E.; Bushey, M. M. *Electrophoresis* **2000**, 21, 706-714.
60. Sugihara, G.; Yamakawa, K.; Murata, Y.; Tanaka, M. *J. Phys. Chem.* **1982**, 86, 14, 2784-2788.
61. Balducci, R.; Roda, A.; Pearlman, R. S. *J. Solution Chem.* **1989**, 18, 4, 355-368.

62. Schönbeck, C.; Westh, P.; Madsen, J. C.; Larsen, K. L.; Ståde, L. W.; Holm, R. *Langmuir* **2010**, 26, 23, 17949-17957.
63. Holm, R.; Shi, W.; Hartvig, R. A.; Askjær, S.; Madsen, J. C.; Westh, P. *Phys. Chem. Chem. Phys.* **2009**, 11, 5070-5078.
64. Dominguez, C.; Sebban-Kreuzer, C.; Bornet, O; Kerfelec, B.; Chapus, C.; Guerlesquin, F. *FEBS Lett.* **2000**, 482, 1-2, 109-112.
65. Wein, W. *Ann. Phys Leipzig* **1898**, 301, 1-18.
66. Thomson, J. J. *Proc. R. Soc. London, A* **1913**, 89, 1-20.
67. Aston, F. W. *Philos. Mag.* **1919**, 38, 707-715.
68. Zhu, G.; Sun, L.; Yan, X.; Dovichi, N. J. *Anal. Chem.* **2014**, 86, 13, 6331-6336.
69. Ho, C. S.; Lam, C. W. K.; Chan, M. H. M.; Cheung, R. C. K.; Law, L. K.; Lit, L. C. W.; Ng, K. F.; Suen, M. W. M.; Tai, H. L. *Clin. Biochem. Rev.* **2003**, 24, 1, 3-12.
70. Dole, M.; Mach, L. L.; Hines, R. L.; Mobley, R. C.; Ferguson, L. P.; Alice, M. B. *J. Chem. Phys.* **1968**, 49, 2240.
71. Mach, L. L.; Kralik, P.; Rheude, A.; Dole, M. *J. Chem. Phys.* **1970**, 52, 4977.
72. Fenn, J. B. *J. Am. Soc. Mass Spectrom.* **1993**, 4, 524-535.
73. Perry, R. H.; Cooks, R. G.; Noll, R. J. *Mass Spectrom. Rev.* **2008**, 27, 6, 661-699.
74. Scigelova, M.; Makarov, A. *Proteomics* **2006**, 6, 2, 16-21.

75. Makarov, A.; Scigelova, M. *J. Chromatogr., A* **2010**, 1217, 25, 3938-3945.
76. Makarov, A. *Anal. Chem.* **2000**, 72, 1156-1162.

## Appendix

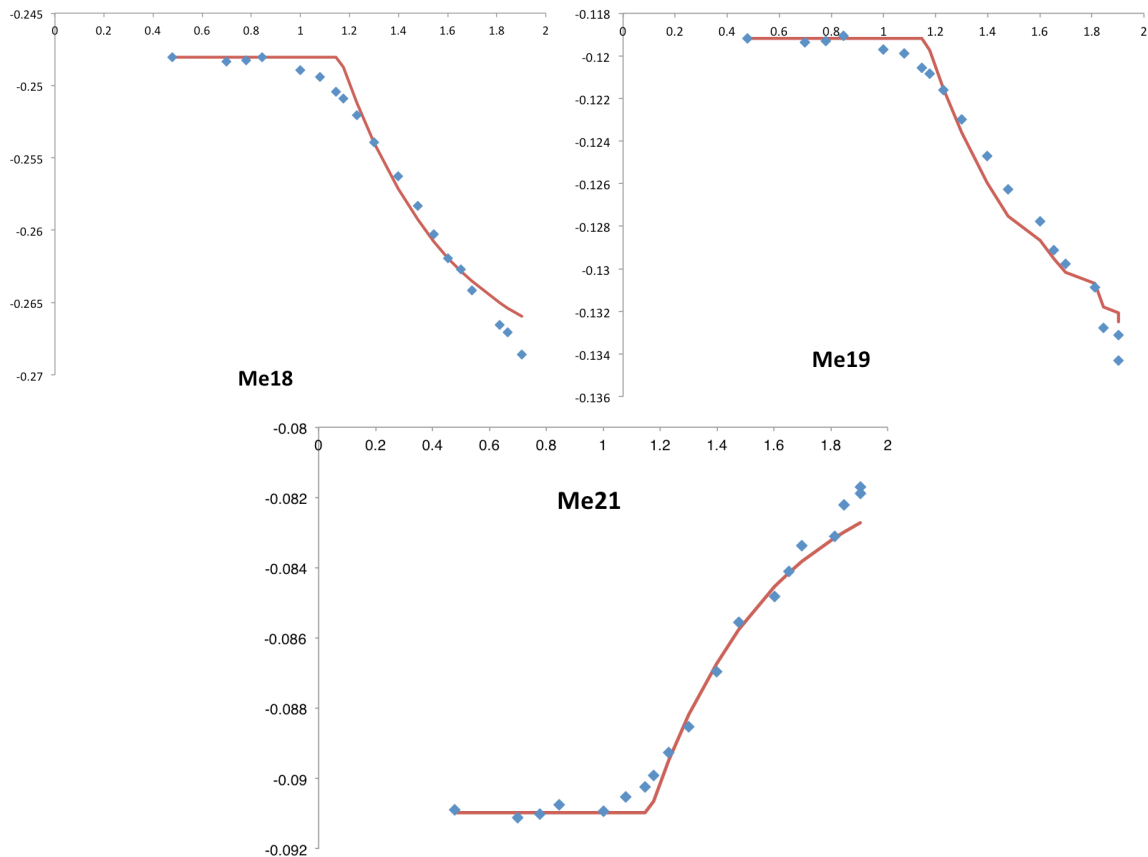


NOESY Spectra of 80 mM taurodeoxycholate at pH 12.0 with 300 ms mixing.

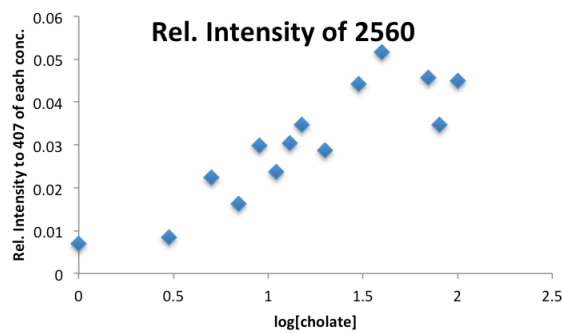
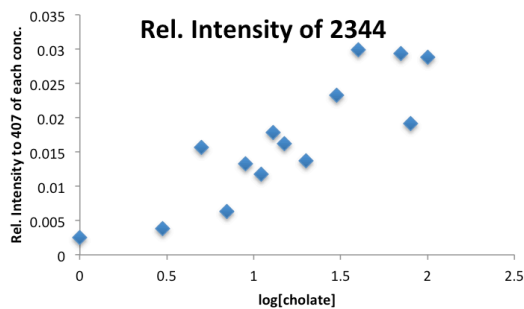
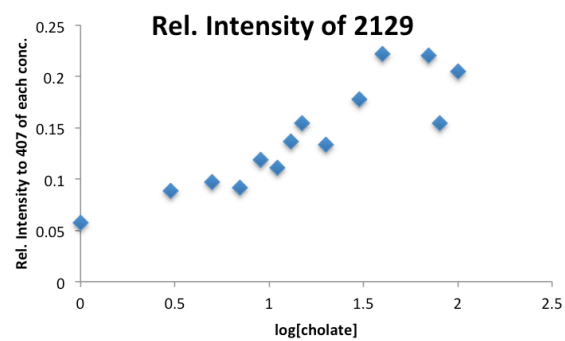
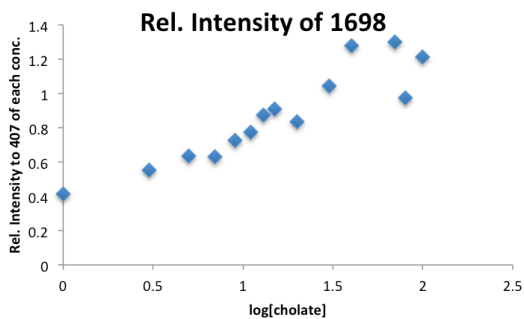
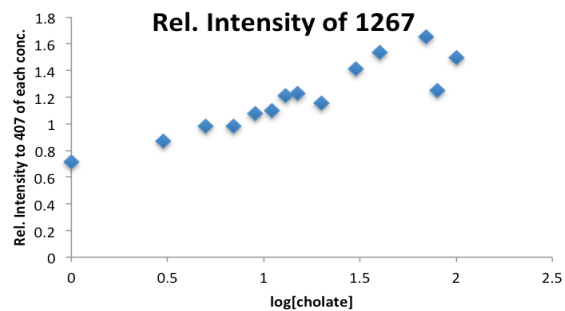
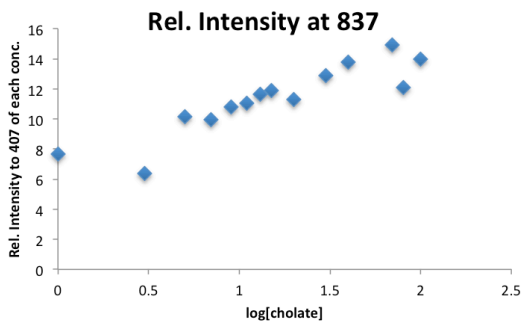
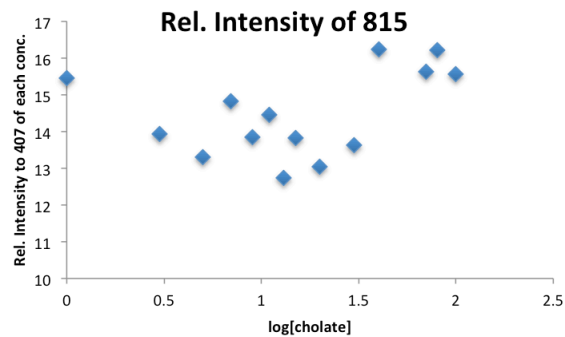
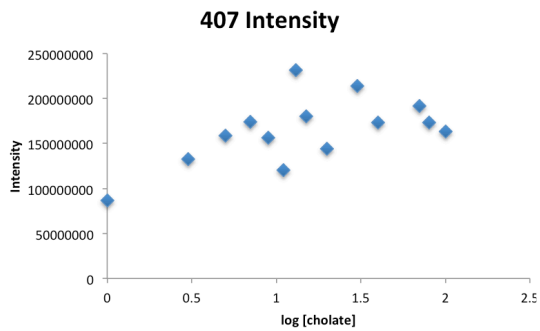
*Left:* Taurodeoxycholate with 2.5 mM R-BNDHP in solution. *Right:*

Taurodeoxycholate with 0.1 mM S-BNDHP in solution. See

HSQC\_noprobe\_NOSEY\_tauro.ppt for more detail.



Phase-transition modeling of the proton chemical shift perturbation of the methyl groups of cholate as their concentration increases at pH 12.0 with 2.5 mM S-BNDHP in solution. *Top left:* Methyl 18 data showing a CMC of 14.5 mM cholate. *Top right:* Methyl 19 data showing a CMC of 14.5 mM cholate. *Bottom center:* Methyl 21 data showing a CMC of 14.5 mM cholate.



The previous page contains graphs of the intensities and relative intensities for every found aggregate in mass spectrometry experiments on solutions of different concentrations of cholate at pH=7.5. All relative intensities are calculated based upon the intensity of the peak at 407 m/z for each concentration.